ELECTRON BEAM LITHOGRAPHY AND INDUCED DEPOSITION FOR NANOPLASMONIC APPLICATIONS

Aline Heyerick

A Thesis Submitted for the Degree of MPhil
at the
University of St Andrews

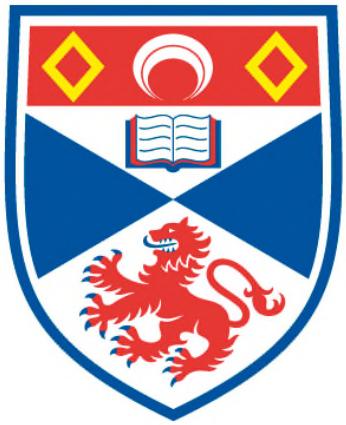

2018

Electron Beam Lithography and Induced Deposition for Nanoplasmonic Applications

Aline Heyerick

University of
St Andrews

This thesis is submitted in partial fulfilment for the degree of MPhil
at the
University of St Andrews

10 September 2017

Abstract

Nanoplasmonics concerns the study of light-metal interactions on a subwavelength scale, exhibiting behaviour able to achieve arbitrary control and manipulation of light at the nanoscale, an important goal for the further development of nanophotonic devices. As the field of plasmonics advances, research is looking beyond the materials and fabrication techniques traditionally employed. This thesis discusses the design, fabrication methods, and characterisation of nanoplasmonic structures. A comparison between two electron beam based fabrication techniques, electron beam lithography (EBL) and electron beam induced deposition (EBID), is presented. The discussion covers both the fabrication technology and the properties of the resulting nanoscale structures: gold nanoscale features obtained via standard EBL, and tungsten structures achieved through EBID. As a mature technology, the well-understood characteristics and reliable fabrication procedures of electron beam lithography are weighed up against the limitations of top-down planar fabrication. Electron beam induced deposition is presented as an alternative technology, able to achieve nanoscale fabrication resolution with a point-and-shoot bottom-up deposition technique, but constrained by the lack of optimised fabrication settings as a result of incomplete understanding of a complex set of patterning parameters. Direct-write EBID technology offers to overcome several of the limitations and challenges of electron beam technology, including three-dimensional and greyscale patterning, and precise alignment and orientation of nanoscale features on arbitrary substrate patterns.

This thesis also presents the discussion of chirped plasmonic diffraction gratings as a specific application in nanoplasmonics. Their theoretical design based on Fourier analysis and simulation-based design, their fabrication using both electron beam lithography and induced deposition, as well as the characterisation of their far-field diffraction pattern are discussed in detail. As part of the characterisation step, a Fourier microscopy setup for the measurement of the far-field diffraction patterns of nanophotonic structures in both reflection and transmission was constructed.

Acknowledgements

During the course of this research I received help from many people. First and foremost I need to thank Dr Andrea Di Falco, my supervisor, who was a guide throughout the project. Special thanks should be given to Blair Kirkpatrick, Peter Reader-Harris, and Monika Pietrzyk, who offered valuable advice and taught me how to use various pieces of fabrication equipment, an essential skill. I am very grateful for the assistance I received from Dr Liam O'Faolain, as my second supervisor, and for the help and advice I received from Professor Manfred Buck and Dr Renald Shaub of the School of Chemistry, who were there to help with the parts of the research requiring a lot of chemical knowledge. I also want to thank the other members of the Synthetic Optics Group: Michiel Samuels, Yufang Shen, Adam Fleming, James Burch, Xin Li, Jingzhi Wu, and Alasdair Fikouras, for being there and sharing the (in)sanity, and the members of the Nanophotonics Group for the friendly and productive experiences working side-by side. In the School of Physics and Astronomy, my research would not have been possible without the work of Callum Smith, Chris Watson, and Steve Balfour, who kept the cleanrooms and lab equipment running and helped to build custom setups, Chris Booth, who assisted with electronics issues, and Scott Johnston, who always kept on top of the many order requests he received from me over the years, no matter how difficult. My sincere thanks go to all of them for making things run smoothly.

I also want to acknowledge and express gratitude for the contribution from Dr. Zhang-Kai Zhou from the School of Physics and Engineering at the Sun Yat-sen University, in Ghuangzhou, China, who provided the nanowire samples which were an essential part of the research into precise alignment using electron-beam induced deposition.

Candidate's declarations:

I, Aline Heyerick, hereby certify that this thesis, which is approximately 36 000 words in length, has been written by me, and that it is the record of work carried out by me, or principally by myself in collaboration with others as acknowledged, and that it has not been submitted in any previous application for a higher degree.

I was admitted as a research student in September 2014 and as a candidate for the degree of MPhil in November 2016; the higher study for which this is a record was carried out in the University of St Andrews between 2014 and 2016.

Date signature of candidate

15 September 2017

Supervisor's declaration:

I hereby certify that the candidate has fulfilled the conditions of the Resolution and Regulations appropriate for the degree of MPhil in the University of St Andrews and that the candidate is qualified to submit this thesis in application for that degree.

Date signature of supervisor

18/09/17

Permission for publication:

In submitting this thesis to the University of St Andrews I understand that I am giving permission for it to be made available for use in accordance with the regulations of the University Library for the time being in force, subject to any copyright vested in the work not being affected thereby. I also understand that the title and the abstract will be published, and that a copy of the work may be made and supplied to any bona fide library or research worker, that my thesis will be electronically accessible for personal or research use unless exempt by award of an embargo as requested below, and that the library has the right to migrate my thesis into new electronic forms as required to ensure continued access to the thesis. I have obtained any third-party copyright permissions that may be required in order to allow such access and migration, or have requested the appropriate embargo below.

The following is an agreed request by candidate and supervisor regarding the publication of this thesis:

PRINTED COPY
No embargo on print copy

ELECTRONIC COPY
No embargo on electronic copy

Date signature of candidate signature of supervisor

18/09/17

Conferences, Schools, Outreach, and Prizes

Conferences and Schools

SUPA Annual General Meeting
Location: University of Strathclyde, The Technology and Innovation Centre
Date: 25 May 2016

SU2P Seventh Annual Symposium
Location: University of Edinburgh, South Hall Complex, Pollock Halls
Date: 4 - 5 April 2016
Poster: Direct Writing Of Nanoplasmonic Structures Using EBID

Advanced Materials Conference
Location: University of St Andrews
Date: 12 - 13 January 2016
Poster: All-Optical Manipulation of Ultra-Thin Conductive Photonic Membranes

SUPA Annual General Meeting
Location: School of Physics and Astronomy University of St Andrews
Date: 25 March 2015

SU2P Sixth Annual Symposium
Location: University of St Andrews
Date: 23 - 24 March 2015
Poster: All-Optical Manipulation of Ultra-Thin Conductive Photonic Membranes

XXVI Distributed Doctoral School on Metamaterials
Location: Abbe Centre of Photonics of the Friedrich-Schiller Universität, Jena
Date: 24 - 28 November 2014
Grant: Grant received to attend the school
Poster: All-optical Manipulation of Ultra-thin Conductive Photonic Membranes

Outreach

International Year of Light Launch Event
Location: Royal Society of Edinburgh
Date: February 23 2015

Outreach Event: Science Discovery Day
Location: School of Physics and Astronomy, University of St Andrews
Date: March 7 2015

Prizes

Name: Arthur Maitland Prize
Location: University of St Andrews
Date: 6 June 2016
Prize for best talk on the PhD Assessment Day

Contents

List of Figures

Chapter 1

Introduction

Light is a powerful, versatile, and widely used tool in science and technology. From being used for carrying information, for optical measurements, and as a source of energy, the list of applications using light across a wide range of sectors is seemingly endless. However, light is currently restricted in its applications by the size of the components used to manipulate it. There is a strong need for the downscaling of optical components and devices, in order to further explore and utilise the advantages offered by light in many applications. To enable light to compete and interact with integrated electronics, there is a need for light manipulation and control at the nanoscale. Current optical components are large and bulky, which is a fundamentally detrimental characteristic for their applicability in scaled-down optical technologies, causing them not only to be unable to compete with integrated electronics in size, but to be limited in the extent to which light itself can be manipulated with nanoscale precision.

This project examines some of the physical concepts able to assist in the achievement of micro- and nanoscale optical applications, and the fabrication methods required to obtain them. The main area of research is nanoplasmonics, the study of the interaction of light and metals at the nanoscale, and a particular chirped grating application is explored as a scaled-down alternative for currently bulky optical technologies. Particular emphasis was placed on the fabrication process, with two separate nanofabrication methods being employed throughout the project, to compare the benefits and disadvantages of both methods.

A first chapter contains a literature review of the current state of the art in the field of nanoplasmonics, comprising an overview of the relevant physical concepts, encompassing the history and development of the field of plasmonics, and outline the state of the art applications and research, providing a particular focus on the use of plasmonics as a building block for metamaterials. The chapter also includes a discussion of the traditional nanoplasmonic fabrication methods and materials and compares them with novel fabrication procedures.

A second chapter covers the fabrication procedures used throughout the process, starting with a detailed discussion of a well-established top-down lithographic etch-back method used to fabricate gold nanoplasmonic structures on flexible polymer membranes. A chirped grating application made using this configuration is discussed, for the creation of a 2D light array which could be mounted on a

fibre for use in endoscopy applications. The overview of the development involves the theory, design, and fabrication steps of the chirped grating as a discrete equivalent of blazed diffraction gratings. A second fabrication method is presented, concerning Electron Beam Induced Deposition (EBID) of tungsten using the Gas Injection System (GIS) of the Raith e-Line Plus nanofabrication [143] tool. The discussion includes a detailed analysis of the setup, alignment and fabrication process using the gas injection system, and the use of the pattern design tool and recipe settings.

Moving on from fabrication to characterisation, a third chapter concerns the development of a Fourier microscope as a far-field measurement setup, to be used in the characterisation of diffraction patterns and detection of optical effects of EBID-generated structures. A fourth chapter discusses the results obtained from the chirped grating and electron-beam induced deposition samples in relation to their fabrication procedures and measurements. The results also contain an outline of future work to be performed as the next step for each topic.

To conclude, the top-down lithographic and electron beam induced deposition fabrication methods are compared, discussing the benefits and drawbacks of working within the limitations of well-known methods and materials using mature technologies, and exploring new opportunities that become available when using newer fabrication methods and materials.

Chapter 2

Literature Review

2.1 Introduction

It is potentially forbidden, or at least severely frowned upon, to compose an introduction to the field of plasmonics without mentioning the Lycurgus Cup, an ancient artefact and illustration of an early, though accidental, application of plasmonics. As it is such an iconic item for the field of research this thesis belongs to, I went to see it in person.

Figure 2.1 – The Lycurgus Cup, displayed in the British museum, is the oldest complete known example of a plasmonic application. Gold and silver nanocolloids cause the cup to appear green in reflection and red in transmission. The image on the left shows a mix of green and red colours on the cup, depending on the specific illumination conditions. The image on the righthand side shows that when the interior of the cup is illuminated the exterior of the cup appears red, from the transmitted light, while the interior of the cup appears green, showing the reflected light.

The Lycurgus Cup is on display in London, at the British Museum, where it can be found in Room 41: early Europe 300 - 1100 AD [1]. It sits by itself in a small glass box in its own column, receiving considerably less attention than the grand display of treasures of the impressive Anglo-Saxon Sutton Hoo Ship Burial archeaological find taking up most of the room [2]. The lighting configuration of

the cup changes periodically, between a single spotlight right above the centre of the cup, illuminating the interior of the cup, and 4 spotlights placed further to the side of the glass box, shining on the cup exterior. As this happens, the appearance of the cup changes from the glass having a red glow, to it looking green. The short explanation card provided by the museum is limited mostly to the discussion of the mythical scenes displayed on the cup, and does not mention the peculiar nature of the colour-changing glass. The reason for the change in colour is that the makers of the late-Roman/early-European glass cage cup (accidentally) embedded gold and silver nanocolloids in the glass, micro-crystals formed of small gold and silver particles. The nanocolloids have a plasmonic resonance peak in the green part of the visible light spectrum, and consequently heavily interact with incident light of that wavelength. As a result, green light is mostly reflected by the glass off the cup, whereas wavelengths far away from the resonance (mostly in the red part of the visible spectrum), are transmitted through the glass. This makes the cup look green when it is illuminated from the outside and the observer sees the reflected light, and red when it is illuminated from the inside and the transmitted light is seen [3].

Although the Lycurgus Cup is an example of plasmonics being used millennia ago, the start of the physical study of plasmonics is often attributed to Gustav Mie's theory of scattering of light be small particles [4] [20]. After the formulation of the theory which broadly explains and predicts nanoplasmonic behaviour, it took several decades for experimental work focussing on plasmonics to take off, which happened in the 1970s and 1980s with the development of Surface-Enhanced Raman Scattering (SERS) [33]. The amount of publications relating to plasmonics has steadily increased since the 1990s [5], covering a range of applications [6] - [16].

The following chapter contains an overview of plasmonics concepts and applications, and electron beam lithography and electron beam induced deposition nanofabrication techniques.

2.2 Plasmonics and Metamaterials: Physical Concepts and Applications

Nanoplasmonics is an area of study concentrating on the interaction of light and metals at the nanoscale. Although the field is mostly confined to classical physics, it does exhibit a range of unusual and unintuitive characteristics and material behaviour. The following sections provide an outline of the physical concepts governing plasmonic behaviour, an overview of the advantages and disadvantages of plasmonic characteristics, and a review of applications.

2.2.1 Plasmonic Physical Concepts

Plasmonics is the study of the interaction of light and metals, a topic discussed extensively in Stefan Maier's 2007 book *Plasmonics: Fundamentals and Applications* [20]. A plasmon polariton, often simply called a plasmon, is a quasiparticle consisting of a photon and vibrating free electrons in the metal. The word plasmon refers to the plasma of vibrating electrons, whereas the word polariton expresses that the (quasi-)particle is not merely a quantisation of the free electron plasma, but that

the plasma oscillations are coupled to electromagnetic radiation.

When light hits a metal surface, the electrons in the metal react to the electromagnetic field, and attempt to neutralise the disruption. If the frequency of the incoming light is sufficiently low, the reaction of the electrons is fast enough to counteract the created effect, and the light will be reflected. If the frequency is too high, the electrons are not able to follow the vibrations and the material will appear transparent to the incoming radiation. The plasma frequency ω_p

$$\omega_p^2 = \frac{N_0 e^2}{\epsilon_0 m_e} \tag{2.1}$$

is completely determined by the material properties and indicates the boundary between reflective and transparent behaviour. Here N_0 is the electron density in the material, e is the electron charge, ϵ_0 is the permittivity in vacuum, and m_e is the electron mass. The transparent behaviour of the metal is often referred to as the dielectric regime, whereas the reflected frequencies are said to experience the material's metal regime. For most metals the plasma frequency is greater than visible frequencies, which is why metal surfaces appear shiny: the photons of the visible part of the spectrum hitting the surface are reflected. Only when the frequency of the incoming light is higher than the plasma frequency, will plasmons be able to propagate through the material, making the material transparent to those photons.

The above paragraphs provide a basic explanation of the interaction between light and metals, but do not explain how plasmons can be formed. There are actually several types of plasmons: of most interest are the ones that exist on a metal-dielectric interface and have the ability to propagate (Propagating Surface Plasmon Polaritons, (P)SPP) or form a type of standing wave on a small metal particle (Localised Surface Plasmon Polaritons, LSPP). Volume, or bulk, plasmons exist as well, but are not discussed in detail here as the majority of applications and research focus on surface plasmonic effects to an extent that when the term plasmonics is used, the intended meaning is often surface plasmonics.

Starting from Maxwell's equations it is possible to calculate the electric and magnetic fields of a wave propagating at the metal-dielectric interface. From these calculations it follows that TE polarised waves cannot be sustained on this interface, while TM waves can, and create a surface plasmon with a propagation constant β, as indicated in equation 2.2.

$$\beta = k_0 \sqrt{\frac{\epsilon_d \epsilon_m}{\epsilon_d + \epsilon_m}} \tag{2.2}$$

Where k_0 is the wave number in vacuum, ϵ_d is the permittivity of the dielectric, and ϵ_m the permittivity of the metal. This propagation constant is different from the propagation constant of the incident light, so momentum will have to be added in order to couple light into the plasmonic mode e.g. through prism coupling techniques or through a grating, as seen in the second term of equation 2.3:

$$\beta = k_d sin(\theta) + m\frac{2\pi}{a} \tag{2.3}$$

where a is the grating period, m the order number, and θ the angle of wave vector k_d with the normal to the surface [20].The angle θ at which the light can be coupled is very sensitive to the value of the plasmon propagation constant β, which in turn can be influenced by changes to the environment (they affect the value of ϵ_d). This makes propagating plasmons ideal candidates to use as refractive index sensors (through permittivity), an application which has been commercialised, and other sensing applications [6] [11]. Plasmons propagating along a metal-dielectric interface penetrate into both materials. Their skin depth is inversely proportional to the absolute value of the permittivity of the material, which means the plasmon usually penetrates deeper into the dielectric than the metal [20].

Instead of propagating along an extended metal-dielectric interface, localised surface plasmons (LSPs) are localised electron plasma excitations caused by scattering phenomena of electromagnetic radiation from a subwavelength metallic particle [10]. The electrons in the metallic particle react to the incident field and at a certain frequency, depending on the material and shape of the particle, achieve a resonating regime able to strongly amplify the electromagnetic field around the particle, concentrating light to subwavelenth dimensions. The strength of the plasma resonance depends on the polarisability (α) of the particle, which for particles a lot smaller than the wavelength of the incident radiation is given by the Frölich condition (equation 2.4), where a is the particle radius. The resonance will be exhibited at frequencies for which particle and medium reach a minimum for $\epsilon_m + 2\epsilon_d$ (ϵ_m = metal permittivity and ϵ_d = dielectric permittivity). This resonance falls in the visible region for gold and silver, two commonly used materials for plasmonic structures [20].

$$\alpha = 4\pi a^3 \frac{\epsilon_m - \epsilon_d}{\epsilon_m + 2\epsilon_d} \tag{2.4}$$

Next to the refractive indices of the metal and dielectric medium, the resonant mode frequency and shape also depends on the particle shape and size. The resonant response can be rigorously determined using Mie theory. Unlike propagating surface plasmons, localised plasmons do not require an exact amount of added momentum and are therefore easier to excite, but their lower sensitivity to environmental conditions makes them less suitable for sensing applications as their response at frequencies close to resonance conditions will still be considerable [20].

2.2.2 Plasmonic Properties: Advantages and Drawbacks

The theory of plasmonic operation is well-studied and understood, and over the years researchers have come up with a wide range of potential applications. Plasmonics have a lot of advantageous characteristics to be exploited, including their narrow confinement ability, enabling focussing beyond the diffraction limit [10] [24] [25] [27], and guiding effects along metal-dielectric interfaces [6] [28]. The narrow confinement also leads to the obtainment of high localised intensity profiles [13] which can be exploited for applications using non-linear effects, which tend to require high intensities [29] [30]. Drawbacks of plasmonics include the high sensitivity to refractive index, leading to strict de-

sign and equipment requirements for plasmonic experimental setups operating at optimal efficiency. Plasmonics also experience high losses which decrease the efficiency of any potential applications and cause local heat production which can cause damage to the sample [25] [26] [31].

The high level of light-matter interaction around plasmonic frequencies leads to considerable amounts of light absorption by the metal, resulting in strong attenuation of the propagating or localised SPPs, their energy being dissipated as heat into the metal [6] [21]. Apart from the loss of efficiency due to optical losses, the heating of the material can be detrimental to the material itself, damaging the plasmonic structures or substrate and even destroy them, and influencing the temperature-dependent plasmonic behaviour [12]. This is especially relevant in localised surface plasmon applications where the field strength is amplified by several orders of magnitude, creating a considerable amount of heat [31].

For feature dimensions smaller than $\frac{\lambda}{2n}$ the magnetic energy of an electromagnetic wave confined to the structure has considerably less magnetic energy than electric energy [25]. This means not all electric energy can be converted into magnetic energy every half period. When free electrons are available this energy gets converted into kinetic energy held by the electrons instead. At the plasmon resonant frequencies the amount of energy held by the electrons restores the electromagnetic energy balance upset by the subwavelength structure. This energy is lost at the scattering rate of electrons in a metal, dissipating a lot of energy as heat within the metal. These losses are an intrinsic property of the size of the structures and the material, and are unavoidable when working at optical frequencies [20] [25].

It has been suggested that losses in plasmonic structures could be compensated by fabricating plasmonic materials with gain, so that the gain cancels out the losses [25], other possibilities include looking for different plasmonic materials [21]. If the losses are compensated by gain, the problem of heat dissipation remains. References [22] and [23] discuss a setup in which Transparent Conducting Oxides (TCOs) are used as a substrate for the plasmonic structures. If a good ohmic contact exists between the metallic plasmonic structures and the conductive membranes, the free electrons carrying the excess energy can move into the membrane and spread out on a sub-picosecond timescale [23], which will allow the heat to diffuse across a larger area, and into the membrane instead of the plasmonic structures. The option of dealing with losses by using alternative plasmonic materials is discussed in more detail in a separate section below.

2.2.3 Plasmonic Applications

Plasmonic have been used in commercial applications for millennia, using their interesting and aesthetic colour effects to obtain coloured glass including Roman pottery and European mediaeval stained glass windows [1] [4]. Although these are undeniably early commercial successes which have stood the test of time, they were produced without a true understanding of the plasmonic processes taking place. However, plasmonic sensors based on modern understanding of plasmonic effects are also commercially available, and are being used in cancer treatment methods and in electronics components [32], indicating that despite their drawbacks, plasmonics can move beyond the research-stage and become commercially viable applications.

Research is being performed in a range of areas including several where commercial success has already been achieved, as mentioned by Stefan Maier in the August 2015 Nature Photonics Editorial [32]. The sensitivity of plasmonics to refractive index changes, which is often a drawback as it sets very narrow tolerance values on setup requirements, is also a characteristic which can be exploited to make high-performance sensors [12]. Another area where plasmonics can be used for sensing purposes is Surface-Enhanced Raman Spectroscopy (SERS), which uses plasmonic features to increase the local intensity of the interaction with light to increase the amount of Raman scattering taking place [33] [34]. SERS can be used in a variety of applications, including in the field of biophotonics, which is also a popular area for other plasmonic applications [11]. More than just sensing and detecting light, plasmonics can be used in applications seeking to collected light, which can be useful for a range of applications to increase the interaction of a device with light, e.g. in solar cell applications [35].

The interaction of plasmonics with light can go beyond detection and collection, to engineer arbitrary control or manipulation of light. This arbitrary control can be achieved by using plasmonic structures as the basic building block for metamaterials, a periodic array of nanoscale structures which forms a material with specifically engineered bulk properties [16] [38]. In order to grasp the concept of metamaterials, it helps to understand that when light interacts with materials, the behaviour can be described using the bulk properties of the material (permittivity, permeability, etc.), and does not require taking the individual atoms and crystal structure into account. This is the case because the wavelength of visible light (around 400 - 700 nm) is several orders of magnitude larger than the size of the individual building blocks of the material (around 0.1 nm or 1 Å). Using nanoscale fabrication techniques (see chapter 3) it is possible to construct periodic arrays of nanoscale written patterns which form an array of meta-atoms to create a metamaterial. The interaction of light with this metamaterial can be described by the same bulk variables including permittivity and permeability. By specifically engineering the characteristics of the meta-atoms and their distribution to form the metamaterial, bulk properties can be achieved which do not appear in nature [39] [40]. In order to obtain effective interaction of the light with the meta-atoms they can be constructed from plasmonic materials, and the fields of metamaterials and plasmonics have evolved together [5] [41]. Metamaterials can be achieved in 3D structures, although they can be challenging to fabricate due to restrictions in nanoscale fabrication techniques (see section 3.1). As an alternative the fabrication of metasurfaces, a 2D metamaterial consisting of a single layer (or a small amount of layers) of small, planar plasmonic structures, is more straightforward to fabricate and has been widely researched [42] [43].

Applications aimed at controlling and manipulating incident light include a wide range of applications, some of which are optical cloaking [44], epsilon-near-zero and negative refractive index materials [9] [16], filters [47], nanoantennas [27] [46], flat optics [45] [48], periodic gratings, and other diffraction pattern generators [50]. Among the diffraction pattern generating components are plasmonic chirped gratings, which are of particular interest to obtain broadband interactions in applications for sensing, collecting, guiding, and manipulating light [51] [52] [53] [54]. There are even metamaterials designed to be reconfigurable, by thermally, optically, or electromagnetically switching between different states of the material to invoke different light-matter interactions [55].

2.2.4 Enhancing the Application Possibilities of Plasmonics

Flexible plasmonics

As can be seen in the overview of applications provided in the paragraphs above, the potential reach of plasmonics applications is very wide. Plasmonics are, however, limited not only by their inherent disadvantageous drawbacks, but also by the limitations of fabrication equipment. As nanoscale fabrication is needed, traditionally a lot of experiments were and still are performed on samples made using top-down Electron Beam Lithography (EBL, see 3.1), which is limited to rigid and planar sample fabrication. Many of the potential applications have requirements for which plasmonic structures on rigid planar substrates are not suitable, for example sensing applications where the apparatus has to adapt to the environment of the subject. One potential solution to overcome this limitation of EBL is to develop alternative fabrication methods able to fabricate plasmonic features in these varying locations and environments [56]. Another option is to place plasmonic features on (transparent) flexible substrates, as is being done for flexible electronics [57]. This enable the plasmonic structures to be placed in a variety of environments and conform to a wide range of shapes [58] [59]. The substrate can be engineered to limit its influence on the interaction with the light and plasmonic features, or it can be designed to play an active role in the interaction with the light (e.g. ohmic dispersion for spreading of heat dissipation [22] [23]). The substrate can further be used to tune the properties of the plasmonic features through rolling, stretching, bending, folding etc. [60] [61].

Plasmonic materials

When designing plasmonic applications, losses are always an important element to take into account. In the visible range, gold and silver have traditionally been the most popular material choices, as their losses in those wavelength ranges tend to be lower than those of other materials. However, gold and silver still exhibit significant plasmonic losses, their response is not tunable [62], they are not suitable materials for integrated electronics or photonics applications, and are expensive [32] [66]. As a result, the search for alternative materials has continued, and as research into plasmonic applications advances, other materials are being considered to suit specific applications [5] [21] [41]. One proposed idea to overcome the optical losses is to work with dielectric metamaterials. The coupling of light with the subwavelength structures does not suffer from high losses through heat dissipation, but the strong light-matter interactions achieved by plasmonic features are not present, which leads to lower efficiency [63]. The performance of gold as a plasmonic material drops for shorter wavelengths in the visible spectrum, and for these blue-range colours, aluminium has shown to be a suitable alternative metal, and has been used in applications for that purpose [36]. Although not as frequently used as gold and silver, aluminium and copper are also considered to be metals with plasmonic performance [66]. Having accepted that there is no way to eliminate losses from even the best performing traditional plasmonic metals, and realising that there is no perfect solution or wonder-material overcoming all difficulties and showing exceptional plasmonic behaviour without drawbacks, research efforts have been directed towards finding and developing specific materials and tune their characteristics to satisfy the needs of specific applications. In theory it is possible to engineer materials to be optically lossless in a specific wavelength range, but this has not yet been experimentally achieved [66]. Gold and silver, and to an extent aluminium and copper, have acceptable intrinsic properties but the possibilities to alter these properties is limited, making them unsuitable candidates for this individually tailored plasmonic material approach.

A lot of research around alternative plasmonic materials has been performed by the research group

of professor Vladimir Shalaev. In a paper by *N. Kinsey*, *M. Ferrera*, *V. Shalaev*, and *A. Boltasseva* from 2014 [66], an overview of potential plasmonic materials is provided singling out two groups with particularly promising characteristics. A first group are the II-VI semiconductor materials, also known as Transparent Conducting Oxides (TCOs) (e.g. SnO, InO). They obtain their plasmonic properties by being able to tolerate high doping levels, which renders their behaviour metallic. Because the plasmonic properties depend on the nature and level of doping, TCO properties are also strongly tunable [66]. Another material exhibiting promising tunable properties as a result from its ability to be doped is graphene, which is considered for plasmonic applications in the mid- and far-infrared wavelength ranges, both by itself and in combination with other materials (e.g. boron nitride). A shallow penetration depth, potential effective heat dissipation and loss reduction are other desirable qualities for plasmonic graphene potential applications [5]. The second group of interesting materials mentioned by *Kinsey* are the Transition Metal Nitrides (e.g. WN, TiN, CuN), as they are chemically stable ceramic materials that can withstand high temperatures, which enables them to deal with large amounts of heat produced by plasmonic activity. Transition metal nitride properties can be tuned by changing deposition conditions [66] [64] [65]. Although tungsten nitride is signalled as a promising material, tungsten itself is suggested to have poor plasmonic performance abilities based on its real and imaginary permittivity values [64], while tungsten oxide nanorods have been reported to exhibit tunable localised SPP resonances in the near-infrared [67]. The search for materials with better plasmonic performance is far from over, and has expanded in many directions as the requirements for individual applications and the potential of tunable materials become more apparent.

2.3 Plasmonics and Metamaterials: Fabrication Techniques

In order to experimentally study nanoplasmonic effects, there is a requirement to fabricate nanoplasmonic samples, which in turn presents a necessity to have access to nanoscale fabrication techniques. The following sections will provide an overview of the development and functioning of the two electron beam based fabrication techniques which played an essential role in the project. First, the top-down fabrication technique Electron Beam Lithography (EBL) will be discussed. The first part of the discussion will focus on the history and development of the technique to emphasise the maturity of the technology, and the advantages associated with using equipment which exists as a results of decades of intensive research and development efforts. The placement of the technology in a historical context is followed by an explanation of the basic operational principles of an electron beam lithography system, and the presentation of an overview of the state of the art of EBL perfomance. The second part of the discussion covers a bottom-up fabrication technique making use of a focussed electron beam: Electron Beam Induced Deposition, which has the ability to deposit material in the proximity of a sample surface onto that surface through electron beam irradiation. The existence of this phenomenon has been known for approximately the same amount of time [81], but has not benefitted from the same amount of investement or research into the technique. As a result, the relatively new availability of commercial systems employing this as a nanoscale fabrication technique means the technology is a lot less well understood. Research surrounding electron beam induced deposition focusses a lot more on the actual fabrication techniques and resulting sample quality, as opposed to electron beam lithography, where the fabrication methods are better understood and often taken for granted. The section contains a discussion of the fabrication technique and some EBID-based applications. The next section gives a short overview of some other existing nanofabrication techniques, to idicate that there other alternatives to EBL are available.

2.3.1 Electron Beam Lithography

Electron Beam Lithography (EBL) is a mature technology, which has been widely used in research and industry for several decades [78]. In order to understand the importance, benefits, and motivations of using a technique as well-developed as EBL, it is essential to know the historical context which has led to decades of considerable effort being put into developing the technology, and the technological importance of a race to push the state of the art forward to achieve smaller and more precise fabrication possibilities.

Electronic technology played a key role in shaping the twentieth century. The speed at which the expansion and development of electronic technology has progressed and the way electronics has embedded itself into almost all aspects of modern life throughout the century are hard to miss, and the advancement of the technology was enabled by significant progressive efforts and several key technological developments taking place in the middle of the twentieth century, when several novel inventions combined to create the field of integrated circuits.

The first event that helped lead to the development of electron beam lithography is often considered to be one of the most important inventions of the twentieth century [69]: the invention of the transistor by William Shockley in 1947. Shockley's transistor allowed fragile and bulky vacuum tubes to be replaced with a smaller, more efficient equivalent made from semiconductor materials compatible with other electronic components. Shockley received the Nobel Prize alongside his Bell Labs colleagues John Bardeen and Walter Brattain in 1956, just 8 years after their initial discovery of the transistor and the presentation of their understanding of charge behaviour in semiconductor materials, indicating that the significance of this development [69].

Although the transistor was a significant improvement over the vacuum tube in many ways, electronics as a field still struggled with the *tyranny of numbers* problem, a phrase first introduced by Vice President of Bell Labs Jack A. Morton in 1958 [70]. The power and complexity of computing systems were limited by the amount and size of the available electronic elements. In order to add to the computing power, the amount of transistors needed to increase drastically, but transistors and other electronic components at the time were still discrete and separate pieces, which needed to be placed and soldered onto an electronic circuit manually, limiting the amount the components could be scaled down and the system scaled up [72]. The invention of the transistor paved the way and provided motivation for the development of integrated circuits (ICs) which would present the solution to the scaling problem and overcome the tyranny of numbers [71]. The idea of integrating electronic components on semiconductor materials was supported and spread by Geoffrey Drummer, who presented an idea in 1952 that: "With the advent of the transistor and the work in semiconductors generally, it seems now possible to envisage electronics equipment in a solid block with no connecting wires. The block may consist of layers of insulating, conducting, rectifying, and amplifying materials, the electrical functions being connected directly by cutting out areas of the various layers." [72]

It is not possible to pin the invention of the integrated circuit to a single person, as the technology developed gradually. Drummer's disclosure of the idea of integrated circuits was followed by research

that lead to discoveries of integrated circuits by Jack Kilby [72] and Robert Noyce [73]. Once the theory and concepts of integrated circuits were developed, the limiting factor to access the incredible potential offered by ICs and transistors was the fabrication resolution, which resulted in the research effort being directed there, motivating the development and improvement of electron beam lithography. Another key event accelerating the development of lithography systems took place in 1965, when Gordon Moore predicted a trend, based on a limited set of data points, that the amount of transistors per area would double every year [74]. This statement has become widely known as *Moore's law*, and the semiconductor fabrication industry has kept up with the prediction for decades, although the process has slowed down. Considering the short period and small amount of data points, Moore's law is arguably more likely to be Moore's self-fulfilling prophecy. Moore set a roadmap for the industry, and the industry has risen up to face the challenge and has committed considerable efforts to stay in the race. In 1975 fabrication technology enabled a minimum feature size of an integrated circuit transistor of around 8 μm; by 1982 that minimum size had decreased to around 2 μm [71]. The smallest transistor size set to become commercially available in 2017 is 10 nm [75]. The scaling down of electronic components has slowed down over the years, as the challenges faced to create the fabrication technology and methods necessary to fabricate the features become harder. Moore's law has already come to an end as transitor size decreases can no longer keep up with the speed dictated by Moore's predicition, and the continuing decrease of transistor size will eventually run into physical limits.

The momentous pressure and efforts invested in scaling down transistors in an integrated circuit required the continuous development and improvement of fabrication techniques, including the technique which is the topic of this discussion: electron beam lithography. Electron beam lithography was initially developed during the 1960s, after the discovery that electron beam irradiation could cause membranes to form by breaking and forming bonds in and between molecules [76]. Alongside this discovery, work was being performed to better understand and control the properties of electron beams (e.g. the determination of charge distribution inside high-current electron beams, by Ashkin in 1957 [77]). The combination of this work resulted in the first electron beam lithography systems being developed by converting Scanning Electron Microscope systems to be able to write patterns instead of being used to detect and form images [78]. After the discovery of PMMA (poly-(methylmethacrylate)) as a suitable resist in 1969 [79], a resist still widely used today for patterning using electron beam irradiation, there was an enormous drive to improve electron beam lithography and other technologies related to the fabrication of integrated circuits. This drive for improvement has lasted for decades, propelled forward by Moore's law and commercial applications for the electronics industry worth over 300 billion dollars each year [80], sparing neither money nor effort in the race for the advancement of the electronics, microelectronics, and nanoelectronics fabrication technology.

Electron Beam Lithography System

The electron beam

There are several types of electron beam lithography systems, ranging from state-of-the-art setups for industrial commercial applications, to more basic configurations for research setups. The first types of lithography systems were converted/modified Scanning Electron Microscope setups, and this type of lithography setup is still frequently used today. Purpose-designed-and-built lithography systems are also available. These tend to have a higher electron beam energy to achieve better resolution and beam stability. Systems using a modified SEM setup function at lower electron beam energies and

are a lot cheaper, while still being able to achieve beam diameter sizes under 10 nm [90].

The nature of the electron beam is determined by its source and electron optics, and has a significant impact on the resolution of the system and the quality of the irradiation pattern. Electron sources are either thermionic, where energy is applied by adding heat to the system, or they are obtained by applying a strong electric field, also referred to as field-emission sources. These field-emission sources can be cold, relying solely on the electric field, or they can be heated, which tends to decrease resolution but increase beam stability. In both cases the electrons are often emitted from a narrow conducting point to increase the effects of the heat or electric field application, and facilitate the emission of electrons. The electron source has size, brightness, and energy spread parameters which determine the quality of the beam, and are equivalent parameters to the size, intensity and wavelength range of optical sources. A low energy spread is desirable, as the behaviour of the electrons hitting the surface is ideally as uniform as possible. Any changes in electron interaction with the material should be engineered by the system settings rather than left uncontrolled and unavoidable due to a large range of electrons all being produced by a single source [78] [91].

Most lithography systems use a Gaussian electron beam, but some systems have additional beam-shaping electron optics built in to be able to engineer the shape of the beam more precisely [122]. These beam-shaping optics tend to make the system significantly more expensive and are only found in systems at the higher end of the market. Although beam-shaping optics are rare and expensive, even basic modified SEM systems require some electron optics to control and manipulate the beam after it exits the source. The movement of electrons can be influenced by electrostatic or magnetic forces, and these are used to create what is referred to as electron lenses, although the electronic and/or magnetic configurations are not alike to traditional optical elements [78] [91].

Next to electron lenses a lithography system also has one or more apertures in place. These can be used to correct for aberrations induced by the electron lenses and clean up the electron beam, they can be used for blocking or blanking the beam when it is not writing, and the aperture can also set the range of angles of incidence from which electrons can reach the sample surface [78]. A lithography system is likely to be configured to be able to switch between a selection of apertures to change the write settings, and therefore aperture alignment is often a necessary step in the initialisation of an electron beam lithographic write. Alongside apertures which can be used to improve the quality of the electron beam, an EBL system also has electron optics present to influence the nature and shape of the beam by correcting for astigmatism, which is an aberration causing the focal lengths to differ in the x- and y-direction of a beam travelling along the z-direction. Astigmation alignment helps achieve a round, focussed beam. The electron beam lithography system discussed and used throughout this thesis comprises a heated field-emitter source providing a Gaussian Beam.

The irradiation process

Electron beam lithography creates patterns by irradiating a specifically chosen radiation-sensitive material which reacts with the electrons and undergoes a structural change. These materials are referred to as resists and can be used to form masks or as the target material for patterning itself [78]. They can be organic or inorganic, consist of a single type of molecule or a mixture of multiple molecules, and are characterised by their sensitivity and patterning contrast [92]. Depending on the specific resist material used, irradiated areas of the material are changed in such a way where they

can be removed during development of the resist after irradiation, leaving behind the non-irradiated areas (positive resists), or the opposite can be the case, where the irradiated parts remain and the unexposed areas are removed during the development step (negative resists) [71].

Electrons in the electron beam hit the resist surface at acceleration voltages around 1 - 30 kV for modified SEM systems, and between 20 - 100 kV for purpose-built systems [90]. For these high energy electrons the resists tend to be mostly transparent, and the electrons penetrate into the resist material and potentially layers of the materials underneath. These high-energy electrons are sometimes referred to as primary electrons. They can undergo elastic scattering and change direction within the material without losing energy. This change in direction causes a significant widening of the electron beam within the resist, which is why the minimum resolution and feature size within a resist is usually higher than the achieved beam diameter during the electron beam exposure. This beam widening can be reduced by using a high acceleration voltage for the electrons, which is one of the reasons why purpose-built lithography systems have better patterning resolution. If the direction change of the electron is greater than 90 ° compared to the original direction of incidence, the electron has backscattered. This backscattering can occur both in the resist layer, or in lower layers, meaning an electron can traverse the resist more than once, which increases the actual irradiation dose compared to the theoretically intended one and causes even further widening of the electron beam This is sometimes called the proximity effect and can be partially corrected by changing the patterning design [78] [90] [122].

When an electron non-elastically scatters, it loses some of its energy as well as obtaining a change in direction, and a secondary lower-energy electron can be created. As the primary electrons lose energy and create secondary electrons, some electrons can exist within the resist with the right amount of energy to interact with the resist, breaking and creating bonds between neighbouring molecules. Crosslinking of neighbouring molecules to form a less easily dissolvable material structure is the main irradiating action in negative photoresists, and the electrons break up polymers into smaller, dissolvable pieces in positive photoresists [78] [90].

The patterning method

The electron beam is directed across the resist to write a pattern. Electron optics are used to deflect and move the beam across a single write field, the size of which can often be set within the machine. The size of the write field is the size of the area patterned by the electron beam without moving the sample stage. The electron beam is moved across the write field by deflecting the electron beam. For patterns extending beyond the boundaries of a single write field, the stage holding the sample is moved instead of deflecting the column. The patterning parameters are stored in the GDSII format, a frequently used file format for resist patterning [145]. It is a format designed to be able to store a lot of information about the nature of the pattern to be exposed, and the specific parameter settings it should be written at, or to function with only a basic amount of writing parameters provided, being flexible to the need of the specific user and patterning system [145]. Pattern parameters are specific to the materials and samples used and are discussed in more detail in chapter 3.

EBL resolution limits and applications

The resolution limits of EBL have consistently been decreased and can now be pushed below 10 nm [92] [94] [96]. Although there are other technologies that can achieve higher resolution, delivering

smaller feature sizes (e.g. AFM), EBL has always been viewed as a top-performing practical fabrication technique [92] [93]. The actual limit depends on the specific EBL system (modified, purpose-built, ...) and resist being used, and the design of the pattern itself. To push the resolution limits further, next to improving the system and system settings, over the years researchers have looked into developing new resists (e.g. HSQ, hydrogen silsesquioxane) and improving development procedures [92] [95]. For a PMMA resist it has been shown that developing the resist in isopropyl alcohol in an ultrasonic bath (see chapter 3 for more information) can improve the resolution limit by removing excess material [94]. Despite its disadvantages, which include cost and planar sample requirements, EBL is the preferred nanofabrication method for a lot of applications and research groups, including research into improving transistor designs, nanophotonic structures and bio- and pharmaceutical applications [92]. The established status of EBL as a reliable and understood technology means that any other nanofabrication technique will need to offer significant advantages to be considered as a valid alternative.

2.3.2 Electron Beam Induced Deposition

The possibility of performing Electron Beam Induced Deposition (EBID) was proposed in the late 1950s as a means to measure astigmatism, and discovered in the early 1960s when it was noticed that thin films could be deposited on sample surfaces as a result of electron bombardment in the presence of vapour [98] [81]. Although it has been around as long as EBL, EBID did not receive the same amount of research and development effort and investment, being first seen as contamination writing, an unwanted side effect. As a result EBID is still in its research stage many decades later. The technique has progressed, as it has benefitted from several of the developments made in EBL technology, as EBID can employ a lot of the same electron beam equipment. Just like with regular EBL, the resolution of the system is increased for higher electron energy and acceleration voltage, and a small working distance. However, as the system requires room for tools to locally supply the precursor gas, the working distance cannot be made arbitrarily small [90]. The sample chamber of an electron beam lithography system can be adapted to include the necessary gas injection equipment to enable EBID fabrication processes to take place, and machines have been built that combine traditional EBL techniques alongside EBID and other nanofabrication tools [143]. Although it has not been as intensive, research into the fabrication, resulting materials, and potential applications has slowly built up over the years [89] [98].

Electron Beam Induced Deposition (EBID), sometimes referred to as FEBID (Focussed Electron Beam Induced Deposition) has many benefits as a technology for nanoscale fabrication over regular Electron Beam Lithography. Where a metallic pattern made via EBL requires a plurality of steps including the deposition of a metal layer, covering the metal with a resist layer, patterning the resist, developing the resist, and the etching away the exposed metal, EBID is able to direct write the metallic patterns straight onto a sample surface using a focussed electron beam and a locally supplied precursor gas [90] [82]. Having the ability to write structures in a point-and-shoot configuration is a great advantage that enables EBID to easily execute certain patterning tasks which would be very challenging with traditional EBL. A first example is making metal contacts to previously formed structures on a sample. Sometimes these structures are patterned in a previous lithography step, in which case their location could be determined by using alignment markers and having an accurate map of the previous written pattern. This comes with challenges as the metal and resist layers make

it hard to locate and use alignment markers covered underneath several other layers, and even if it is successful the alignment procedure is an extra step making the already long fabrication process even longer. Although the above alignment procedure for metal contacts could be challenging, the process of how to achieve it is in theory clear. This is not the case when the metal contacts need to be made on structures which are not specifically placed on the surface (e.g. nanorods grown on a sample surface). There are no alignment markers, and no detailed map of the location of the features. Although it might be possible to place alignment markers on the sample and to create a detailed feature map, the solution is not obvious or straightforward, and would be challenging and time consuming. In contrast, for EBID, the procedure would be as simple as navigating to the place where the contacts need to be placed, easily found as they are exposed, and starting the patterning process. The research can then focus on the challenges of improving the metal contact properties itself [84] [83].

Another advantage of EBID is the ability to write greyscale or 3D structures in combination with the precise alignment possibilities of EBID. In theory, nanoscale features of an arbitrary three-dimensional shape can be written on an arbitrary substrate. The features can be simple shapes, e.g. SNOM-tip (Scanning Near-field Optical Microscopy) enhancement [106], nanopillars [105], or nanowires [99]. Alternatively, EBID is also able to fabricate complex shapes with holes, gaps, bridges, and varying width and height profiles [143] [104].

EBID fabrication process

EBID uses the energy provided by the incident electrons originating from the electron beam to induce the molecular dissociation of the present gas molecules. The highly focussed electron beam allows the deposition to occur in a very localised manner, enabling it to write sub 10-nm structures, including dots with a diameter smaller than 1 nm and lines with a width smaller than 2 nm [88]. In order to avoid deposition of material outside the irradiated areas the gas is delivered close to the sample surface in a very localised manner, and the precursor gas molecules released into the chamber are engineered to be quite volatile, but still contain active groups able to adhere to the surface. When reacting with the accelerated electrons coming from the beam, the molecules making up the precursor gas are designed to dissociate into a desired deposition material, the part of the molecule adsorbed to the sample surface, and a byproduct engineered to be volatile, to facilitate their easy removal from the vicinity of the sample surface (see figure 2.2). The dissociation of molecules into the target and byproduct molecules is achieved both by primary and secondary electrons [101] The precursor molecules are sufficiently volatile to not remain attached to the surface if the above dissociation into target and byproduct molecules does not occur [89].

The precursor gas used for electron beam induced deposition influences the quality of the material deposit. To obtain a high purity deposited material it is essential for the process to take place under high vacuum conditions to avoid the deposition of impurities caused by molecules other than the injected gas molecules present in the chamber. The reaction resulting from the interaction between the electron beam and the precursor gas should be predictable, consistent, efficient, and create the desired deposit material which should easily adsorb onto the surface. The two metals on which this project focusses are gold for EBL and tungsten for EBID, both of which can be deposited using EBID. In their 2009 paper *"Creating pure nanostructures from electron-beam-induced deposition using purification techniques: a technology perspective" Botman* et al. provide an overview of the different types of material and their achieved deposition purity [89]. Their review reports on a 66% purity of tungsten

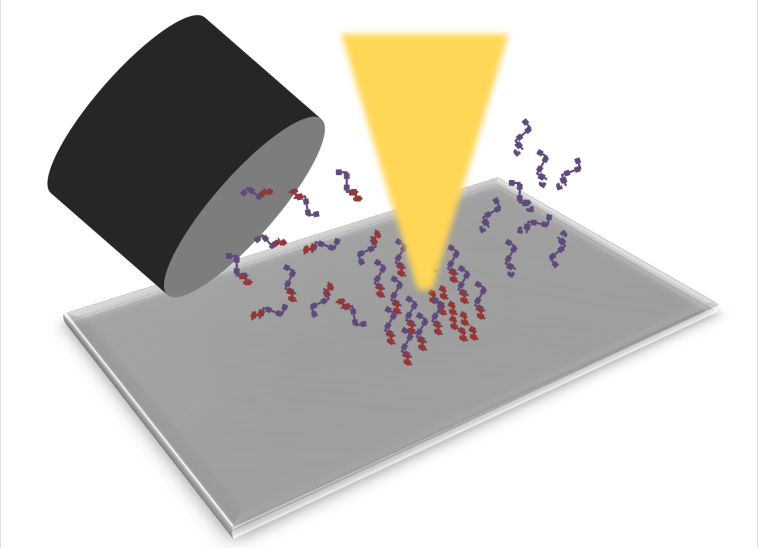

Figure 2.2 – During electron beam induced deposition locally supplied precursor gas (red and purple in image) molecules loosely adhere to the sample surface, and are dissociate by incident electrons into a target molecule and a volatile byproduct. The volatile byproduct is removed by the vacuum pump of the system, and the small target molecules are strongly adsorbed onto the sample surface and forms the desired deposit layer.

and 100% purity of gold obtained using electron beam induced deposition techniques. The quality of the deposited material is a critical shortcoming of electron beam induced deposition compared to other, more established metal deposition techniques like chemical vapour deposition, molecular beam epitaxy, or electron beam evaporation, which are often employed in combination with standard EBL fabrication procedures. As a result, researchers are working to develop methods for achieving higher quality EBID-deposited materials [89].

In order to improve the quality of the deposited material it is important to understand how the different parameters of the EBID write settings influence the deposition. It is equally important to understand the properties of the deposited material itself, so that its quality can be improved and further purified once it has been deposited. Looking at tungsten as a specific example, EBID patterning parameter settings influence the quality of the resulting deposited tungsten material. A first property of the deposition process that can help with understanding how to improve the writing parameters and deposition conditions relates to the dissociation rate of the precursor gas molecules, which is proportional to the density of the precursor molecules and EBID electrons at the target substrate surface [90]. The metal content, or purity, of the deposited material increases with increasing beam current, as the higher electron concentration at the target deposition surface leads to more precursor molecules to be dissociated into a target deposit and volatile byproduct. The size of the deposited nanocrystals formed from the target deposit particles increases with the precursor molecule flux and resulting concentration [89]. For tungsten obtained from $W(CO)_6$ precursor gas it was also shown that the conductivity, which can be seen as an indicator for the deposited tungsten material quality, is increased for slower scan speeds, with longer dwell times and loop times [86] [102]. The above improvements can be explained by the deposition shifting from an electron-limited to a precursor-limited regime. In the precursor-limited regime, a larger fraction of the molecules dissociate, and the dissociation into smaller fragments is more complete. As a result, the adsorbed molecules will be more fully dissociated and have a higher metal content, and less residual precursor molecule groups

will remain adhered to the surface. Although the above findings are described for tungsten, they are more generally valid and are true for several other EBID deposit materials [89].

Looking at post-EBID purification techniques of the resulting material, a first well-known method is annealing: heating up the material can increase the amount of crystallisation of the deposited material present, and remove impurities from the deposit. However, tungsten in particular is at risk of oxidation, which would decrease the overall metal purity, so the annealing process should take place in high-vacuum conditions, with as little oxygen present as possible to avoid tungsten oxidation.

The impurities in the tungsten material deposited through EBID consist of remnants of undissociated precursor molecules, molecules for which dissociation was incomplete, byproducts which were trapped on the substrate instead of removed, and residual impurities not removed by the vacuum pump of the system. The residual impurities tend to mostly comprise water vapour, nitrogen, oxygen, and small hydrocarbon groups, and can be hard to remove once the material is deposited. It would therefore be beneficial to find a method to avoid the impurities and unwanted precursor side products being deposited in the first place. One potential solution is the technique of reactive gas mixing, the idea of which is to have the impurities interact with a gas added to the chamber, instead of the target deposit. In the case of gold, which is not oxidisable, adding oxygen improved the deposit material purity, but with easily oxidisable tungsten, the resulting purity was worse than without reactive gases present, as the amount of carbon impurities was not significantly reduced, and the amount of oxygen contamination increased [103]. It should be noted that in section 2.2.4 tungsten oxide is mentioned as a material which exhibits plasmonic properties, and the oxidation effects mentioned above should therefore be kept in mind when looking for a method to produce tungsten oxide through $W(CO)_6$ EBID fabrication, as finding good quality precursor gases is not a straightforward task, as those precursors need to be compatible with the EBID system as well as being capable of depositing a target material with plasmonic properties. In light of the vast array of parameter settings and molecule selections and variations that can be performed, simulation methods have been developed in order to facilitate a method of predicting outcomes and researching having only the guidance of experimental results [82]. Simulations can also be used to guide determine specific recipe and patterning settings to achieve desired EBID designs [104].

EBID applications

Van Dorp stated in his 2008 Journal of Applied Physics paper that there are a plethora of results out there [100], and the technology and research community around it have not yet reached a stage where a common set of results are accepted as tried and tested, illustrating that the technology and field are still in their developing phase. However, the significant benefits and unique fabrication possibilities offered by electron beam induced deposition mean that applications have been achieved under research conditions for decades. The range of applications explored over the decades is large and includes the creation of field emitter arrays by *Morimoto* et al. [107] and several conductive nanostructure designs by *Koops* et al. [108], both in 1996, by depositing platinum or gold on a silicon array using EBID. *Graells* et al. presented the fabrication of gold plasmonic nanostructures using EBID in 2007 [109]. In 2015, *Sengupta* et al. published a paper on the fabrication of superconducting tungsten nanowires using EBID [110]. Keeping the focus on tungsten, Electron beam induced deposited tungsten obtained from a tungsten hexacarbonyl precursor ($W(CO)_6$) has been used as a material to provide interconnects and metal contacts [85] for a variety of structures. As conductivity

is an important parameter for electrical contacts, there have been several studies on the conductivity of EBID-tungsten, as mentioned above as part of the discussion around optimising writing parameters [86] [87] [102] . The possibilities of a maskless nanopatterning technique able to deposit a wide range of materials with accurate and precise location alignment and the ability to write three-dimensional patterns has opened the door to a wide range of potential applications hich would not be accessible using standard EBL fabrication techniques.

2.3.3 Other Fabrication Techniques: a short overview

The above sections provide a detailed discussion of electron beam lithography and electron beam induced deposition, examples of top-down and bottom-up nanofabrication methods, respectively. Although these are the two techniques used as part of this project and therefore have received most attention in this review, they are certainly not the only nanofabrication techniques available. Other alternatives include Focussed Ion Beam Lithography (FIBL) and Ion Beam Induced Deposition (IBID), which are similar to the EBL and EBID techniques but use a focussed ion beam instead of electron beam. In the following paragraphs a brief overview is provided of some of the other technologies used for the fabrication of nanoscale patterns [90].

The categorisation of fabrication technologies into either top-down or bottom-up techniques is based on how the nanoscale patterns are achieved. In top-down fabrication methods, a surplus of material is deposited, often in a continuous, even layer, after which the pattern is applied to the layer (e.g. via etching using a lithographically patterned mask). Bottom-up fabrication methods, in comparison, deposit the material immediately in the desired pattern. This can be achieved by having precise patterning equipment available (e.g. EBID), to have controlled deposition of materials, or the target materials can be delivered to a general location, where they are engineered to self-assemble as a result of the nature of the material and its environment itself [123].

Optical lithography

Optical lithography, also called direct laser writing, is a top-down fabrication technique similar to EBL, but instead of using an electron beam, the energy to break and create bonds within a resist is provided by photons in the UV range, with smaller wavelengths providing higher resolution. The resists in this case are referred to as a photoresists, and some resists can be used for both optical and electron beam lithography (e.g. SU8 [115]). It is possible to operate the optical lithography system in a patterning configuration similar to EBL, steering the beam across a sample surface to irradiate patterns in the photoresist, and potential sources of focussed, collimated light are plentiful with a wide selection of lasers available spanning across wavelength and energy ranges. However, as light is limited in the achievable spot-size to half its wavelength according to Abbe's diffraction theorem, it is possible to use masks patterned with a chromium coating to block light in some areas and flood-exposure the entire sample [124] . Masks can be contact masks directly touching the resist of the sample, they can be placed in the focal plane of a beam, or additional optics can be added to achieve higher resolution [123]. Optical lithography is a cheaper alternative to EBL, and when using the flood exposure and mask settings, it is also faster and able to pattern larger areas, especially when a similar pattern is often repeated.

Soft Lithography

Soft lithography is a technology that combines top-down patterning of a pre-formed reusable pattern with bottom-up self-assembly of deposited layers. It uses a reusable master-mould which can be used to transfer molecules or other materials to a target surface in the desired pattern, where the molecules self-assemble into a pattern [128]. A popular material to form the mould is PDMS (poly-(dimethyl siloxane)), the mould itself is often produced using electron beam, ion beam, or optical lithography [129]. An advantage of soft lithography is that outside of the mould fabrication step, the patterning can be performed without requiring cleanroom facilities [123] [127] [129].

Scanning Probe Lithography

An example of a direct deposition technique as a potential alternative to EBID, Scanning Probe Lithography (SPL) is a fabrication technology on the expensive and slow end of the spectrum, but it is able to deposit materials with atomic precision [131]. It uses existing technologies like Scanning Near-field Optical Microscopy (SNOM), Scanning Tunneling Microscopy (STM), or Atomic Force Microscopy (AFM) to transfer a material pattern onto a substrate. A first example is dip-pen technology, in which a solution of the target material is adsorbed onto an AFM tip and then transferred onto the substrate by scanning the AFM tip in the desired pattern [132]. Next to depositing material it is also possible to pattern a layer by removing material by one or multiple passes of the probe over the surface [133], making scanning probe lithography also suitable for precise pattern etching, instead of deposition. SPL can also pattern materials by locally chemically altering a material at the surface, e.g. by local oxidation of a surface [123] [129] [134]. EBID is also able to perform localised etching, by using a precursor gas producing a molecule on interaction with the electron beam which interacts with the target sample surface [90].

Self-Assembly of Molecular Structures

A bottom-up fabrication technique, self-assembling molecules are designed and developed to have the structure they form depend on their molecular properties, and spontaneously assemble as they are brought in contact on the intended surface. An example is the formation of a self-assembled monolayer of MBP0 (4-methylbiphenyl-4-thiol), where the MBP0 molecules automatically order themselves into a Self-Assembled Monolayer (SAM) on a gold-coated substrate as the sulphur in the thiol-group weakly bonds to the gold. This layer can then be strengthened by crosslinking it through electron or photo-illumination to form a membrane, or patterned using electron or photon irradiation [123] [136], [137].

DNA-Guided Self-Assembly

One of the disadvantages of self-assembled molecular structures is that the pattern-forming information needs to be contained within the forming molecules themselves. Unless the desired pattern material is a particularly complex and chemically engineered molecule, the information that can be held by the material is limited. A solution to this problem is offered in the form of using DNA (deoxyriboNucleic Acid) as complex molecule as a self-assembling carrier for a simpler target material to bind to. DNA-guided self-assembly materials make use of the concept of DNA origami, a process of folding DNA to form arbitrary planar shapes [139], and use the DNA structures as a carrier to order and form other material structures, including plasmonic nanostructures [123] [138] [140] [141].

Nanoimprint Lithography

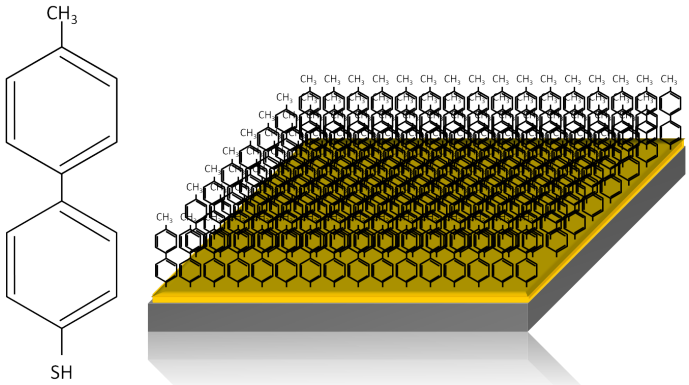

Figure 2.3 – MBP0 molecules automatically orient themselves on a gold surface by loosely binding the sulphur of the thiol-group to the gold, forming a Self-Assembled Monolayer of ordered molecules on the sample substrate.

Nanoimprint lithography uses a master cast of the desired pattern to mechanically emboss that pattern into the desired material. The use of a master cast allows large areas to be patterned quickly, making nanoimprinting a high-throughput, low-cost nanofabrication option [125] [126].

Block Copolymer Nanopatterning

Block copolymer nanopatterning is another technology combining top-down and bottom-up fabrication techniques. Block copolymers can automatically form thin films with small-scale patterns with a periodicity as low as 10 nm, when coated over a substrate surface [130]. It is possible to pre-pattern the target substrate (e.g. using EBL, a top-down fabrication method) to contain markers which can guide and manipulate the block copolymers to self-assemble into complex nanoscale patterns when forming a thin film [123] [130].

Edge Lithography

Edge lithography uses edges to obtain nanoscale structures, either by using the edges as a location ot deposit nanostructures, or to cleave a material and use the properties of the created edge [129] [135].

2.3.4 Fabrication Techniques: Conclusion

Plasmonics research has benefitted greatly from the availability of semiconductor fabrication equipment enabling the provision of nanoscale precision for sample production. The wider research area of nanophotonics includes integrated optics, a field which is as the name suggests closely related to its electronic integrated circuit equivalent. It is easy to imagine that the fabrication requirements of integrated optics samples and designs closely resemble the needs of integrated electronic circuits, and therefore that the available fabrication techniques could serve the field well. Furthermore, it is plausible to imagine how plasmonics based on thin metal patterned layers could be integrated into planar integrated optics designs. However, the scope and needs of nanophotonics, and nanoplasmonics in particular, extends far beyond the planar layered designs of integrated optics applications, and the

limitations of EBL can become restrictive. Regardless of the advantages offered by the availability of a mature fabrication technology, EBL was not developed with plasmonics in mind, and the technique has limitations which places several desired nanoplasmonic design requirements out of its reach. Electron Beam Induced Deposition is one of the technologies that tries to fill some of the gaps left by EBL as a nanofabrication tool. Both techniques were used during the project and are discussed in the following chapter 3 on fabrication. One of the goals of this thesis is to contribute to the discussion on how and where to find the best solutions for nanoplasmonic fabrication needs. Is it better the limitations of semiconductor fabrication methods be accepted, and worked around, or is it preferable for new techniques to be found to overcome the design and fabrication challenges, despite their own limitations and considerably greater fabrication research requirements? Is EBID ready to be used for state-of-the-art applications and can samples fabricated using the technology compete with EBL samples? EBID offers the possibility of easy alignment due to its point-and-shoot configuration, and can achieve high contrast 3D and greyscale writing, but the writing process is slow. The writing parameters are not entirely understood, making the optimisation of fabrication challenging [111]. The purity and conductivity of deposited metal layers is not as high as the metals used in EBL fabrication, and the order in which patterns are written can influence the resulting pattern, which is an extra writing parameter to be taken into account [112]. EBID also places a limitation on the sample itself, as the surface needs to be conductive to avoid charging up of the surface which would interfere with the electron beam and destroy the writing pattern. It is important to note that the two techniques at the centre of this thesis, electron beam lithography and electron beam induced deposition, are not equivalent, nor are they suitable alternatives for each other. EBL is a single step in a multistep process, providing nanoscale patterning ability. The properties of any samples produced using EBL can further be engineered by changing the lithographic resists, material deposition techniques, and etching processes, etc. In contrast, EBID is a point-and-shoot single step deposition and patterning process, comprising not just an alternative to the EBL step, but including the deposition and etching steps as well. As a result, an exact comparison between the two techniques is difficult, but there is merit to examining the properties of the two techniques, as both contain a step in their respective fabrication processes resulting in the achievement of nanoscale patterns. Both EBL and EBID have their own suitable applications, and it is unlikely at the moment that EBID would be seen a a suitable alternative for EBL in any technology where EBL limitations do not provide an obstacle. Instead, EBID can prove its use in those areas where EBL limitations prove insurmountable or severely limiting, and EBID can exhibit the potential of its fabrication properties.

Chapter 3

Fabrication

This chapter will provide detailed descriptions of the fabrication methods and techniques used in the different fabrication sections of the project: Electron Beam Lithography (EBL) and Electron Beam Induced Deposition (EBID). The first part of the chapter will discuss the fabrication techniques used to make gold nanoplasmonic structures through EBL. As this method is more conventional and established in the group, the focus of the project did not lie in the development of recipes, but the specific application of these fabrication methods to the production of chirped gratings and other designs. The section will start with a general description of the fabrication procedure, followed by a detailed analysis of the design and fabrication of chirped gratings.

In contrast with the many-step, well-established Electron Beam Lithography method, the second part of this chapter will discuss Electron Beam Induced Deposition, a single-step point-and-shoot method to write nanoscale metal structures directly onto a substrate. The technology was newly available to the Synthetic Optics group, and as a result the project focussed on the development of the fabrication procedure and recipes, and the exploration of novel opportunities EBID offers.

This chapter on fabrication will conclude with a comparison of the EBL and EBID techniques as methods to achieve nanoscale structures, offering an overview of their benefits and drawbacks, and suitability in different situations.

The processes described below detail a procedure to fabricate nanoscale metallic features on flexible membranes, the flexible membranes being held on a rigid substrate throughout the fabrication process to ease handling and be compatible with the fabrication equipment. Although it is not discussed in this thesis, the eventual goal is to lift the metallic nanostructures on the flexible membrane off the rigid substrate, and to utilise the beneficial characteristics of the resulting (flexible) photonic membranes, specifically their conformability to a range of shapes and environments, and their tunability through manipulating the shape of the membrane (stretching, folding, bending, rolling, etc.).

3.1 Electron Beam Lithography-based Fabrication of Gold Plasmonic Nanostructures

The process of fabricating gold nanoplasmonic structures using electron beam lithography uses a combination of standard methods and materials. Gold has traditionally been a preferred choice for many plasmonic applications despite its higher plasmonic losses than silver, due to its comparatively low reactivity and ideal plasma frequency [21]. Electron beam lithography is a well-established method of patterning materials on the nanoscale. The gold structures are created using a multi-step etch-back method, by depositing even layers and etching away exposed, unrequired material. A brief outline of the fabrication process is provided below, followed by a detailed description of the different steps and their significance.

3.1.1 A Brief Overview of the EBL Fabrication Method

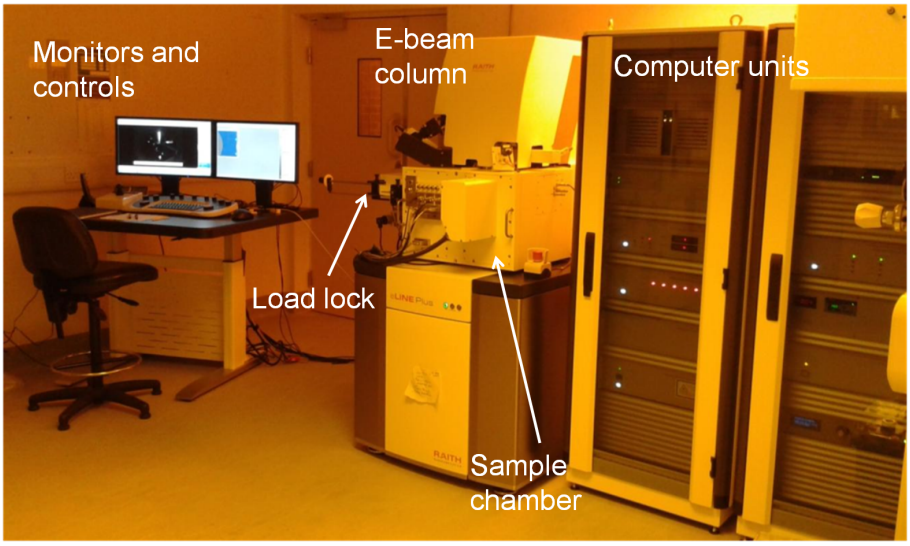

Figure 3.1 – Photograph of the Raith e-Line Plus Nanofabrication tool setup in the cleanroom, comprising the computer units, monitors and operating controls, the electron column, and sample chamber with load lock. The equipment is used for both standard electron beam litography and electron)beam induced deposition, the 2 main fabrication methods discussed in this thesis.

The nanoplasmonic samples obtained for this project through electron beam lithography were produced on silicon or glass substrates that act as carriers for the polymer membranes. The samples were flat and tended to have dimensions between 0.5 and 2.5 cm. First, the substrates were cleaned in acetone and isopropyl-alcohol (IPA) in an ultrasonic bath. A sacrificial lift-off layer of Omnicoat [114] was spincoated on top of the cleaned substrate, followed by a layer of SU8 polymer [97] [115] [116], which forms the flexible polymer membrane to carry the nanoplasmonic structures.

Once the membrane fabrication had been completed, an even layer of gold was deposited onto the membrane, using electron beam evaporation. In order to be able to pattern the gold, a photoresist mask (SU8, [115]) was spincoated on top of the gold, and this photoresist was subsequently patterned using electron beam lithography (EBL), see figure 3.1, and developed to remove the unexposed SU8 material. The remaining SU8 patterns acted as a mask, and creating patterns in the gold by shielding

part of the gold layer, while the exposed gold was etched away using a reactive ion etcher (RIE).

The resulting product was a nanoscale gold pattern on top of a polymer membrane, carried by a rigid, flat substrate. By dissolving the Omnicoat [114] layer, the flexible SU8 [115] membrane with gold patterns could be lifted off its rigid carrier substrate.

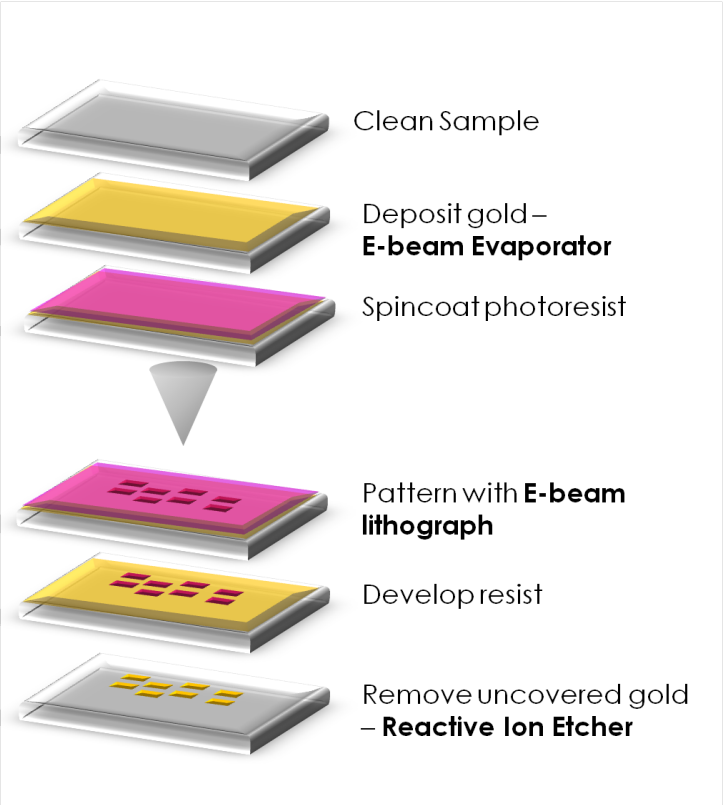

Figure 3.2 – Overview of the main step of a standard top-down etch-back plasmonic fabrication process, using electron beam lithography.

3.1.2 Choice of Substrate and Cleaning Procedures

Electron beam lithography relies on precise focussing on the sample surface. It is therefore necessary to start with an even, flat, and clean substrate, as any imperfections and impurities will have a knock-on effect on the subsequently added layers. The necessity for this clean sample, and the relative size of dust particles, dirt, and impurities compared to the nanoplasmonic features, means a clean environment is necessary, and because of this the entire fabrication process takes place in a cleanroom, a low-dust environment with pressure, temperature, and humidity control.

In order to facilitate sample manipulation throughout fabrication and characterisation, having a rigid and sturdy substrate helps to protect and preserve the fabricated samples. The rigid substrate is also essential during several of the fabrication steps described below. The nanoscale features themselves are patterned on top of a flexible photonic membrane which can be removed from the rigid substrate. The flexible membrane carrying the metallic features can be used to transfer the nanoplasmonic functionality to a wide range of materials and shapes by conforming to the dimensions of the target

object. The flexible carriers can themselves also be patterned to form micro-sized carriers, as shown in figure 3.10, which can suspend the plasmonic structures they carry in liquid, and position them precisely e.g. with the help of optical tweezers.

Depending on the need of the application of the sample, the substrate might have different requirements regarding conductivity, transparency, reflectivity, thickness, size, etc. Throughout the project, the main substrates used were (100) silicon (Si), which facilitates straight cleaving to obtain clean sample edges, by cleaving along the (100) lattice direction indicated on the wafer, silicon-dioxide-coated silicon (also referred to as silica- or SiO_2-coated silicon) to have an non-conductive substrate while retaining some of the cleaving and reflectivity characteristics of the silicon substrate, and glass (Agar coverslips, No 0 and No 2 [113]), which allow for uniformity in sample sizes, high optical transmission, and a thin substrate (No 0, 0.08-0.10 mm; No 2, 0.19-0.23 mm).

The abovementioned substrates were all cleaned using the same procedure. First, the sample is submerged in a beaker filled with acetone, and placed in an ultrasonic bath (see figure 3.3 (c)) for 3 to 5 minutes. The sample is then moved into a different beaker filled with IPA, and placed into an ultrasonic bath for another 3 to 5 minutes. Acetone removes organic impurities and IPA removes the remaining acetone from the surface and further removes impurities from the surface. The sample is subsequently removed from the IPA and dried using a nitrogen (N_2)-gun, to minimise the residue of impurities on the surface.

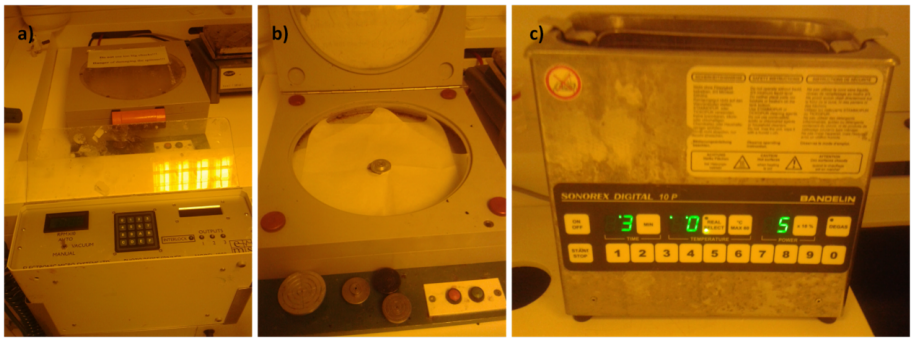

Figure 3.3 – (a) and (b) show contain images of a spincoater used to cover samples in a thin, even layer of photoresist (e.g. SU8) or sacrificial layer (e.g. Omnicoat); (c) shows an image of the ultrasonic bath used during the cleaning procedure of the membrane.

3.1.3 Fabricating the Sacrificial Layer and Polymer Membrane

As mentioned above, the flat substrate is meant as a carrier for the flexible polymer membrane supporting the plasmonic features during fabrication, as well as during parts of characterisation and testing of the sample. The clean surface of the substrate has been prepared to receive the layers which will form the sample membrane. In order to access the properties of the membrane without interference or hindrance from the carrier substrate (e.g. its flexibility, transparency, etc.) it is necessary to incorporate a method to remove the membrane from the substrate. For this, a sacrificial layer, also referred to as a lift-off layer, is added between the substrate and the polymer membrane. The material used for this sacrificial layer is Omnicoat [114]. It has the desired properties of not reacting to any of the chemical treatments or other production steps performed on the sample, so it

stays intact throughout the fabrication and use of the sample, and can be removed using chemicals (e.g. n-methylpyrrolidone [118], MF-319 Developer [119]) which do not destroy the finished sample.

In order to fabricate the sacrificial layer, the substrate is placed in the centre of a spincoater on an appropriately sized chuck, and held in place using vacuum grip. Using a pipette a thin, even layer of Omnicoat is applied to the surface of the substrate. The Omnicoat is then spincoated on the surface at 1000rpm for 1 minute, after which it is baked for 1 minute at 230°C. Once the Omnicoat has cooled down to room temperature, it is ready to receive the next layer.

The material used to form the polymer membrane is SU8 2000.5, an epoxy material that functions as a negative photoresist and can be crosslinked using UV, electron beam or X-ray radiation [115]. The Omnicoat covered substrate is placed back on the spincoater chuck with vacuum grip, and covered in a thin, even layer of SU8, using a pipette. Depending on the desired thickness the SU8 is spincoated using different spin-speeds. As the SU8 membrane only acts as a carrier for the nanoplasmonic structures, precise control of the thickness of the membrane is not critical. However, a membrane which is sufficiently thin to maximise its flexibility and minimize its influence on the environment of the nanoplasmonic structures it carries, yet also strong enough to withstand careful handling during measurements and tests, is desirable. To obtain this it was found that a membrane resulting from spincoating SU8 2000.5 at 5000rpm for 1 minute and soft-baking for 2 minutes at 100°C gave a satisfactory result, with a thickness around 500 nm.

After soft-baking the SU8, which is a negative photoresist, it needs to be irradiated in order to form a strong, crosslinked membrane. For this fabrication step, a UV mask aligner provides the ability to provide sufficient radiation to crosslink the entire surface of the sample in an even manner in a short amount of time. The sample is placed under the UV lamp and flood-exposed for 2 minutes, and subsequently post-exposure baked for 1 minute at 90° C and 4 minutes at 100°C. The small ramp-up in temperature helps to avoid the formation of bubbles in the membrane.

The quality of the membrane can be roughly assessed visually, as any sizeable dirt particles present would leave visible traces on the membrane during spincoating and baking. Unevenness in the membrane thickness or height can be seen as thin film interference rings, patterns, or other lack of uniformity in the colour of the membrane. If the quality of the SU8 membrane is not acceptable for the desired application, it is possible to remove it by submerging it in EC (ethyl lactate) for a minute in an ultrasonic bath. However, this must happen before the UV exposure step, as a crosslinked SU8 membrane is very difficult to remove with conventional chemical methods [115].

Having completed the formation of the basic membrane, the next step involves applying a layer of metal to be used as the source material for nanoplasmonic structures.

3.1.4 Metal Evaporation to achieve Gold Deposition

As discussed above, the gold nanostructures will be produced using an etch-back method, therefore the next step in the process is to fabricate an even layer of gold to use as a base for etching. In order to

obtain sub-nanometre precision in the control of the thickness of the layer, a technique called electron beam evaporation is used. The equipment used (see figure 3.4) is able to deposit material with nm precision. The thickness is measured by a quartz crystal microresonator, which can determine the deposited layer thickness on the crystal by measuring the resonance frequency of the quartz crystal, which changes as more material is deposited.

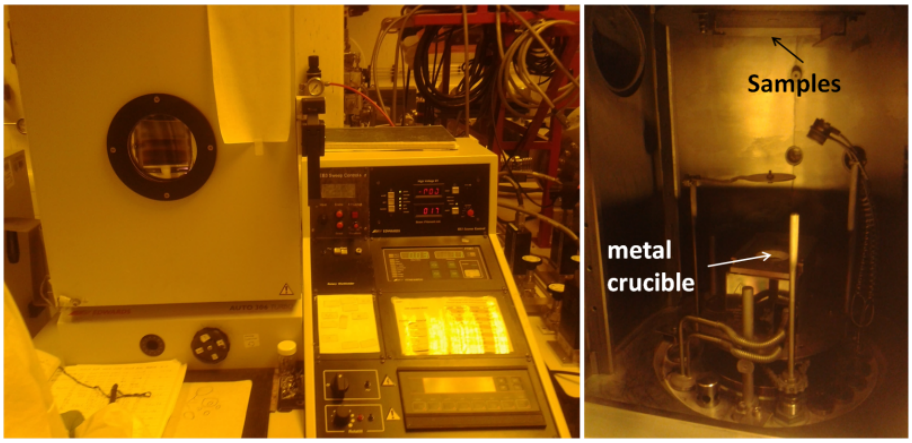

Figure 3.4 – The electron beam evaporator. The image on the left shows the external view of the sample chamber and the operating panel of the evaporator. The righthand image shows the inside of the sample chamber, indicating the location of the sample holder (suspended upside down) and the metal crucible containing the source material for the evaporation process.

The quality of the deposited material depends on the quality of the substrate surface, the purity of the source material, the deposition rate, the pressure in the chamber, etc. A paper by K. McPeak et al. [120] discusses ways to improve deposition of different types of metals and discusses the influence of different environmental parameters on different materials. Although the article discusses thermal evaporation settings, the general findings are applicable to electron beam evaporation as well. It states that when deciding on a deposition speed, a optimal balance must be reached between the detrimental effects caused by residual gases and impurities remaining in the chamber, and diffusion rate of the newly deposited atoms. At lower deposition speeds, the amount of impurities being adsorbed onto the sample surface during deposition is higher, decreasing the grain size and quality of the deposited metal. At higher deposition speeds, the metal atoms have less time to diffuse through the metal before being hit with other atoms, reducing the grain size of the resulting deposited material. As gold is a noble metal it is quite unreactive, meaning that the deposition speed can be kept low without much detriment to the overal quality of the deposited layer. An additional benefit of this low deposition speed is that less material is lost during ramp-up of the evaporator, which is an important factor to consider when working with an expensive source material like gold [120].

Gold deposits well on an SU8 membrane, so the samples produced as previously described can be loaded without need for further treatment. The samples are secured to a sample holder and hung upside down into the evaporation chamber (see figure 3.5). Below the sample holder a crucible filled with gold granules will act as a source material for the evaporation process (see figure 3.4). The chamber door is closed and the room is pumped down to a vacuum around the order of 10^{-6} mbar. This pumping down process takes a minimum of 6 hours but is ideally done overnight (12 - 14 hours) to achieve a lower vacuum, which leads to better deposition quality.

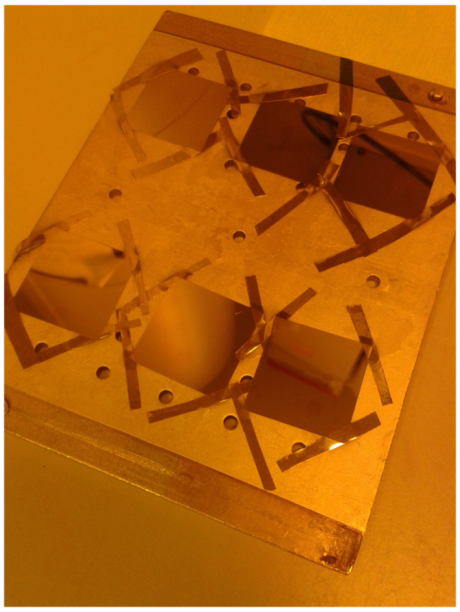

Figure 3.5 – Samples on the electron beam evaporator sample holder after deposition of 40 nm Au, on SU8 on glass samples. As the samples are suspended upside down in the chamber, they are held in place using blue adhesive tape.

Once the chamber has reached the desired vacuum pressure, the electron beam evaporator can be turned on. An electron beam evaporator works by evaporating the source material using an electron gun. An electric field is used to create an electron beam which hits the crucible and heats up the material, in this case gold. The evaporation and resulting deposition rate can be controlled by adjusting the strength of the electron beam through its current. In order to obtain a high-quality deposited layer, uniform across all the samples, several steps can be taken to improve the evaporation process. The sample holder is rotated to assist making the deposition as even as possible across the sample(s). Before starting deposition, the chamber and current need to be gradually ramped up to their final value, as sudden current increases or heating of the metal can cause sparks which can disturb the low vacuum in the chamber. Because of this, the electron beam is established slowly to avoid fast changes in the chamber could cause disturbances and influence the quality of the deposition, or cause damage to the chamber or source material. The system needs time to condition the source material and to allow the deposition rate to stabilise, as this can fluctuate during the ramp-up, even when the current is stable. During this ramp-up process a cover blocks the path from the crucible to the samples to shield them against any unwanted and uncontrolled material deposition.

Once the current has been set to achieve the desired deposition rate, which is usually around 0.04 $\frac{nm}{s}$ to 0.1 $\frac{nm}{s}$ the cover can be removed to unblock the path from the crucible to the samples. A quartz crystal inside the evaporator chamber allows the deposition rate to be measured with nanometre accuracy. Depending on the specific application for gold-on-SU8 samples, a layer between 40 nm and 100 nm thick was deposited. The pressure was kept below 2 10^{-5} mbar during the evaporation process. Once deposition is complete, and the sample is removed from the chamber, the metal is ready to be coated in a photoresist mask.

3.1.5 Electron Beam Lithography Patterning Procedure

Electron beam lithography is a fabrication procedure which has been established and developed over several decades [121]. The technique uses an electron beam focussed on the surface of a material which reacts to the incident electrons, often a photoresist, to write patterns and create a mask with the desired nanostructures. The patterns are written by deflecting the electron beam and by moving the sample relative to the beam. While all steps in the process influence the quality of the finished sample, which in turn has an effect on the overall performance of the sample, it is the electron beam exposure step which determines the resolution and quality of the pattern itself. The quality of the exposure depends on the technical performance and capability of the equipment, and the parameters set by the user.

Photoresist mask

In order to pattern the deposited gold layer, it needs to be covered in a photoresist, or photomask, which will be lithographically patterned and developed, after which un-crosslinked parts of the mask will be removed to remove parts of the gold surface.

In the majority of the samples produced during the process, SU8 [115], which forms the polymer membrane carrying the gold layer, is also used as the lithographic photoresist mask. As a negative photoresist it is ideally suited to form high contrast, nanoscale structures. SU8 is referred to as a negative photoresist because the electron beam irradiated SU8 crosslinks and remains on the substrate as a membrane after development. Alternatively, positive photoresists may be used (e.g. PMMA), in which case a solid membrane is formed, and parts exposed to the electrons are removed during development. This type of photoresist is ideal to use for patterns which require small-scale gaps, holes, lines, etc. in a mostly solid layer.

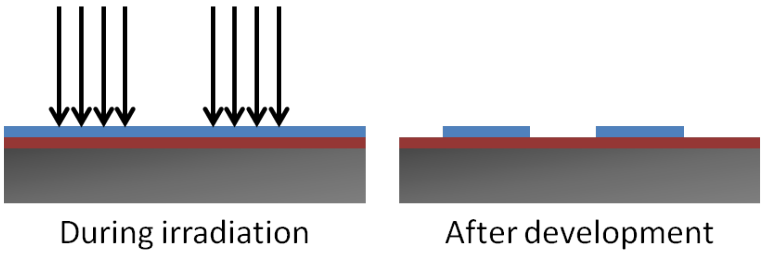

Figure 3.6 – A negative photoresist keeps the irradiated material after development. This pattern can then be used as an etching mask, removing the exposed material.

During the electron beam exposure of a negative photoresist, high energy electrons are accelerated towards the sample by the Extremely High Tension (EHT), a high voltage value up to 30kV for the Raith e-Line lithograph. The Gaussian beam of accelerated electrons is formed in the electron gun column of the lithograph, and when the high energy electrons hit the sample, most of them penetrate through the sample without coming to a halt. Some scatter off particles inside the photoresist and create secondary, lower-energy electrons as they do so. It is these secondary, scattered electrons which are able to break bonds in the SU8, exciting an atom within the molecule, making it susceptible to bond to neighbouring atoms, both within and outside the same molecule. As the energy dissipates, the molecule returns to its ground state by reforming a bond, some returning to the original single molecule configuration, but others bonding with atoms of neighbouring molecules instead. The

repeated occurrence of this process causes the molecules within the exposed areas to link together and form a crosslinked layer, which after development, as outlined in section 3.1.5 above, form a hard-to-remove polymer material, functioning as mask pattern [122].

Electron Beam Lithograph

The above paragraphs describe how a precise and accurate pattern is created by writing patterns into photosensitive materials using electron beams. The true power of this technique lies in the precision and accuracy which can be achieved when writing structures on a nanoscale, and the technological expertise present to produce a machine capable of performing these actions: an electron beam lithograph. It requires the creation of a stable, precisely focussed electron beam, and sub-micrometer control of the movement of the sample stage to distribute and position the written patterns across the sample surface.

The electron beam lithography system equipment was replaced during the project. The old equipment was a modified SEM (Leo Gemini 1530) combined with a RAITH ELPHY Plus pattern generator. The new system, used for the majority for the samples presented in this thesis is the RAITH E-Line Plus Nanofabrication tool (see figure 3.1) [143], a modified SEM (scanning electron microscope) with additional Nanomanipulator features and Gas Injection System, discussed in more detail in section 3.2. Instead of scanning a Gaussian electron beam across an area to form an image, a modified SEM lithography system is operated through a pattern generator to produce an irradiation pattern on the sample surface [122].

In order to write precise features, very fine and accurate alignment is required, for the beam to be correctly focussed on the sample surface, and the features to be written properly aligned with each other. The setup requires both the SEM alignment settings and pattern generator parameters to be set to operate the lithograph. Samples are loaded into the chamber via a loadlock, to avoid exposing the sample chamber to room pressure conditions. Once the sample is loaded the SEM can be aligned, setting the vertical position of the stage and related working distance, the aperture of the column, and EHT voltage. The system also needs to have its current calibrated to the sample conditions, and the system is focussed and adjusted for aperture and stigmation alignment by writing spots at magnification values of 40 000 and more, creating sharp, round irradiated patterns.

Once the SEM is sufficiently aligned, any settings related to the exposure and patterning process can be set. To pattern a sample, the electron beam is deflected by electron optics to navigate across a write field and form the intended features. The size of the write field is set by the user and linked to the magnification and resolution at which the pattern is written. Between write fields, the sample stage is moved, which can lead to stitching errors (see figure 3.7). A write field alignment procedure is performed before each exposure. Apart from needing high quality beam and sample alignment so the electron beam can function accurately and precisely, the parameters linked to the beam and its movement guided by the pattern generator need to be determined as well. The patterning parameters are a set of interrelated values which determine how the machine writes features during the exposure. They influence the speed, dose, and quality of the written features. They include the dwell and settling time, different dose values, step size, etc. need to be set as well. A more detailed description of parameter settings is provided in section 3.2

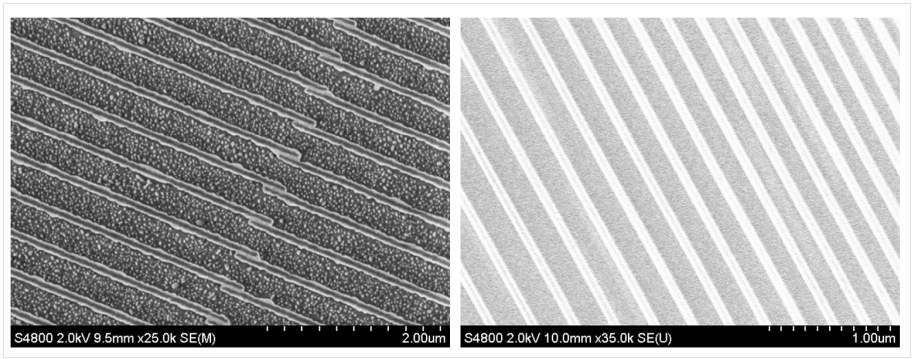

Figure 3.7 – Illustration of alignment errors which can occur when patterns are distributed across multiple write fields (left image), compared to a linear grating with good exposure and alignment settings.

Mask Development

Once the patterning is complete, the mask is removed from the electron beam and, if the used material is SU8, the development includes post-exposure baking at 100°C for 2 minutes. This solidifies the crosslinking of the exposed areas. The sample is then submerged in EC (ethyl lactate), a developer which does not affect any of the other layers of the sample. The EC removes any SU8 which has not been crosslinked. As the gold layer is fragile, no ultrasonic bath is used, but gentle stirring or swirling of the sample inside the EC beaker can help advance the removal of the SU8. The sample is initially submerged for 45 seconds, removed from the EC, washed in IPA, which removes any EC remnants, and dried with a nitrogen gun. The sample is then inspected under an optical microscope to assess if all unexposed SU8 has been removed. If this is not the case, the sample is placed back in the EC for another 10-15 seconds, and the process is repeated until the result is satisfactory. If mistakes are made when setting the patterning parameters of the lithographic writing step, overexposure causes additional areas of the resist to be unintentionally crosslinked, as can be seen in the lefthand and middle SEM images of figure 3.7.

This is the first time it is possible to observe the irradiated structures, as the crosslinked SU8 features on top of the gold layer are clearly visible under the optical microscope. Some issues or errors can be noticed at this point, e.g. relating to the SU8 development, dosage, or alignment, but for a detailed examination of the written structures, analysis under the Scanning Electron Microscope (SEM) is necessary.

3.1.6 Reactive Ion Etching

After the electron beam irradiated pattern in the photoresists mask has been developed, the sample is ready for the final step in the fabrication process: etching away the exposed gold. Reactive ion etching is a dry and directional etch, ideal for removing the exposed gold while leaving the masked portions of the gold untouched.

For the removal of exposed gold, an argon plasma is used, as it has a lot of desirable properties for the task at hand: argon is a noble gas, and relatively cheap, it will not react with the gold or any

other part of the sample, and performs a purely physical and very directional etch.

RIE

A custom-built Reactive Ion Etcher (RIE) was used to perform the etch (shown in figure 3.8). When the machine is not in use, the reaction chamber is held under high vacuum to keep it as clean as possible. A butterfly valve is used to separate the sample chamber from the turbo vacuum pump, which is turned on continuously to reduce the wear on the pump and save time loading and unloading the chamber.

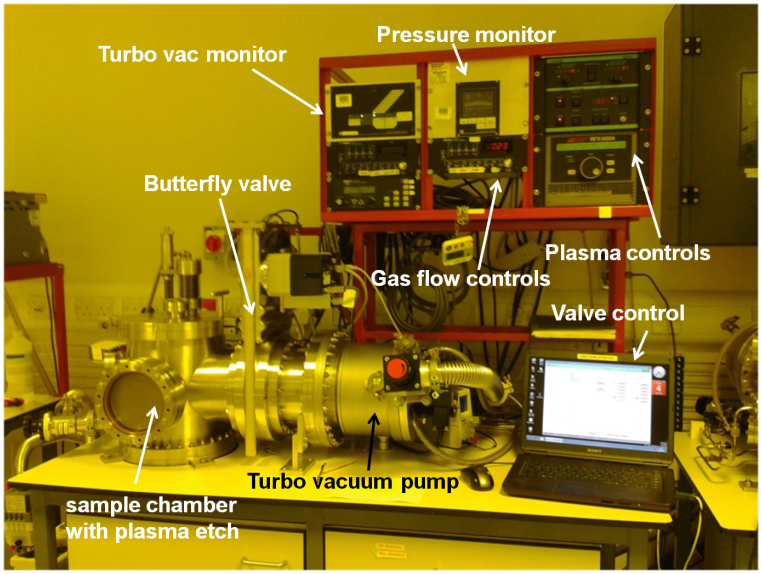

Figure 3.8 – Image of the Reactive Ion Etcher (RIE) in the cleanroom. The sample chamber is the vertical cylindrical chamber on the lefthand side of the equipment. The horizontal cylinder on the right is the turbo vacuum pump, separated from the sample chamber by a butterfly valve (the rectangular dividing panel between the two cylindrical structures). The butterfly valve is operated by the laptop on the right. The equipment on top of the setup is used to operate the gas flow, monitor the turbo vacuum load, and control the voltage settings to generate the plasma for the etch.

Once the sample has been placed into the chamber, and the chamber has been brought down to a satisfactory low base pressure (around 3 e^{-6} Pa = 3 e^{-8} mbar) by a roughing vacuum pump, a 500 (50 %) argon gas flow is set using a flow regulator, and the butterfly valve is partially lowered to allow the argon to bring the reaction chamber to a constant pressure of 5 e^{-2} Pa (5 e^{-4} mbar). The argon gas is ionised using an Radio Frequency (RF) source, adjusting the setpoint power to achieve a -333V DC bias (usually this is achieved for a power of 19 W), to create an argon plasma. The electrons dislocated from the argon atoms by the RF field accelerate following the force of the field, as an electrically insulated plate carrying the sample collects many of the accelerated electrons, building up a highly negative charge. This charge creates a DC voltage bias, which accelerates the positively charged argon atoms towards the plate and the sample it carries. The value of the DC bias determines the acceleration and impact strength of the ions, and is regulated by the parameters in the chamber (pressure, gas flow, RF power, and frequency). During the etch, the heavy atoms hit the sample, and physically sputter the surface, removing the gold. As argon is a noble gas, the plasma does not chemically react with the sample, and the resulting etch is purely physical and anisotropic, referred to as ion milling, which etches vertically down.

The etch time and RIE settings varied slightly throughout use, as several parts were replaced during the process and wear on system components caused the parameters to shift with time. To etch 40 nm of gold with the above parameters, an initial etch time of 11 minutes was set. If after visual inspection of the sample gold residue was found on the exposed surfaces, the sample was be placed back in the RIE for an additional etch, in 30 seconds to 1 minute increments. The process of loading, pumping down, and unloading the RIE makes these incremental etch steps time consuming, but the risk of overetching and consequentially removing the masked features along with the exposed areas, would destroy the sample, and would be a great loss at such a late step in the fabrication process.

Once the excess gold has been removed from the sample, the fabrication of a single layer of gold structures on a polymer membrane is complete. If only a single layer of structures in needed, the sample is ready for characterisation, measurement, and testing as described in chapter 4. Optional further fabrication steps are discussed below.

3.1.7 Lift-off

In order to access the flexible properties of the membrane, and to remove the influence of the rigid substrate carrier, the sample can be lifted off by removing the sacrificial Omnicoat [114] layer added during one of the first steps of the fabrication process. If a crystalline substrate was used, the edges of the sample should be cleaved in order to create clean access to the Omnicoat layer for the solvent, as the edges of the sample could have been covered in SU8 [115] or gold during subsequent deposition steps, blocking the etchant from accessing the Omnicoat layer. To remove the Omnicoat, NMP (N-methyl-2-pyrrolidone) is used [118], a solvent able to remove the Omnicoat layer while keeping the gold and crosslinked SU8 structures intact. MF-319 [119] can be used as an alternative solvent to NMP. Figure 3.9 contains images of a gold-covered PMMA membrane formed on a glass substrate during and after liftoff to illustrate the process.

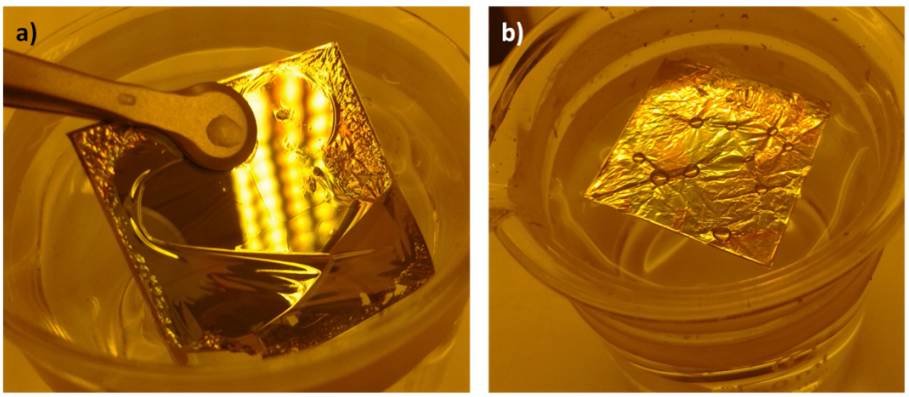

Figure 3.9 – Images of a gold-covered PMMA membrane fabricated on a glass substrate during (a) and after (b) liftoff.

3.1.8 Multilayer Samples

In some cases, all of the required features cannot be fabricated in a single run of the lithographic procedure. It is possible features need to be made from different materials (e.g. see the gold on SU8

ribbons in figure 3.10), require different material thicknesses (e.g. 40nm and 100 nm gold), different mask coverage (e.g. positive photoresist in case large areas need to be unexposed), or need a spacer layer between them (e.g. chirped gratings). In these cases, the lithographic and etching steps of the above process need to be repeated several times. The nano ribbons of figure 3.10 are designs of ribbons to be trapped horizontally by optical tweezers against their natural alignment direction, using gold discs as plasmonic trapping handles.

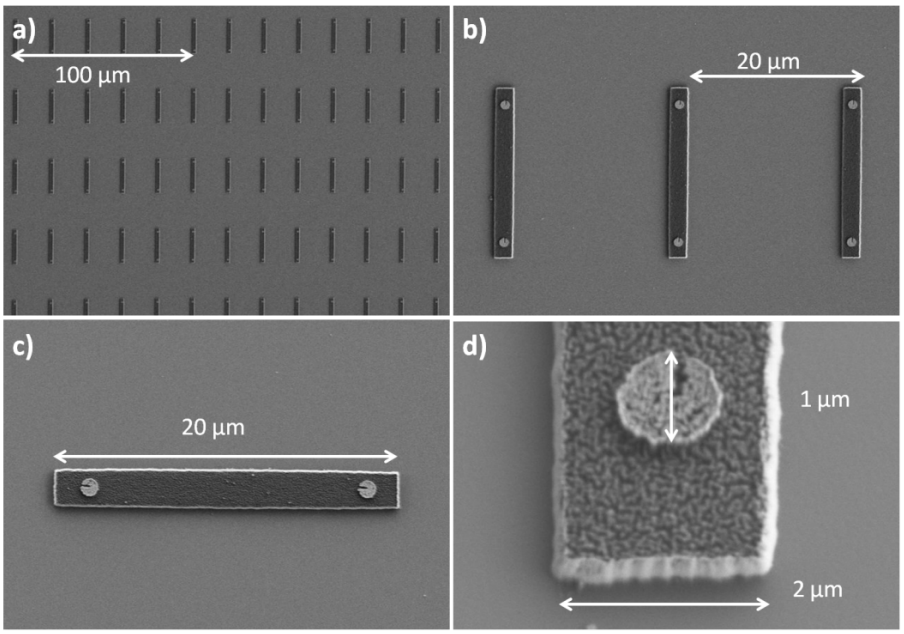

Figure 3.10 – SEM images of gold handles on SU8 membrane ribbons. The SU8 ribbons and gold handles are produced in separate lithography steps, and require precise alignment. The ribbons can be used lifted off and suspended in solution, where the gold handles can be used as optical trapping handles.

Spacer Layer

In some cases a spacer layer might be required between the different patterned layers, to create a physical separation. One potential application for a spacer layer is to act as a physical separation between two perpendicular EBL gratings, to allow the light to be diffracted by the first grating before reacting with the second grating. A spacer layer has the added benefit of evening out any bumps created by the pattern of the first layer, allowing the subsequent metal layer and photomask to be deposited on a even and flat surface, which should increase the quality of the resulting irradiated pattern. Often thicker SU8 is used as a second layer, the thickness of which can be controlled by mixing the correct fractions of SU8 2000.5 [115] and SU8 2050 [117] to thicken the layer, and cyclopentanone to make it thinner. The spacer layer will also have to be flood exposed to UV in order to crosslink it.

Multiple Metal Depositions

The second or later metal layer deposition requires a repeat of the gold layer deposition step (see section 3.1.4), although different materials and/or thicknesses can be used as well. In order to lithographically pattern the new metal layer, another photomask is spincoated on top of the metal, to pattern, mask, and etch.

Alignment Difficulties due to Metal and Spacer Layers

In order to enable precise alignment of the new lithographic patterns on the structures in the layer or layers below, alignment markers can be added to the electron beam lithographic pattern written in the previous layers alongside the desired structures, their precise position relative to the features known. When the sample with second or later photoresist layer is loaded into the e-beam an extra alignment step needs to be performed in order to map the new features around the old ones. Usually a three-point-alignment method is used, where three non-collinear points of the 2 layers are mapped precisely on top of each other, resulting in the layers being aligned in x and y. Difficulties can occur during this step as the alignment markers are written in the same, often thin, first photoresist mask layer, and are covered and hidden under layers of metal and SU8, which can make finding them a challenging or even impossible task.

3.1.9 Conclusion on EBL Benefits and Drawbacks

The above sections describe the standard fabrication steps to obtain a nanoplasmonic sample through electron beam lithography. The process follows a series of well-understood steps, part of a technology that has been used and improved in industry for decades [121]. This means that a successful sample can deliver high-precision nanoplasmonic structures fabricated from high-quality materials. However, the process described above is time consuming, a single sample can take several weeks to produce, when taking into account equipment availability. Each individual step also has the potential to fail or deteriorate the quality of the sample due to errors, either human, equipment, or environment based, which lowers the sample yield and increases the effective sample production time.

In an ideal time-effective scenario a sample could be produced in 3 days: an afternoon to prepare the substrate and membrane, a metal evaporation with the chamber vacuum pumping down overnight and morning metal evaporation, the afternoon to deposit the photoresist, followed by an evening EBL setup and overnight electron beam write, developing the sample in the morning followed by a reactive ion etch. During these 3 days the fabrication is work-intensive, requiring constant attention and active input during every step of the process, as loading, pumping down, and write periods are scheduled overnight. If the availability of equipment and unpredictable setbacks are added in (e.g. sudden cleanroom closure, bad spincoating, RIE down for service etc.), the delay in a single step has effects on the entire fabrication pipeline, as there is no point loading a sample into the e-beam lithography system if the sample does not have a photoresist coating, because the cleanroom was down that afternoon. This can cause the fabrication of a single sample to take several weeks.

Electron beam lithography also has limitations in its abilities. It is not a great tool for greyscale or 3D writing as it works with planar samples and single layers at a time, and precise alignment between separate lithographic patterning steps can be a challenge. There is no opportunity to test doses and parameter settings on the same sample, so separate samples are required to test recipes, and small differences between individual samples or writing conditions cannot be taken into account, which can cause writes to fail.

To summarise, electron beam lithography is a very powerful, well-established, but time consuming fabrication technique, delivering samples with high quality materials able to form high precision nanoscale structures. Using a sacrificial layer it is possible to release flexible polymer membranes

from their rigid carrier substrates needed to be used with semiconductor techniques designed for flat, solid samples. Fabrication throughout this project has been focussed on gold metallic structures, but the same method, when using different evaporator materials and etch settings, can be used to fabricate a whole range of different materials.

3.2 Example Application: Chirped Gratings

The EBL fabrication method described in section 3.1 was used to fabricate a range of different sample designs and tests throughout the project, including membranes suspended on top of pillars, metal contact masks, linear gratings, and chirped gratings. The following sections will go into more detail on chirped gratings as an application and as a specific example of using electron beam lithography for fabricating samples: chirped diffraction gratings.

3.2.1 Chirped Gratings for Generating a 2D Light Array

In order to take and recreate a 2D image of a subject there is a need to collect visual information and to link this collected visual information to a 2D coordinate. If an image of a moving subject is required the information of each 2D coordinate pixel of the complete image also needs to be linked temporally. For moving subjects the processing of such an image needs to happen sufficiently fast so that it can be repeated to obtain enough consecutive images to create a moving picture. The use of cameras is commonplace in a wide range of applications and they are present in many different shapes and sizes throughout many aspects of our everyday lives, providing different types of images depending on their intended use, and with those different uses come different requirements regarding many properties of cameras. One area of applications which requires a range of cameras with particular sets of characteristics is the medical sector, and the example discussed in this section aims to provide for the requirements of a particular type of camera used in medicine: the endoscope. Endoscopes are cameras used to look inside the human body, and therefore require the ability to be navigated inside the human body while causing minimal disruption, i.e. they should be small and flexible [17].

Based on these required characteristics, and ideal candidate for use in endoscopy-equipment might be optical fibres, which are thin, flexible, and an excellent carrier of light along a narrow path. However, optical fibres are not without their drawbacks. There are many types of fibres available, depending on the light carrier needs, but in general they are often divided into 2 categories: single mode fibres (SMF) and multimode fibres (MMF). Single Mode Fibres are notoriously difficult to guide light into, because of their narrow angle of light acceptance, making them bad at collecting optical information from a wider field of view. When used in endoscopes they would have low light capture efficiency and a narrow field of view. Multimode fibres are better at capturing light more efficiently and from a wider viewing angle, but as the light travels through the fiber, modal dispersion causes the information to spread over time, with wider angles of acceptance leading to more dispersion. Any spatial information will get lost when travelling through the fibre, as direction of incident light cannot be encoded during propagation through the fibre [18].

Potential solutions to the problems presented above could be to use a bunch of separate single mode fibres, to add in optical elements to increase the field of view and coupling of light into the fibre, or

to add active elements to the capturing end of the fibre to scan a wider surface and retain spatial information. All of these solutions have the side effect of increasing the volume of the equipment, so although a set of 1000 single mode fibres would in all probability provide a detailed image of observed matter, the circumference of such a device would make it unsuitable for use in endoscopic applications. In order to keep the diameter small, an ideal solution would be to have a single fibre with a wide viewing angle in which it captures light, and is able to maintain spatial information as light travels through the fibre. As we have established above, any information relating to the direction in which light hits the fibre is lost, but one characteristic of light that does not get scrambled while travelling through a fibre is the wavelength. Considered along the length of fibre required for endoscopic applications, propagation losses along the optical fibre are usually negligible, so when a certain amount of light of a specific wavelength enters that optical fibre, that same amount of light will reach the end of the fibre. As light of different frequencies does not interact while propagating through a fibre, information encoded in the intensity of a specific wavelength captured by the fibre can be retrieved at the other end of the fibre.

It is this property of light propagation in fibres which presents a potential solution for endoscopic applications and which has inspired the development of the chirped diffraction gratings below. If broadband light is sent into a fibre, and the light is split up with each wavelength sent in a unique direction, the returning signal can contain spatial information. In order to create the one-to-one wavelength to location mapping whilst keeping the size of any optical elements to a minimum, plasmonics and its ability to control and manipulate light at the nanoscale offers a necessary properties and potential in the form of chirped diffraction gratings. Chirped gratings on a flexible substrate are presented below as a possible solution for planar one-to-one wavelength-to-location mapping. It will be shown that chirped gratings can be seen as a discrete version of blazed gratings, and should have the capacity to diffract large amounts of light into overlapping high diffraction orders. The overlapping orders can then be split up by a second periodic grating, perpendicular to the chirped grating, to create the two-dimensional character of the frequency map (see figure 3.19).

Using the fabrication procedure set out in section 3.1, the gratings will consist of gold nanoplasmonic structures on a polymer (SU8) flexible substrate. This flexible substrate can be mounted on top of a fibre in order to diffract the exiting light [47] (see figure 3.11). Using a chirped diffraction grating in combination with a perpendicularly oriented periodic diffraction grating, a 2D light array can be created. Within the array a single colour is mapped onto a single area, creating a one-to-one relationship between location and wavelength enabling the user to produce an image from information sent through a single multimode fibre. Before the specific design of the grating is discussed, a general overview of the relevant theoretical concepts surrounding diffraction gratings will be discussed.

3.2.2 Diffraction gratings

Gratings are an often used to split a collimated lightbeam into diffraction orders. The grating equation illustrates the process for a linear diffraction grating:

$$sin(\theta_m) - sin(\theta_i) = m\frac{\lambda}{d} \tag{3.1}$$

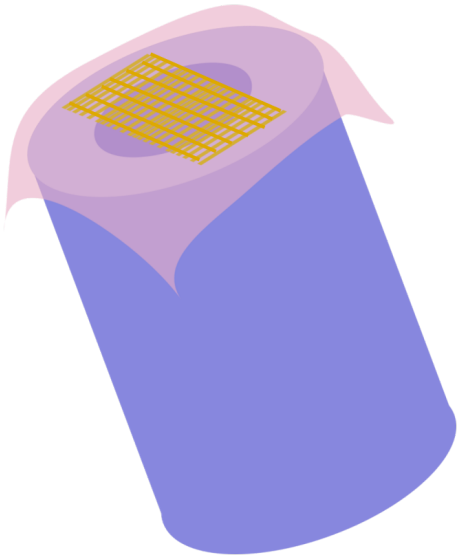

Figure 3.11 – Controlling light exiting a fibre without adding bulky optics is possible by placing nanoscale plasmonic structures to optically manipulate light on flexible substrates and mounting them on a fibre-tip.

Where d is the periodicity of the linear diffraction grating, λ is the wavelength of the light, m is the diffraction order, $sin(\theta_i)$ is the angle of the incident light, and $sin(\theta_m)$ is the angle at which the mth diffraction order exits the grating. From this formula it is obvious that different periods of light result in different diffraction angles, with a smaller periodicity leading to larger diffraction angles. For higher diffraction orders (higher values of m) the difference between the diffraction angle for the shortest (λ_{min}) and longest (λ_{max}) wavelength increases, and consecutive diffraction orders start to overlap as soon as $m\frac{\lambda_{max}}{d} = (m+1)\frac{\lambda_{min}}{d}$. The overlapping of the higher diffraction orders will be of use in the creation of a 2D light array.

Although the grating equation is able to predict the diffraction angles for the orders, it does not include information about the intensity of each order. The intensity distribution is determined by the size and shape of the grating, or if the lightbeam is smaller than the grating, the size and shape of the beam itself. From the Fraunhofer equation it can be determined that the intensity for a simple rectangular linear periodic grating fits a $sinc^2$ distribution, which concentrates a lot of the total energy into the central zeroth diffraction order [142]. It is possible to design different types of gratings to obtain different intensity distribution patterns. One example of particular interest for this project is the blazed grating, also referred to an echelle or echellette grating for large angles, which has a triangular grating profile, instead of the square patterns of a regular periodic diffraction grating, as shown in figure 3.12 [142]. Blazed gratings enable light intensity to be directed to an order different from the zeroth order, while at the same time suppressing intensity maxima at the other orders. The mathematical details of this case are discussed in more detail in section 5.1.2.

The ability to direct a lot of energy into a single order is a desirable characteristic, making blazed gratings an interesting feature to integrate into lithographic fabrication procedures. Unfortunately, the triangular grating patterns necessary to fabricate blazed gratings are not easily made using electron beam lithography, as they require precise greyscale patterning. To overcome this fabrication limitation it would be beneficial to find an alternative design with the same functionality as blazed gratings, able to be fabricated using standard lithographic techniques. Such a solution exists, and

presents itself in the form of chirped gratings, which can be seen as a discrete version of blazed gratings, as both designs are able to linearly vary their induced phase change along the length of a single grating period, or in the case of chirped gratings, superperiod.

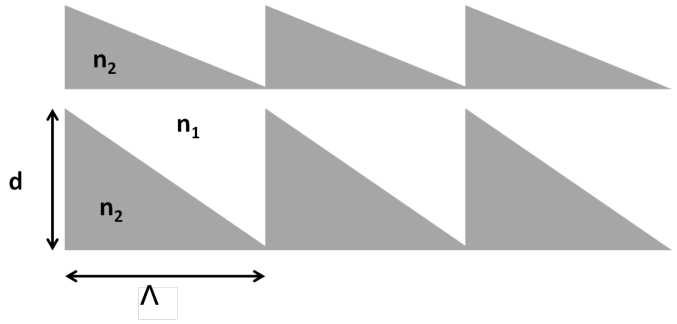

Figure 3.12 – A blazed grating consists of triangular periodic structures of height d and with periodicity Λ. The blazing angle and refractive indices of the medium and grating materials influence the characteristics of the grating.

A more detailed and mathematical analysis of blazed and chirped gratings is provided in sections 5.1.1 and 5.1.2 of the Results chapter, as the analysis was an essential part of understanding the similarities between chirped and blazed grating functionality.

3.2.3 Chirped Grating Design

The functionality of blazed gratings, and the equivalent operation of blazed and chirped gratings is covered in sections 5.1.1 and 5.1.2 above, and should convince the reader of the beneficial use of chirped gratings for creating a 2D light array using nanoscale lithographic structures. This section covers chirped grating design and fabrication in more detail. The chirped gratings studied in this project are gratings for which the width of a single grating period strip varies linearly, starting from a base period d_b and increasing in equal steps to a maximum period d_{max}. Each consecutive strip adds on an extra amount of width, referred to as the chirp c. The result is a set of grating lines each varying slightly in width and distance from each other, forming a single superperiod defined by the base period d_b, the maximum period d_{max}, and the chirp c, as shown in figure 3.13. This structure making up a single superperiod is repeated periodically to form the complete chirped grating. Another important parameter is the fill factor of the grating material relative to the amount of exposed space for each period. Figure 3.13 shows several possibilities, including keeping the grating line width constant, keeping the exposed line width constant, keeping a constant fill factor for each individual period width, etc. The material used also plays a role in the grating behaviour, but during the project the gratings were consistently fabricated with gold.

The momentum change induced by a grating with periodicity Λ is determined by the grating constant $\frac{2\pi}{\Lambda}$ (see figure 3.14). In a chirped grating, the momentum added by the grating changes along a single superperiod structure from $\frac{2\pi}{d_{max}}$ to $\frac{2\pi}{d_b}$. The phase difference induced by the chirped grating is expressed by the difference in these two extreme amounts:

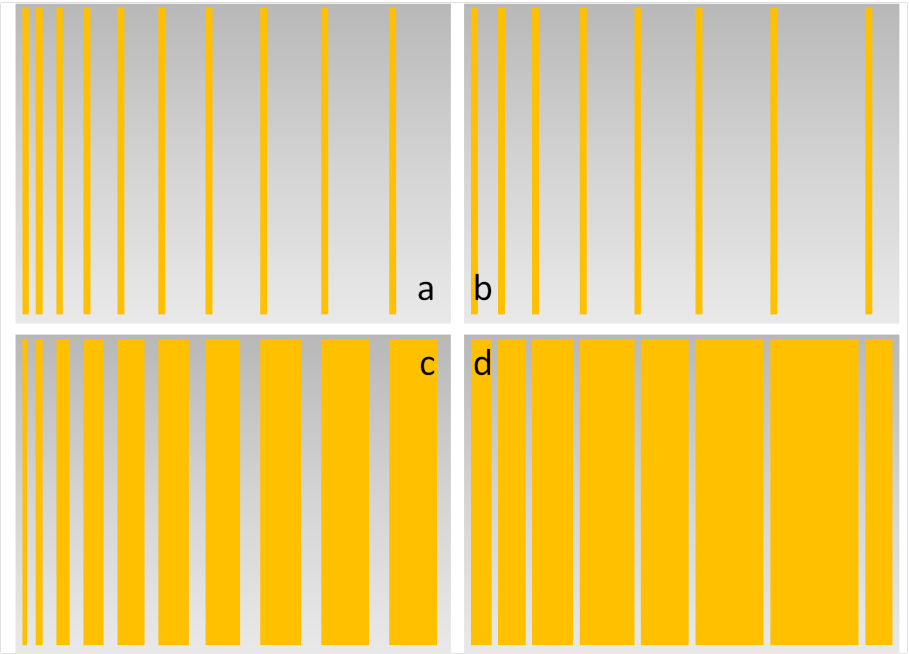

Figure 3.13 – A figure illustrating several design choices which need to be made when designing a grating. (a) And (b) have the same base and maximum period, but different chirp values, with the chirp in b being double of that in (a). (c) Has the same periodicity and chirp values, but different fill factor, filling 50% of each individual period, where (a) keeps the same grating line thickness for every strip of metal. (d) changes the thickness of the metal strips, and keeps the width of the exposed lines constant.

$$\Delta k = \frac{2\pi}{d_b} - \frac{2\pi}{d_{max}} \tag{3.2}$$

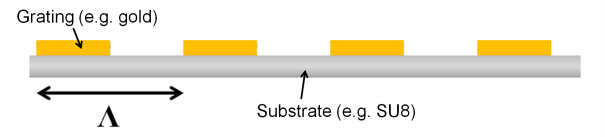

Figure 3.14 – An illustration of a gold on polymer periodic grating with periodicity Λ.

Chirped grating designs require a lot of manual changes as a result of simple parameter changes, changing the chirp or basic periodicity of a grating requires every singe grating strip to be moved. In order to streamline and accelerate the generation of a GDSII [145] file to write a E-Line structure, each chirped grating design was generated using Matlab scripts. Instead of having to manually enter the design features in the GDSII graphic editor, Matlab scripts allow the designs to be generated using a set of parameters. The scripts write documents containing ASCII codes based on instructions in the Raith software reference manual [144], which can be converted by the E-Line software into GDSII files. The Matlab scripts generated grating designs from the following set of parameters: base period, chirp, linewidth (set to 0% for a single pixel line or SPL, the thinnest line the system can write at those alignment settings of the system), superperiod (the width of the total repeating structure), super_repeats (the number of times the superperiod structure is repeated), and height (the length of each grating strip).

3.2.4 Chirped Grating Fabrication

Chirped grating samples were fabricated using the standard lithography fabrication process described in detail in section 3.1, using SU8 polymer [115] membranes on glass (or sometimes silicon) as a substrate for the gold gratings. Most steps in the process were well known and parameter and setting tests were all centered around the electron beam lithography step.

- **Cleaning substrate**
  3 Minutes acetone followed by 3 minutes IPA (ultrasonic bath)
- **Fabricate SU8 membrane**
  Spin Omnicoat [114] 1000rpm followed by 1 minute bake at 230°
  Spin SU8 2000.5 (or SU8 2000.5 : cyclopentanone 1:2) 5000rpm followed by 5 minute bake at 100°
  UV-expose SU8 for 2 minutes followed by 2 minute post-exposure bake at 100°
- **Gold evaporation**
  Deposit 40 nm Au at pressure less than 10^{-5} mbar and deposition rate around $0.1 \frac{nm}{s}$
- **Deposit photomask**
  Spin SU8 2000.5 : cyclopentanone 1:2 5000rpm followed by 5 minute bake at 100°
- **Electron beam lithography patterning**
  Discussed in more detail below
- **Post-exposure sample treatment**
  2 minute Post-exposure bake followed by 45 s in EC, then rinse in IPA
- **Reactive Ion Etch**
  10 - 11 minute etch for 40 nm Au
  19 W setpoint, around -333 DC bias
  500 Ar flow, aim for pressure 5.0 10^{-2} mbar by setting butterfly valve around 37

After a series of dose and setting tests using the Raith E-Line electron beam lithograph, the chirped grating patterns were written using the following set of parameters:

- Aperture: 10 μm
- EHT: 30 kV
- z = 25.5 mm
- Working Distance: approximately 10.5 mm
- current: approximately 0.03 nA
- 1250 x Magnification, 100 μm Write Field
- **Dose and patterning settings**
  basic step size: 0.002 μm
  line dose: 12 $\frac{pC}{cm}$
  line step size: 0.006 μm
  line dwell time: 0.0002 - 0.0003 ms
  area dose: 10 $\frac{\mu C}{cm^2}$
  area step size: 0.01 μm

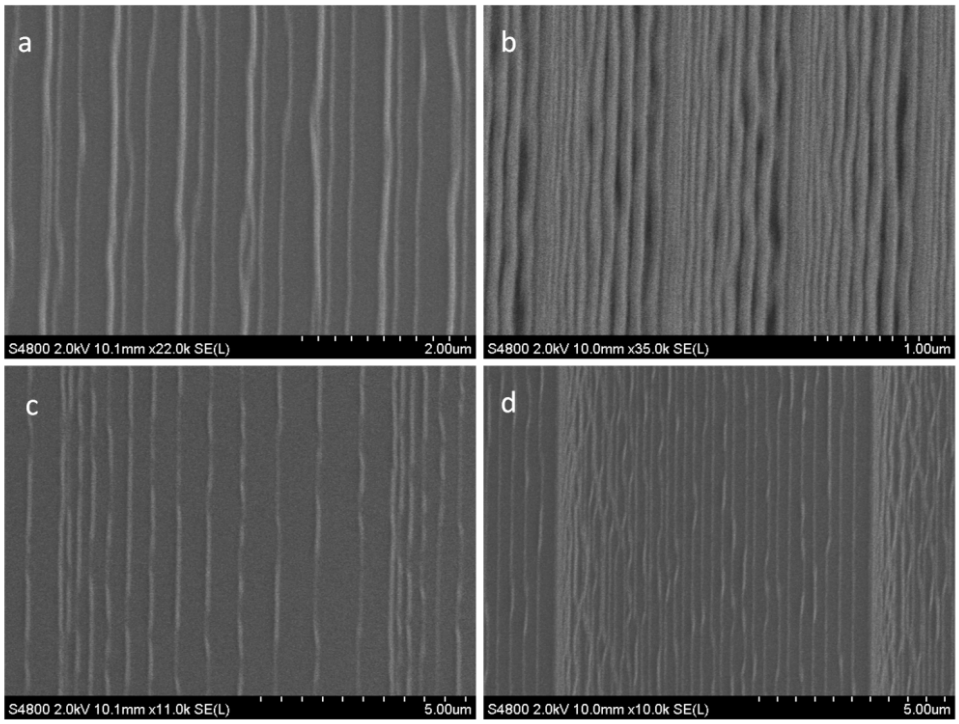

Figure 3.15 – SEM images of chirped grating samples all fabricated on the same sample using the same write settings. The design of the chirped grating influences the dose required to achieve successful patterning. Subfigures (a) and (b) have a low superperiod (800 nm and 1 μm), where (c) and (d) have a high superperiod of 10 μm. The chirp for (a) and (c) is set to 100 nm, and for (b) and (d) it is set to 10 nm.

area dwell time: 0.0003 - 0.0004 ms

dose factor: 2 - 7

The patterning tests were performed to check the limits of achievable line thickness and the required dose to optimise the quality of the written patterns. From figure 3.15 it is clear that the requirements of parameter settings depend on the specific grating design itself. Lower base periodicity and chirp settings mean that neighbouring lines are spaced more closely together, putting constraints on the maximum amount of current the area should be exposed to. If the total amount of current gets too low, the quality of the written patterns reduces and the intended straight and filled in lines become detached and uneven (see figure 3.17 (a)). If, on the other hand, the current is too high, the lines will get overexposed, and expand beyond their intended boundaries, resulting in areas beyond the desired patterns to be crosslinked as well (figure 3.17 (b)). An optimised chirped diffraction grating pattern is shown in figure 3.18.

In order to make sure the design of any chirped grating is executed under optimised writing parameters, it is advisable to always perform a dose test with the desired design pattern, and select the best dose settings for each particular write (as shown in figure 3.16)

3.2.5 Chirped Gratings: Conclusion

This section started with the introduction of the optical requirements of endoscopy applications, and the desire to both scale down the size of optical components and increase resolution of the resulting

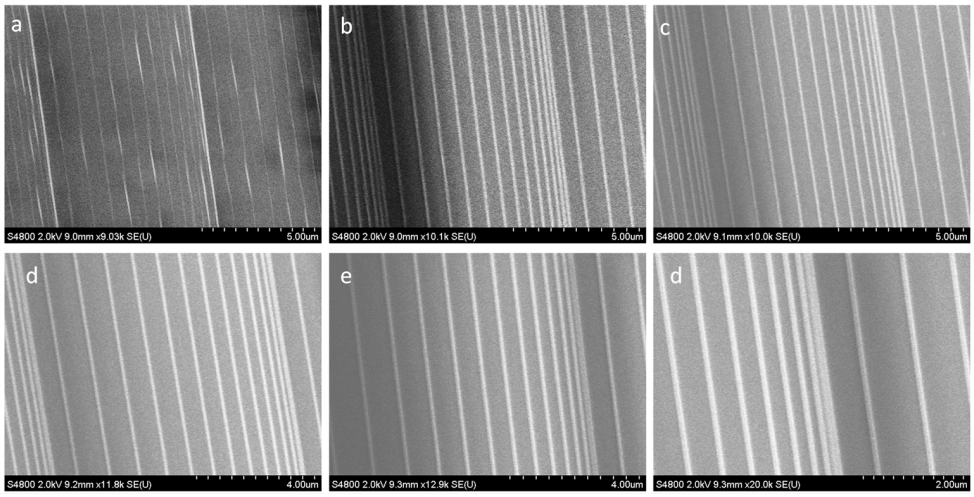

Figure 3.16 – The figure contains SEM images of a dose test performed on a chirped grating design with 7 μm superperiodicity, 100 nm basic period, and 100nm chirp. Images (a) to (f) have been fabricated using a base line dose of 12 $\frac{pC}{cm}$, and a dose factor of 2, 3, 4, 5, 6, and 7, respectively.

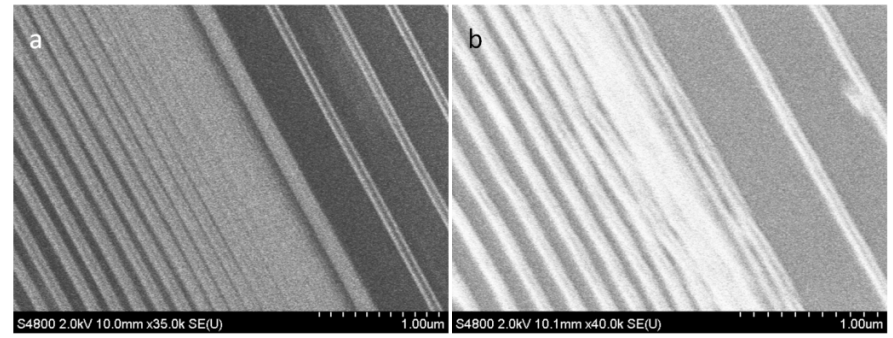

Figure 3.17 – SEM images of chirped gratings fabricated during the same write, and with the same design parameters, but different write settings on the e-beam lithograph. Image (a) shows dose settings which are too high for the design settings, making neighbouring chirped grating strips overlap. In (b) the same design has been produced with a lower dose, which reduces the overlap, but the dose is too low to form a high quality written pattern. The results presented here suggest that the chirp design used here is too fine to be achieved with the used e-beam settings.

images. A potential solution was presented for the challenge of fibres losing spatial elements of the information they collect, suggesting this could be overcome by encoding the spatial information in frequency, as separate frequencies can travel through an optical fibre simultaneously, independently. This created the need of producing a one-to-one frequency to location map, in combination with the requirement of keeping the optical components achieving this feature small and mountable on a fibre.

Chirped gratings were chosen over blazed gratings as they can be fabricated with a step-based depth profile, whereas blazed gratings require greyscale lithography, which is challenging using the standard electron beam lithography process. However, there are many design parameters to be chosen in the chirped grating, and it is not immediately obvious which ones would render the best equivalent of a blazed grating. Based on the analysis of the equivalence presented in 5.1.1 varying the value of $\frac{2\pi}{\Lambda}$ linearly to achieve a linear momentum change is a potentially suitable design choice. Fabrication of the samples followed the standard lithographic process outlined in section 3.1.

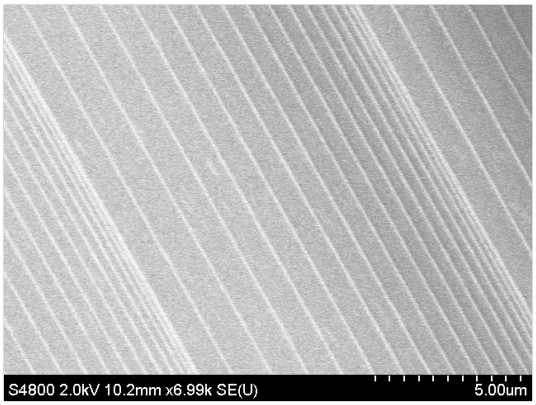

Figure 3.18 – SEM images of a chirped grating design with optimal writing parameters and dose settings.

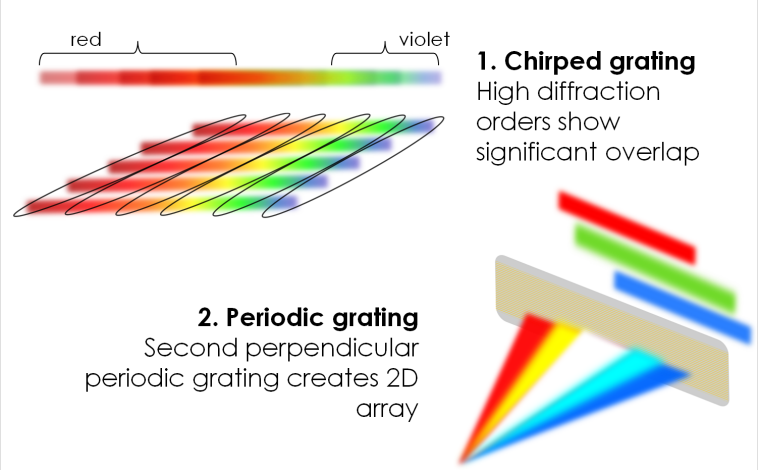

Figure 3.19 – The image shows a schematic of the proposed 2D light array creation. In a first step, a chirped diffraction grating is designed to diffract light to high, overlapping, diffraction orders. A second perpendicular periodic grating then diffracts the light to separate the overlapping colours and create areas covered by a single colour.

3.3 Electron Beam Induced Deposition

Section 3.1 contains a detailed discussion of the methods used to fabricate nanoplasmonic structures using electron beam lithography. As a well-established fabrication technique, EBL is a powerful tool; however, it would be wrong to ignore the limitations associated with the technique. Due to the necessity to use masks, precise alignment of consecutive layers is challenging and in many cases impossible. It is not possible to test or see what you are writing during the lithography step until after the entire writing process is finished and the masks have been chemically treated. This makes testing write settings difficult, and parameter and other dose tests are often performed during a separate write. The technique also has serious limitations when it comes to the creation of 3D structures or greyscale patterning, as illustrated by the example application discussed in section 3.2, where the well-known blazed grating structure is abandoned for a less well understood chirped grating design due to the difficulties electron beam lithography would have creating the greyscale blazed grating profile.

As technology advances, it is logical that people look for ways to get around the shortcomings of existing methods. One innovation has been to adapt an electron beam lithography system to not just

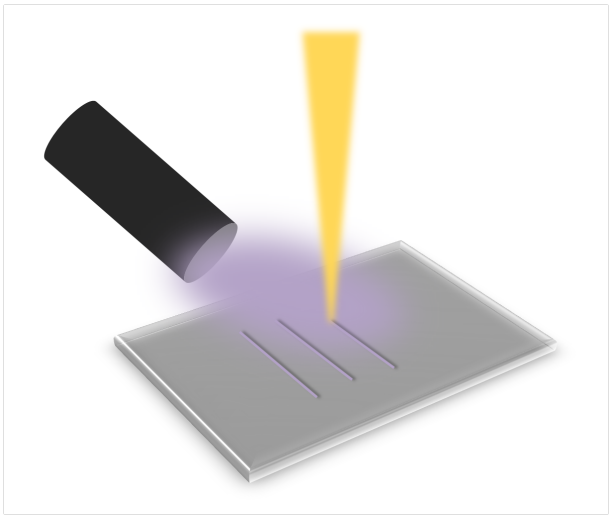

Figure 3.20 – Schematic of the Electron Beam Induced Deposition process. The Gas Injection System nozzle (left) releases gas ($W(CO_6)$ during this project) which releases W to adsorb onto the sample surface under influence of the irradiating electron beam.

pattern available photoresist material, but to deposit materials on the go. The technique is known as Electron Beam Induced Deposition (EBID), a direct-write fabrication process in which an electron beam irradiates localised gas molecules engineered to separate upon irradiation by the electron beam into a target material adsorbed onto the sample surface, and a gas residue to be removed by the vacuum pump [100]. Using an electron beam lithography system enhanced with a gas injection system, this process can be achieved and structures can be directly written onto the sample surface, following the e-beam irradiation pattern. Figure 3.20 shows a schematic overview of a gas injection nozzle locally providing a gas flow to act as the source material for the deposition process. Figure 3.21 shows a detail of Gas Injection System of the Raith e-Line Plus Nanofabrication system, namely the reservoirs storing the gas used during the deposition process on the outside of the sample chamber.

The following paragraphs in this chapter will discuss the use of the Gas Injection System for Electron Beam Induced Deposition in detail. Further chapters will also diccuss the possibilities, benefits, drawbacks, and limitations of the system, and present results obtained using the fabrication methods described below.

3.3.1 Introduction

Next to standard electron beam lithography the Raith e-Line Plus Nanofabrication tool contains a Gas Injection System (GIS) able to directly write patterns onto a sample. Instead of irradiating a photomask layered on top of a material layer and etching back the exposed, unwanted material, GIS is used for a fabrication technique known as Electron-Beam Induced Deposition, where gas locally provides a stream of molecules containing the desired material to be deposited. The electron beam interacts with the molecules to separate the deposit material, which is engineered to adsorb onto the sample surface, and a residue product which is removed by the vacuum pump.

In the following sections the setup, alignment and deposition procedure will be described in detail.

Figure 3.21 – Gas used for the electron beam induced deposition process is kept in reservoirs attached as a separate module to the electron beam system. The lines of the Gas Injection System connect to the reservoirs and preconditioning tools needed to heat up and prepare the gas flow for insertion into the chamber.

Just as with standard electron beam lithography, both the SEM parameters and the patterning generator settings will need to be set. Additional steps are required for the initialisation process of the gas injection system, complicating the procedure, and the patterning recipe setting are different because of the different nature of the materials the electron beam is interacting with.

3.3.2 Introduction to Using the e-Line GIS System

The following subsection describes a detailed step-by-step process to operate the Raith E-Line Gas Injection System, including reasons for their location in the process and examples of what might go wrong and how to fix it. The process is based on the information found in the Raith NanoSuite Software reference manual [144], particularly chapter 21, and own developments and findings for practical implementation. A shorter version of this manual is included as an appendix (see 7.1) to this thesis.

Although the operation of the GIS system is disclosed in the Software reference manual[144], a detailed, practical description of the process, including indications of where the standard procedure might result in errors and what can be done about it, had to be developed through using and gaining experience with the system. The operation of the GIS system is not intuitive, and includes many individually essential steps. Mistakes could result in inflicting a considerable amount of damage to a sample, the machine equipment, or both. The procedure described below is not the only correct operating method, nor is it necessarily the best, but if the instructions below are followed meticulously,

the system should operate successfully.

Learning to initialise, align, and operate the GIS system and bringing down the amount of time needed to go throught the process, with only the user manual as guidance was not straightforward, and required a great amount of care to make sure no mistakes were made. During the learning process of developing an operating procedure, which resulted in the creation of this manual, the time necessary to set up the system for performing a GIS deposition was reduced from 3.5 hours to around 45 minutes. The existence of this manual will hopefully contribute to making the operation of the GIS system more streamlined and tailored to the specific machine available to the university, with the step-by-step description of the process giving an inexperienced user confidence while going through its essential steps.

3.3.3 Initialisation and Alignment

1. **Start the Elphy program as a GIS/Nanomanipulator User**
   Operating the GIS will not work when trying to act as a standard user, and as an admin user, it is possible to override systems in place to avoid damage to the machine.

2. **Load the sample on the Ultra-Flat stage**
   The use of this stage is essential, in order to avoid collisions of the GIS and/or nanomanipulator systems with the stage. The GIS system assumes this stage layout is being used when navigating the GIS nozzles around the machine chamber.

3. **Make sure the GIS nozzles AND the nanomanipulators are initialised and parked**
   Initialised and parked items are identified by a blue circular icon next to their name in the relevant submenu. If the circular icons are red or grey, the operator in question is not parked and/or initialised, and this will need to be remedied in order for the setup process to continue. If the operators are not initialised, the park button will be grey instead of blue, and it will not be possible to click it.

   Although the nanomanipulators are not needed during GIS operation, the system needs to know their location in order to know if the space is clear for a movement to be performed, avoidoing possible collisions with the nanomanipulators and inflict damage.

   1) In order to start the initialisation process, click a button icon at the top left of the GIS operating menu, indicated by a ruler with the numbers [0 1 2] beneath it. This button can start the initialisation process, but often will not start itself. In that case it is necessary to drive the stage down to z = 1 mm manually, and try the initialision procedure again. It might be necessary to log in as administrator to do this.

   2) If driving down to z = 1 mm fails to start the initialisation process, log in as administrator and check whether the nanomanipulators or GIS nozzles are locked, and if so unlock them,

which can be done in the Administrator level submenu by deselecting a lock-icon.

All operators need to be unlocked and parked, and the system is returned to being logged in as a GIS/nanomanipulator user before proceeding to the next step in the setup process.

4. **Once everything is initialised, turn on the relevant nozzle and reservoir heaters**
   Heating the nozzles requires time and it is beneficial to allow this to happen during other alignment and initialisation steps. Although the first heating up cycle of the nozzles happens relavively fast (less than half an hour for tungsten), subsequent cycles of cooling down and heating up of the nozzles are significantly slower. Whenever a user level needs to be switched (e.g. from GIS/nanomanipulator to administrator level or back), the heaters are turned off, and their slow recalibration of the heating process causes delays to the process. It is therefore helpful that you check the nanomanipulator and GIS initialisation state before starting the heating up process, in order to avoid losing time unnecessarily.

5. **Select write settings for aperture, EHT voltage, and working distance (WD)**
   The meaning of the settings is discussed in more detail in section 3.3.5. The system is able to save several presets, which can be useful starting points when using similar samples several times. If a similar sample has previously been loaded and used for GIS operation a relevant preset might be loaded.

6. **Drive the stage to z = 25.5 mm**
   This is a standardised starting point for any write to obtain an approximate working distance of 10 mm, and very suitable to start the precise z-alignment procedure later in the process.

7. **Measure the Faraday Cup current**
   This can be done both manually and via the automated built-in system of the software. When using the automated system, be sure to check that the Faraday current is measured at the correct location, above the Faraday cup on the stage. If the wrong location is selected, which occurred several times during testing, the measured current will be incorrect and the system zill not flag this up. If the USB TV monitor is turned on during the Faraday cup measurement the current will not be measured and retun a value of 0. The system will not give an error message when this occurs, or provide a warning if the returned value is 0, so care should be taken by the user to avoid this situation.

8. **Adjust the basic alignment settings: origin, angle correction, focus, aperture, and stigmation**
   These are all alignment procedure steps which also occur in the standard use of the E-Line in lithographic operation, and will therefore not be discussed in detail in this section. Origin and angle correction procedures are traditionally performed at the beginning of the alignment procedure, as they require large ranges of movements in the x and y directions, and do not need precise alignment on the sample surface, which might be location-dependent. These procedures cannot be performed once the nozzles have been driven in, because of the movement they require. In order to start the precise z-alignment procedure, the system should be sharply

focussed on the sample surface.

9. **Set the Working Distance to exactly 10.000 mm**
   During Electron-beam induced deposition, the nozzles of the gas injection system need to be very close to the surface of the sample, and the GIS equipment is calibrated to operate at a 10 μm working distance. When driving the nozzles down to hand 10 μm above the sample surface, the location of this surface should be known to at least 1 μm precision. The micronscale alignment of a stage able to move within a range of 30 cm is not straightforward, and requires reliable and precise equipment. The observant user will also note that the sample itself should not show any variations in height above micron scale as these would form obstacles for the nozzles to collide with.

10. **Peform an iterative Working Distance setting process**
    (recommended start at z = 25.5 mm at or near a location where you intend to write)
    1) Focus on the sample surface
    2) Read the Working Distance. This can be done from the 'read W' menu tab. Once you have read the WD value, click 'adjust W', making sure the 'read from CCD' option is not selected.
    3) Drive to W = 10.000 mm and refocus on the sample surface.
    Repeat this process until the sample until the read W value stabilises at 10.000 mm. In order to set the value to a reliable value with micrometre scale precision and accuracy, a 0.5 μm erorr is tolerated, rounding up or down to the nearest μm. The software does not have the option to set the working distance directly, as it depends on both the z-location of the stage, and the focussing settings. it is instead set indirectly by reading its value to W, which is a relative z-parameter, and can be used to direct the z-value. By equating W and the working distance iteratively, and refocussing after every iteration, the z-location of the stage and focussing parameters are coordinated to result in the correct 10.000 mm working distance.

Once the alignment parameters and working distance are set to the desired values, save these settings in a first preset mode, e.g. 'EBID parked'. This will allow the user to reset the system to this set of parameter values if the system gets misaligned too severely or the working distance is adjusted unintentionally. Mistakes during the setup and writing process are easily made and this preset avoids you having to restart the alignment procedure when an alignment mistake is made in a later point of the process.

11. **Start the outgas procedure**
    During the time it takes to align and focus the system at the correct working distance, the reservoir and nozzle heaters should reach the desired temperature to start the outgassing procedure. The circular LED icon next to the control button of a gas nozzle on the GIS submenu will turn green to indicate that the nozzle has heated up sufficiently and is ready for the gas flow to be opened.(see figure 3.22).

Outgassing should be performed at the start and end of each use of the GIS module, to remove any residue from the nozzle and gas flow system to avoid damage to the equipment or decrease the quality of the deposition. In order for the outgas procedure to start, the EHT needs to be turned off, for the pressure gauge in the sample chamber to function so it can monitor the condition inside the chamber during the outgassing procedure.

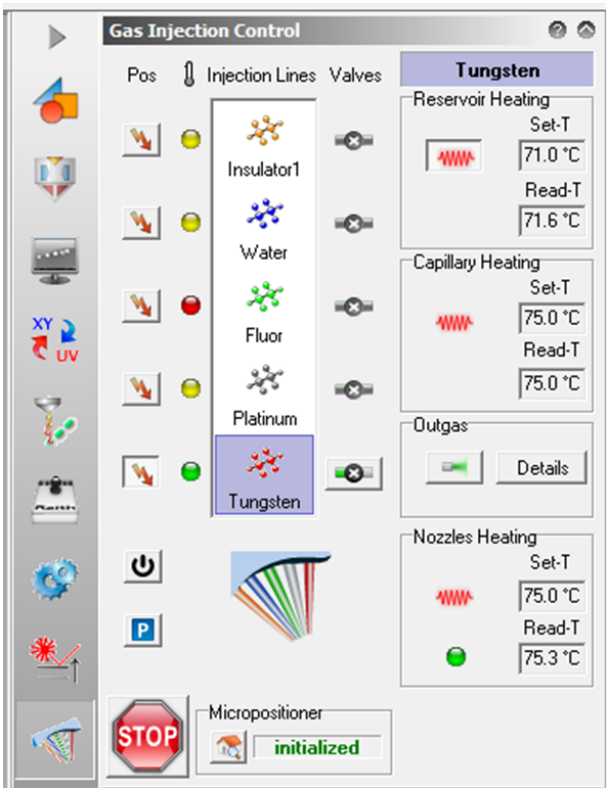

Figure 3.22 – Menu screen capture of the Raith Nanosuite software, GIS nozzle operation submenu. The GIS micropositioner has been initialised and the GIS nozzles are parked. Nozzle 5 (Tungsten) has been selected as the writing nozzle, and the nozzles and Tungsten reservoir have reached their set temperature, indicated by the green LED icon. The tungsten line is ready for outgassing and gas flow procedures.

During the outgassing procedure, the system vacuum is monitored using the Gun Monitor program. The system vacuum should stay below 1 e^{-5} mbar at all times and ideally stabilise around 3 e^{-6} mbar when the GIS valves are closed.

Outgassing is done using the standard system settings and using outgas 'on' times of 0.3 s, 0.5 s, and 0.7 s. Each time setting is repeated until the spikes in pressure stabilise or reduce in height.

12. **Drive the nozzles in**

    Once the outgassing procedure has finished the nozzles can be driven to the surface of the sample. This procedure can be followed from the USB TV screen setting, and there is an emergency stop button availiable in the GIS setting menu.

13. **Setting up the EBID writing mode**

    The proximity of the nozzles to the surface and in the field of view of the electron beam column affects the alignment and focussing settings of the system. The aperture, stigmation and focussing settings will have to be adjusted, in a similar method as described above, to fit the new situation. These new settings can be saved in a separate preset, e.g. EBID write. If this preset already exists from a previous write on a similar sample, loading it once the nozzles have been driven to the surface can simplify the realignment process.

3.3.4 Setting up writing patterns using the GIS

This section gives an overview of how to use the GIS software to write structures, focussing on 2 different approaches: ad hoc writing and writing using positionlists, and both come with their own benefits and drawbacks. Ad hoc writing is useful for tests on the sample, due to its setup speed, and when precise positioning on the sample is required, as it employs a fast drag-and-drop method to position designs instead of using coordinates to position the structures. Positionlists are useful when the positioning of structures relative to each other is more important than their precise location on the sample. The positionlists take longer to set up, but are saved and can therefore more easily be repeated. They also lend themselves well to larger and regular sets of repeated structures and patterns.

1. **Writing Ad Hoc**
   Writing ad hoc structures allows the user to use the equipment in its true point-and-shoot operating modus, selecting and focussing on the location on the sample where you wish to write, and drag-and-dropping the desired patterns to their precise location. The patterning parameters can be individually set for each structure, and it is not necessary to save the patterning parameters or location of individual structures relative to each other.

   Using the imaging mode the user can drive to a desired location on the sample and focus there. Once the desired settings have been reached, the user can open a single image, which will switch the system to patterning mode. The image will show the field of view of the current location of the electron beam, and at the field of view settings selected during setup of the system.

   A structure design file of a compatible format (in this case GDSII files [145] were used), can be placed onto the image by drag-and-dropping the GDSII-file into the image. This action will also open the drawing tools section of the toolbox. Using the drawing tools, the user can then change the originally dragged design by altering, deleting, or adding structures to the design, and moving the structures around both relative to each other and as a whole across the sample surface. These changes can be saved in the GDSII file or the original GDSII file can be kept.

   Next to the design of the writing pattern and its position, the writing parameters need to be set, an overview of these parameters is provided in table 5.1 in the Results chapter. This can be achieved by selecting one or more of the structures and pressing A to bring up the window to set and select patterning attributes, or by dragging and dropping a pre-written set of attributes (recipe settings) to the selected structures. Whether using a pre-written recipe or setting the patterning attributes from scratch, it is important to update the beam current values in each recipe. The beam current should have been determined during the initialisation and alignment phase of the writing process, so it is important to click the adjust button, and not the button with the icon of a pipette, as this will drive back to the Faraday cup, which could damage the system, as the nozzles are driven near the sample surface.

2. **Writing with Positionlists**

   Writing with positionlists makes it easier to save writing patterns for repeat use, to have several structures at precise positions relative to each other, and to automate the writing process. It

does lose the point-and-shoot functionality of the system, as the structures are positioned using coordinates instead of being positioned directly onto an image of the sample surface. Macros make it possible to automate actions necessary for the operation of the system, e.g. driving the nozzles in/out, opening/closing the valves, and changing the working distance for 3D write settings. Positionlists require a seperate GDSII file [145] for each structure with a different design or set of patterning attributes, although dose factors of GDSII files in their entirety can be amended in the positionlist itself.

A positionlist is a list of files which are executed in order, and can be compiled by drag-and-dropping the relevant files into the list. The list should include a file of each structure to be written, with location coordinates allocated to each file, as well as any macros and functions to automate changing settings of the system during the write. Each GDSII file should have the patterning attributes set individually, which can be achieved by opening the file in editing mode, selecting one or more structures in the file, and pressing 'A' to open the patterning attributes menu and entering the desired parameter values (see section 5.2.1).

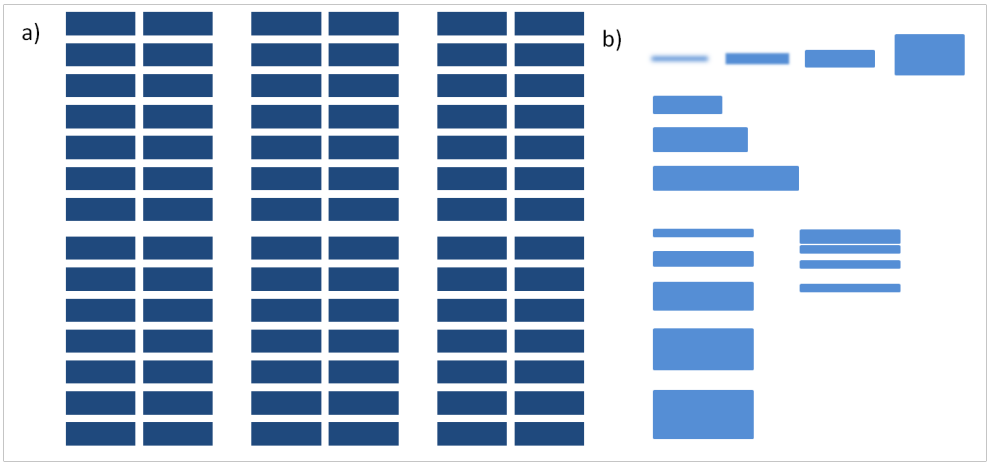

Figure 3.23 – a) Writing with positionlists is useful for writing patterns with multiple structures at precise positions relative to each other, as structures are positioned based on coordinates. b) Ad hoc writing uses the point-and-shoot method and is therefore useful to perform dose and other parameter tests to optimise the write settings for each individual sample. Characteristics to be tested could include parameters which influence the writing dose and speed, minimal feature size, and feature separation.

3.3.5 Setting recipe values

The GIS system allows the user to define individual writing parameters for each structure, making it possible to have different settings even within the same GDSII file. Some settings can be defined for the entire write, as is the case for normal E-Line operation, (e.g. step size, dwell time, ...) but other parameter values specific to the GIS deposition process need to be set for each feature.

Some of the system settings affect the writing parameters of the system. The aperture and EHT voltage settings both have an influence of the writing speed and resolution of the system. Deposition rates increase for lower EHT voltages [144], and decreasing the aperture increases the depth of focus and decreases the beam current.

Parameter values for each individual structure can be set and edited using the patterning attributes

menu within the GDSII file editing mode. This menu can also be called forward during ad hoc writing. The menu opens in a separate window, and contains a list of patterning parameters, an overview of which can be found on pages 215 - 219 of the *Raith E-Line Software Reference Manual* [144]. In the list of parameters, a whole range of values need to be selected, both general e.g. the process type (deposition), and deposition specific elements. The parameters are organised according to the type of structure (dots, lines, areas).

One of the general parameters is the value of the Faraday cup current (measured during setup), which is essential to allow the system to determine other writing parameter values. Saved recipes tend to remember the previously loaded value, and do not update the current automatically, even though a new value has been measured during setup of the GIS process. The value can be updated by clicking 'adjust', and not the button with a pipette icon, as this button drives the stage to align the Faraday cup underneath the electron beam column to remeasure the current, which could damage the system when the nozzles are at the sample surface. *The system does not provide a warning message if you press this button so care must be taken by the user to not press it when the nozzles are driven in.*

When it comes to setting the parameters relevant to the material deposition, a key value to determine is the dose, the amount of charge deposited in a location. Depending on whether dots, lines, or areas are written it is expressed in charge (in the system often expressed in units of pC), charge per length (pC/cm), or charge per area ($\mu C/cm^2$) respectively. The dose can be calculated as the product of the dwell time with the beam current, divided by the relevant step size, and the selected number of loops, and line spacing also play a role in the overall total exposure of electron current to the sample surface [144]. The balance between the different parameters determining the dose, as well as the dose itself, is delicate and depends on the nature of the sample, as well as the overall settings of the system (e.g aperture size, EHT value, etc.). Decreasing the step size increases the dose as does increasing the dwell time of the beam in a specific location. Smaller step sizes and line spacing increase the resolution as well as the dose, although making them too small will cause overlap of neighbouring elements which can affect the pattern. If the dose is too high, the deposition will not adhere to the surface properly, and if the dwell time too short, the deposition might fail. In order to find a balance between the settings, the ad hoc writing procedure of the GIS system provides an ideal method to test different parameter values. Making use of different loops makes it possible to repeat the singular dose settings several times, and the dose can also be influenced by changing the dose factor, which multiplies the value of the base dose.

Chapter 4

Experimental Setups

The following chapter provides a description of the design and use of the experimental setup built during this project, and outlines how it works and was used to measure the properties and characteristics of different types of samples fabricated. The content of this chapter is limited to setups meant to characterise and measure samples, and any setups built for use during fabrication were covered in chapter 3 above, and will not be discussed here.

4.1 Fourier Microscopy

4.1.1 Introduction

The following section concerns the Fourier setup which was built to measure far field diffraction and scattering patterns of several types of samples. The sections will discuss what Fourier Microscopy is and why it was chosen for the project. The development of the Fuorier Microscope in its different stages will be outlined, discussing the purpose of the individual optical elements, aiming to clarify why they were added to the setup.

4.1.2 Visualising the Far Field with Fourier Microscopy

When studying diffraction and scattering behavior, the properties containing the most characterising information is the distribution of the directions in which light is scattered or diffracted, and the intensity distribution across these directions. In order to visualise these properties, it is necessary to observe the light pattern at a point where all the diffracted rays have been separated into their respective directions. In the near field, diffraction orders are still overlapping and cannot be distinguished from each other, whereas in the far field light moving in different directions have propagated far enough to have moved away from each. In fact, the far field is the Fourier transform of the spatial light distribution, rendering a pattern of the spatial frequencies of the initial beam or beams, making it an ideal tool to observe diffraction patterns [147] [151]. Of course, measuring or observing light in the far field has its own drawbacks, with long propagation distances requiring a large amount of space, and the physically separated diffraction orders requiring a large sensing surface covering a wide range of angles at the point where they are observed. Luckily, there is a solution to any problems this may cause as it is well known that a thin lens brings the far field of a light distribution in its

object focal plane, to the image focal plane of that lens [148], meaning it is possible to control the location where the far field light distribution is observed, as well as the size of the far field pattern and the space required for the optical setup.

Fourier imaging can be explained, using the geometric or ray optics model, as imaging all rays having the same direction when hitting a lens onto a single point in the image focal plane, also referred to as the Fourier plane. This means that a point in this plane represents a direction, or spatial frequency, and therefore a direction in real space has been converted into a point in Fourier space. Looking at Fourier imaging starting from an image formed in the object focal plane of a lens, all rays coming from a single point in this image will travel parallel to each other after passing through the lens, as illustrated in figure 4.1 showing that the reverse transformation has been performed and a location or point in object space has been converted into a direction or spatial frequency in image space.

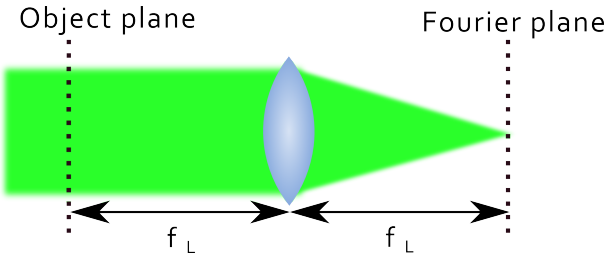

Figure 4.1 – A thin lens transforms all light coming from a single direction in the object focal plane, into light being focussed in a single point in the image focal plane, also called Fourier plane, behind the lens. Collimated light travelling parallel to the optical axis will be focussed onto the intersection of the optical axis with the Fourier plane. A thin lens can (Fourier) transformed each direction to a single unique point in the focal plane.

This ability to convert images in real space to a direction in spatial frequency space and back using a set of 2 lenses is equivalent to using a Fourier and inverse Fourier transform to arrive back at the original function in real space. This feature allows us to create two sets of conjugate focal planes using a set of lenses, each placed to have the object focal plane to coincide with the image focal plane of the previous lens in the light path, each consecutive plane alternating between rendering real and spatial frequency images of the same original object. The planes where a real image is formed are also referred to as image planes, whereas planes which produce a spatial Fourier transform of the original object are referred to as back focal planes. An example illustration of the use of two sets of conjugate planes is Köhler illumination, which uses a back focal plane image of a filament to illuminate a sample as this provides uniform illumination due to light from the filament having no preferred direction [149] [150].

4.1.3 Fourier Setup

Building a Fourier setup might appear straightforward at first glance, as the above paragraphs have just discussed that a simple thin lens provides a Fourier transform of the object focal plane, in the image focal plane. However, although this is the case, the characteristics of the optical tools used have an influence on the quality of the Fourier image formed, and often a simple lens will not suffice to achieve a Fourier transform with acceptable properties.

One of the first optical properties to consider is the Numerical Aperture (NA) of the lens, which for a thin lens in air can be expressed as follows:

$$NA = nsin(\theta) \tag{4.1}$$

With n equal to the refractive index of the lens and θ equal to the half angle of the field of view angle between the centre of the focal plane and the diameter of the lens, as shown in figure 4.2. The numerical aperture of a lens expresses the viewing angle of the lens, and as the goal of the setup is to map the directions in which light propagates from a chosen sample, it is desirable to maximise this angle, and corresponding NA.

Figure 4.2 depicts a schematic of the viewing angle for a thin lens and an objective, a more complicated optical lens system often designed to minimise aberrations. The best type of objective for Fourier microscopy is a Plan Apo objective with high NA and low magnification. The plan and apo(chromatic) terms indicate optimal correction of field curvature, and chromatic and spherical aberration, respectively. The need for a high NA is explained above, and a low image magnification results in a larger image in the Fourier plane (as illustrated in figure 4.3). Usually, the numerical aperture of a lens increases with magnification of the lens, so a compromise between Fourier image size and viewing angle will need to be made when selecting an objective [151]. In the setup a Mitutoyo Plan Apo 50x objective with an NA of 0.55 was used for the majority of the measurements, with occasional tests performed with a Mitutoyo Plan Apo 100x objective with an NA of 0.7.

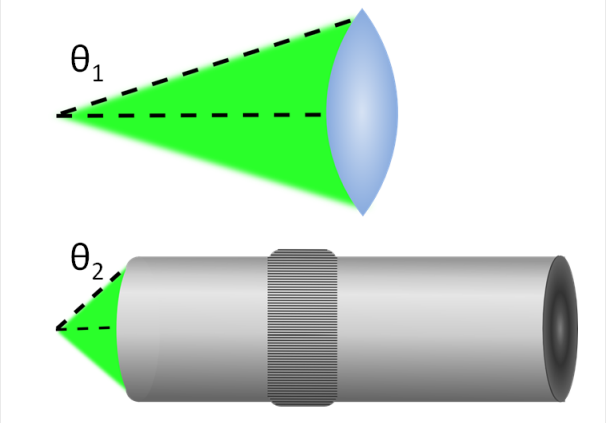

Figure 4.2 – The numerical aperture of the lens determines which viewing angle can be observed by the Fourier microscopy setup. Objectives with large magnification can be designed to have a large numerical aperture θ_2 compared to the relatively smaller NA of a single lens θ_1, equal to the product of the refractive index of the lens and half the diameter of the lens aperture divided by the focal length.

Now that the lens to be used for Fourier transforming the light pattern has been selected, it should be straightforward to get the Fourier transform by simply placing the illuminated sample generating the diffraction pattern in the focal plane in front of the objective, and placing the detector in the back focal plane. Figure 4.3, which contains the Fourier image of a periodic diffraction grating at two different objective magnifications, illustrates the clear equivalent between the back focal plane image, the far-field pattern, and a Fourier transform. The Fourier transform of a a collimated beam diffracted by a periodic grating is a series of points along a straight line in the plane of the periodic

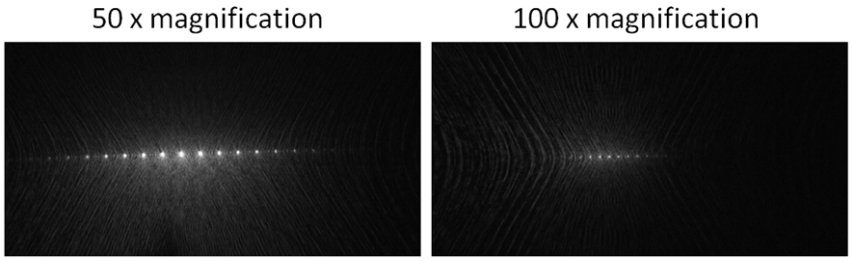

Figure 4.3 – Comparison of images taken with the same setup and 16 μm periodic grating sample, but using different objectives. The lefthand image shows the Fourier image at the back focal plane for a 50 x magnification, and the righthand image shows the same for a 100 x magnification objective, illustrating that a higher magnification, linked to the same numerical aperture, results in a smaller Fourier image.

grating profile. As a periodic diffraction grating produces light diffracted into orders distributed as dictated by the grating equation 3.1, a set of discrete diffraction directions is expected in the far field 3.2.2, which corresponds with the obtained image, each dot on the Fourier image representing one of these diffraction orders, and equivalent propagation directions. The far-field pattern has been brought forward to the back focal plane of the lens, and displays each direction in which a significant amount of light is diffracted within the field of view of the objective, and each dot can be understood to be a spatial frequency of the Fourier transform of the diffraction pattern.

However, it is common in many objective designs for the back focal plane to fall inside the objective casing, making it inaccessible for the detector. Additional optical elements will therefore be required in order to direct the back focal plane image onto a detector.

In a first version of the Fourier setup, two additional lenses, referred to as a tube lens and a Bertrand lens are placed to overlap consecutive image and object focal planes, as shown in figure 4.4. The tube lens is placed after the objective, with the back focal plane overlapping with the focal plane of the tube lens, to create an image of the original object at the imaging focal plane of the tube lens. The Bertrand lens is then inserted to take a Fourier transform of the image of the original object by aligning the focal plane of the Betrand lens with the location of the image plane. The Fourier transform can be found at the back focal plane of the Betrand lens, where the detector (Basler Ace 1920-25gm) can be placed [151]. Aligning a microscopy setup to image the back focal plane can be very counterintuitive as the image of the observed object is not in focus, making the build and alignment of the setup a lengthy process. Figure 4.4 illustrates the 2 sets of conjugate planes, the image plane and the back focal plane, alternating at the focal plane of each consecutive lens [150].

The quality of the observed image is influenced by the precision and accuracy of the alignment of the setup. Figure 4.5 illustrates how the distance between the sample and the objective can influence the observed pattern. In the images the working distance, which the distance between the sample and the entrance of the objective is often referred to, is varied from 6 mm to 24 mm. The detected pattern clearly shows a maximum field of view angle, which appears to be achieved when the sample is placed at the focal plane of the objective, located at 20 mm. The objective has been designed so that this distance with widest viewing angle coincides with the point where rays coming from optical axis are collimated and parallel to the optical axis at the back focal plane. This distance can therefore be

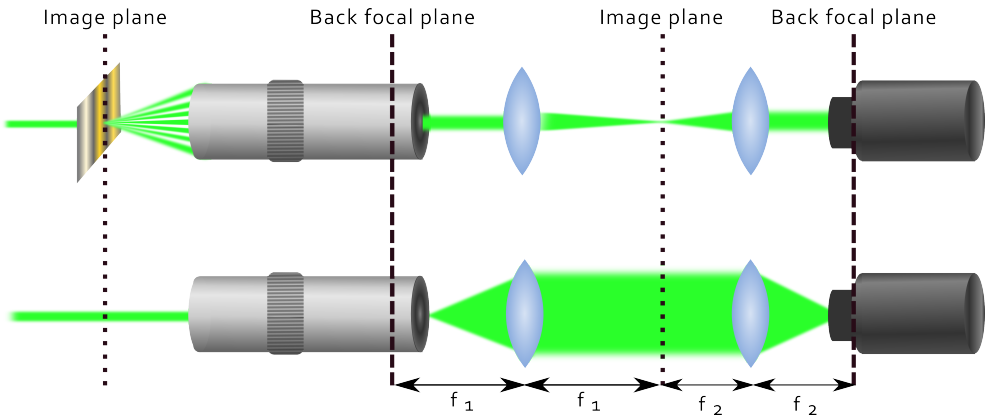

Figure 4.4 – A schematic of the Fourier setup using 2 lenses, indicating the locations of the imaging and back focal planes and the distance between lenses and planes. The top schematic shows the image-forming rays, being in focus when at image plane locations and parallel when passing through the back focal planes. The bottom schematic shows the Fourier image-forming rays, which are in focus at the back focal plane of the objective, and on the detector.

referred to as the front focal length of the objective. For distances larger than this optimal distance, the outer parts of the light cone are no longer caught by the objective, cutting off those propagation directions, represented as the outer spatial frequencies of the Fourier image. If the working distance is shorter than the optimal length, part of the beam will be blocked inside the objective itself, resulting in the lower number of diffraction order visible in lefthand images in figure 4.5.

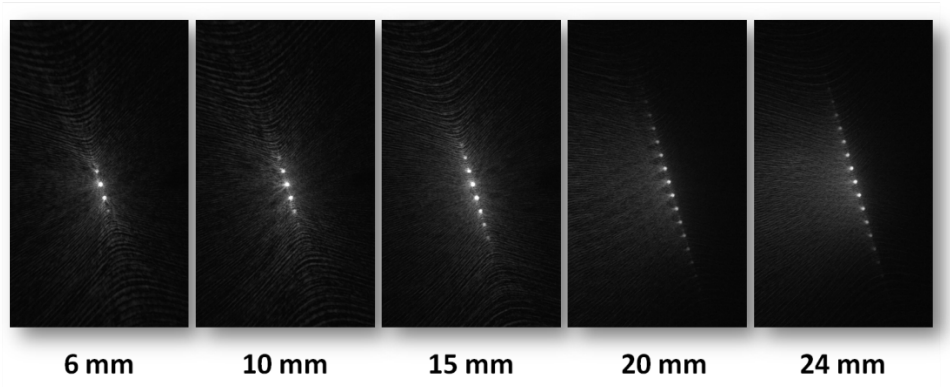

Figure 4.5 – The figure shows a series of Forier images taken with the same 2-lens setup, using a 16 μm periodic dielectric diffraction grating and 50 x magnification objective. From left to right the working distance between the sample and the entrance of the objective was varied from 6 mm, 10 mm, 15 mm, 20 mm, and 24 mm. 21 mm was determined to be the ideal working distance for the objective.

Although the above setup is suitable for measuring high-efficiency periodic gratings, distributing a significant amount of energy to higher orders, as illustrated in figure 4.3, other gratings will have a less even energy distribution, with the zeroth order intensity dominating the diffraction pattern, as shown in figure 4.6. This imbalance in intensity makes it impossible to set an exposure time on the detector to observe the higher orders, either the exposure time is too high and the intensity of the zeroth order saturates the sensor and screen and drowns out the other orders, or the exposure time is lowered to avoid this zeroth order saturation, but the intensity of the higher orders is not observable at these settings.

In order to make it possible to observe higher diffraction orders of samples with a single dominant

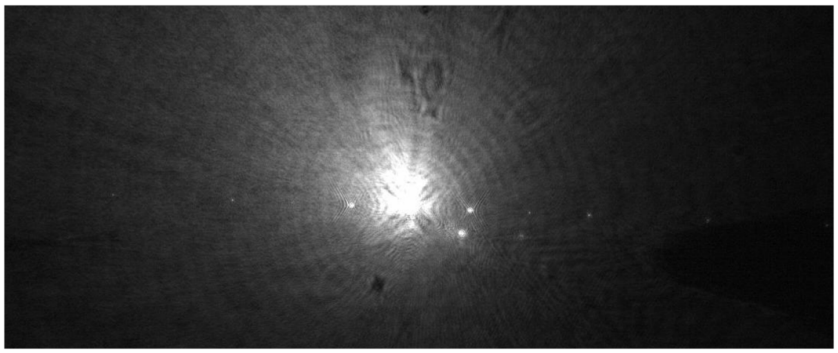

Figure 4.6 – The intensity distribution of samples with lower efficiency is biased towards the zeroth order for perpendicular incidence, as most of the incident light is led towards the zeroth order. The image shows the Fourier transform of the diffraction pattern of a 10 μm periodic gold on glass grating.

order using the Fourier setup, a beam block can be placed in the back focal plane, at the location where all light diffracted into the zeroth order is focussed. In the setup described above (figure 4.4), two back focal planes are present, the first is located within the casing of the objective, and therefore unreachable. The second is focussed onto the detector, and also unsuitable to be used to block the dominant light order. To achieve the beam block, the Fourier setup will have to be expanded to include a third back focal plane, which should be accessible to a beam block element.

An additional lens is placed behind the Bertrand lens, located 2 focal lengths away from the back focal plane where the detector was placed before. This frees up the second back focal plane for placement of a beam block. The third lens simply provides a one-to-one upside down image of the back focal plane at a distance of twice the focal length on either side of the lens. The detector can be placed two focal lengths away from the lens to image this third repetition of the back focal plane, as shown in figure 4.7. The beam block is set up to be translatable across the back focal plane in order to align it with the desired order to be blocked.

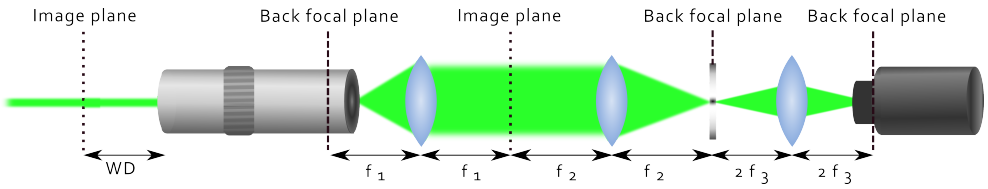

Figure 4.7 – The Fourier microscope setup extended with a third lens, and a movable beam block is added to enable the suppression of a dominant diffraction order. The third lens is placed at twice its focal length from both the detector and the second back focal plane to create a one-to-one translation of the back focal plane.

Figure 4.8 shows a comparison of the image recorded by the detector with and without a beam block blocking the zeroth diffraction order. The top image (a) shows the recorded image when the beam block is not in place: the zeroth order is bright and clearly visible in the centre of the image. The bottom image (b) shows a recorded image taken with the same setup and sample, but with a beam block in place in the back focal plane, preventing the zeroth order from propagating. In order to detect the lower intensity of the higher diffraction orders visible in the image, the exposure time of the image in (b) needs to be higher than the exposure time used to obtain an image of the brighter illumination of (a). The grey background patterns in (b) are due to the imperfect shape, size and positioning of the beam block. The block used in the setup was a small black dot drawn on a glass

slide in permanent marker, causing diffraction around its irregular edges. The grey and black marks in (a) are caused by imperfections and damage (e.g. scratches) to the optical components of the system.

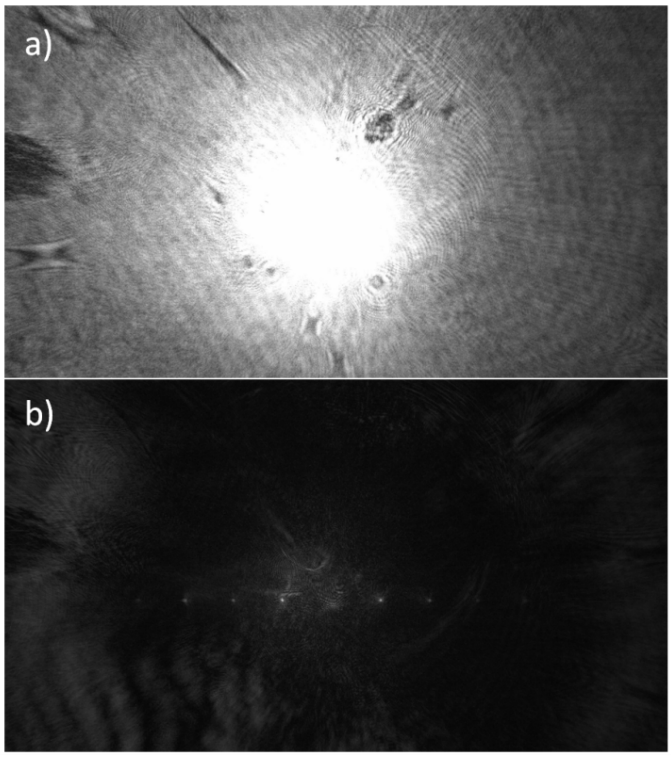

Figure 4.8 – a) Fourier image of a gold periodic grating, with the zeroth diffraction order saturating the detector, and no other diffraction orders visible. b) The same sample and setup, but with a beam block in place in the back focal plane, blocking the zeroth order transmission, making the higher diffraction order visible.

The setup as it has been described up to this point relies on perpendicular illumination transmitted through the back of the sample. Indeed, when keeping in mind one of the intended applications (see 3.2), the necessity to place the diffraction pattern generating sample at the end of a fibre tip makes perpendicular incidence a requirement to correspond with application conditions. The fabrication procedure of chirped grating samples, and many other types of samples used throughout the project allows them to be fabricated on an SU8 membrane carried on a glass substrate, the transparency of these layers enabling the use of transmission illumination. However, not all samples were fabricated on transparent substrates. The GIS system 3.3.2 benefits from a conductive substrate, and although initial tests were performed using ITO covered glass, the resulting deposition and pattern quality was a lot better when working with silicon substrates. In order to be able to measure diffraction pattern generators fabricated using Electron-Beam Induced Deposition, the Fourier microscopy setup was adjusted to work for illumination and imaging in reflection.

In order to achieve the compatibility with opaque samples, a beam splitter was added to the setup between the first and second lenses of the system, having focal lengths of 25 mm and 50 mm, respectively. This allowed the laser beam to enter the system at a 90° angle, as illustrated in figure 4.9. The collimated laser beam is focussed onto the back focal plane of the objective by the tube lens, and appearing from the front end of the objective to provide the sample with a collimated illumination

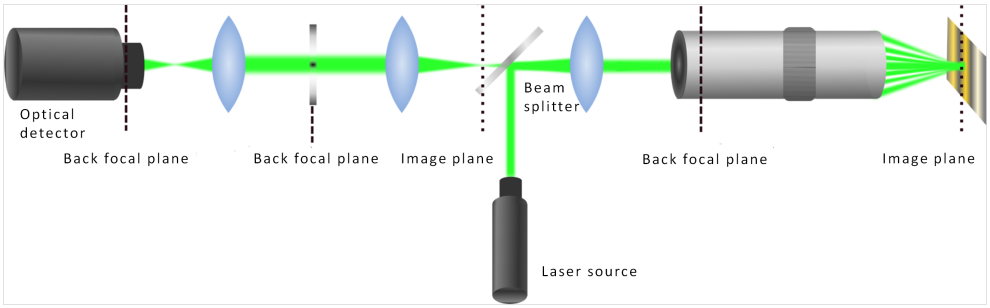

Figure 4.9 – A birefringent mirror is added to the setup and the light source is moved to enable the setup to work in reflection and accommodate opaque samples.

source. The reflected, diffracted light is sent back through the objective and tube lens, after which 50% of the diffracted light passes through the beam splitter towards lens 2. Losses resulting from the use of the beam splitter were partially compensated by increasing the power of the laser source, and the resulting Fourier diffraction patterns were visible on the detector. The light further propagates through the system, passing through the beam block if necessary, and lens 3 forming a focussed image of the back focal plane onto the detector.

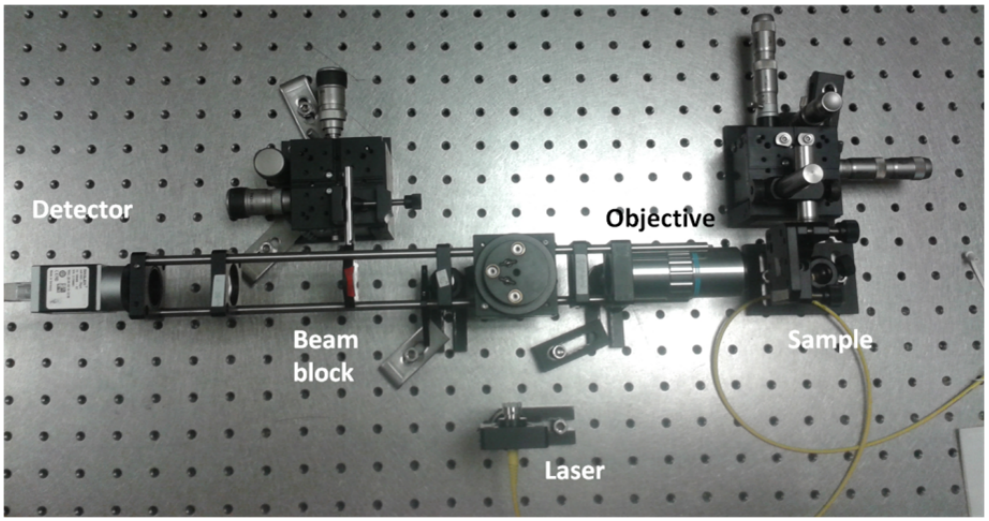

Figure 4.10 – Photograph of the Fourier microscope setup for operation in reflection. The 532 nm laser beam enters the setup from the bottom of the image, being reflected at a 45 ° angle by a beam splitter placed between the tube lens (f = 25 mm) and second lens (f = 50 mm) of the system. The sample holder and beam block are both mounted on three-dimensional translation stages to enable precise alignment. The third lens in the system (f = 35 mm) provides a 1-to-1 translation of the back focal plane to the detector.

Adapting the system for use in reflection added several extra alignment complications. The direction of the laser beam and the beam splitter has to be adjusted to achieve propagation of the laser beam along the optical axis of the system, and obtain perpendicular and collimated incidence of the laser onto the sample. Figure 4.10 shows an image of the Fourier microscope set up to operate in reflection, with a reflective silicon sample mounted on the sample holder.

Chapter 5

Results

This chapter will present results obtained throughout the course of this project. The work performed for the project was mostly fabrication-based, and can be separated into two distinct categories: traditional plasmonic structures and electron-beam induced deposition-based structures. A first section of the chapter deals with the results from the chirped grating application (see section 3.2), while a second part of this chapter covers results obtained through electron-beam induced deposition using the Raith E-Line Plus nanofabrication tool [143].

5.1 Chirped Gratings

5.1.1 Chirped grating design theory: Equivalence of blazed and chirped diffraction gratings

In order to design a discrete planar equivalent of blazed diffraction gratings, the relationship between chirped gratings and blazed gratings in relation to light interaction had to be understood on a more fundamental level. Figure 5.1 shows a single period of a blazed grating, a triangular profile defined by the refractive indices of the grating material and environment, and the height and width of the blazing triangle, sometimes expressed in terms of the blazing angle ($Asin(\frac{d}{\sqrt{d^2+\Lambda^2}})$) with d the height of the blazing triangle, and Λ the length of the blazing triangle, and the periodicity of the blazed grating. Starting from the lefthand side of the triangle in figure 5.1, light propagating at perpendicular incidence (along the y-axis), will cover an entire triangle-height d in the grating material. Moving to the right along the x-axis, the proportion of light travelling through medium n_2 decreases linearly from 100% of height d to 0% at the righthand tip of the triangle at $x = \Lambda$. This linear variation in propagation distance through n_1 andn_2 is equivalent with a linear change in optical path length.

If, in order to be used in a Fourier transform context, this configuration is expressed as phase contributions collected while propagating across the height d of the grating, it reads:

$$\phi = \frac{2\pi d}{\lambda}(n_1\frac{x}{\Lambda} + n_2(1 - \frac{x}{\Lambda})) \tag{5.1}$$

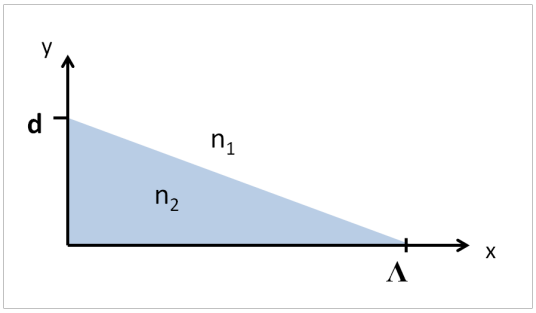

Figure 5.1 – A single period within a blazed grating. The grating characteristics can be defined by the refractive indices of the blazed grating material (n_2) and the environment (n_1), and the blazing angle, here expressed using the height d and width Λ of the blazing triangle.

which returns a phase contribution entirely inside the grating material for x = 0 ($\frac{2\pi d}{\lambda} n_2$), and entirely outside of the grating material for x = Λ ($\frac{2\pi d}{\lambda} n_1$). This optical path length difference caused by the refractive index difference is the cause of the diffraction pattern. In the case of a blazed grating, the optical path length varies linearly along a single blazed grating period.

It is also clear that diffraction gratings impose a similar optical path length difference, in this case expressed by the grating constant $\frac{2\pi}{\Lambda}$ as shown in figure 3.14, with Λ the grating period. In order to find out how to a linear change of this induced optical path length using diffraction gratings, the effects of blazed grating diffraction are analysed in more detail below.

If no grating was present, the optical path length would lie entirely in n_1, as is the case as x = Λ, so the optical path length change or phase addition depends entirely on the height and material of the blazed triangle at each location along the x-axis.

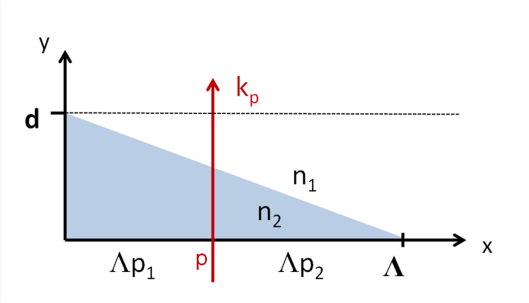

Figure 5.2 – Light transmitted through the blazed grating propagates through the grating material and through the surrounding environment (often air), the proportion of pathlength travelled through each material varies along the length of the blazed grating triangle and is expressed in the picture as Λp_1 and Λp_2 .

The wave vector k of incident light can be described as $\frac{2\pi}{\lambda}$, and it is possible to determine the wave vector of light propagating through a blazed grating at normal incidence, taking d as the maximum height of the grating, and Λ as its length. Take k_p to be the wave vector of light propagating through the grating at distance p from the left corner of the grating, as shown in figure 5.2. This means the light propagates through the environment (n_1) of the grating for a fraction $p_1 = \frac{p}{\Lambda}$ of the total height d, and the remainder of the height $p_2 = 1 - p_1$ propagates through the grating material (n_2). The total wave vector k_p can be expressed in terms of wave vectors k_1 and k_2 propagating through the environment and grating material:

$$k_p = p_1 k_1 + p_2 k_2 \tag{5.2}$$

With

$$k_1 = \frac{2\pi n_1}{\lambda_0} \tag{5.3}$$

$$k_2 = \frac{2\pi n_2}{\lambda_0} \tag{5.4}$$

If the grating was not present at all, k_p would be equal to k_1, so in order to find an expression for the added momentum caused by the grating, k_p will be expressed in terms of k_1 plus an extra term. To achieve this expression we add and subtract n_1 from the expanded form of k_2:

$$k_2 = \frac{2\pi n_2 + (n_1 - n_1)}{\lambda_0} \tag{5.5}$$

This can be reorganised to read:

$$\begin{aligned} k_2 &= \frac{2\pi n_1}{\lambda_0} + \frac{2\pi(n_2 - n_1)}{\lambda_0} \\ &= k_1 + \frac{2\pi(n_2 - n_1)}{\lambda_0} \\ &= k_1 + \gamma \end{aligned} \tag{5.6}$$

where

$$\gamma = \frac{2\pi(n_2 - n_1)}{\lambda_0} \tag{5.7}$$

Substituting this expression into the expression for k_p renders:

$$k_p = p_1 k_1 + p_2 k_1 + p_2 \gamma \tag{5.8}$$

$$= k_1 + p_2 \gamma \tag{5.9}$$

The blazed grating adds an amount of momentum to light propagating through it equal to $p_2\gamma$, with p_2 varying linearly from 0 to 1 along the blazed period length.

If blazed gratings add momentum to propagating light varying linearly along a single blazed grating period, then the goal of this application is to find a planar structure which creates a discrete equivalent of this effect. It is well-known that periodic diffraction gratings add momentum upon reflecting or transmitting light, in an amount proportional to the period of the grating. As a consequence,

changing the period of the grating changes the amount of momentum added. This is where the idea of a chirped grating emerges. Starting from a base (minimum) period, the periodicity of each subsequent grating element is increased by a small amount until a maximum period is reached. The entire set of elements with slightly varying periodicity is repeated many times to form a structure with set superperiodicity. The chirped grating as described here has many parameter values which have to be decided upon, including the base period, the manner and amount by which the period of each subsequent element is increased, the duty cycle of each element, etc. Will the efficiency of the grating increase if each groove keeps the same width, or should it be determined as a fraction of the total periodicity? Is there an optimal fill factor proportion or air and metal, and can varying this duty cycle for each individual element optimise plasmonic resonances to achieve increased efficiency?

The designs executed during the project all concern linear changes in the chirp of the grating periodicity, although other variations in periodicity could potentially lead to more beneficial results.

Starting from the grating equation

$$n_2 sin(\theta_m) - n_1 sin(\theta_{in}) = \frac{m\lambda}{\Lambda} \tag{5.10}$$

It is possible to transform this equation to be expressed for wave vectors by making the following substitution:

$$\lambda = \frac{2\pi}{k} \tag{5.11}$$

Which leads to

$$n_2 sin(\theta_m) - n_1 sin(\theta_{in}) = \frac{2\pi m}{\Lambda k} \tag{5.12}$$

And can be rearranged to read

$$k n_2 sin(\theta_m) = k n_1 sin(\theta_{in}) + \frac{2\pi}{\Lambda} m \tag{5.13}$$

In this equation $\frac{2\pi}{\Lambda}$ is often referred to as the grating constant, and it represents the amount of momentum added to the light by the grating. From the equation it is clear that a periodic diffraction grating adds an amount of momentum equal to an integer number of grating constants to diffracted light. Based on these calculations it would be beneficial to design and fabricate samples which have a linearly varying grating constant, instead of grating period, to see if this more closely approximates blazed grating functionality.

5.1.2 Chirped grating design theory: Mathematical analysis of blazed gratings

The following mathematical analysis of diffraction by a blazed grating in transmission. The change in momentum resulting from light propagating through a grating is discussed in section 5.1.1 on blazed gratings. The phase change $b(x)$ introduced by a single period of a blazed grating can be expressed using the symbols of figure 5.1, and based on expression 5.1:

$$b(x) = exp(j\frac{2\pi}{\lambda}(n_2 - n_1)\frac{xd}{\Lambda} - j\frac{2\pi d}{\lambda}n_2) \tag{5.14}$$

In order to understand the effect of a blazed grating on the diffraction pattern of transmitted light in the far-field, a Fourier transform of the above expression of a single blazed grating period is performed, as explained section 4.1.2 in the chapter on Fourier microscopy. The following calculations are based on lecture and syllabus notes of the Microphotonics course by Professor Roel Baets [19], and are provided detailing the several required steps to achieve the Fourier transform in order to aid the reader in gaining understanding and encourage intuitive interpretation of the Fourier transform.

$$\begin{aligned} B(f_x) &= \int_{-\infty}^{\infty} b(x)exp(-j2\pi f_x x)dx && (5.15)\\ &= \int_0^{\Lambda} b(x)exp(-j2\pi f_x x)dx && (5.16)\\ &= \int_0^{\Lambda} exp(j\frac{2\pi d}{\lambda}(n_2(\frac{x}{\Lambda} - 1) - n_1\frac{x}{\lambda}))exp(-j2\pi f_x x)dx && (5.17)\\ &= exp(-\frac{j2\pi dn_2}{\lambda})\int_0^{\Lambda} exp(-j2\pi(f_x - (n_2 - n_1)\frac{d}{\lambda\Lambda})x)dx && (5.18) \end{aligned}$$

Abbreviating this expression slightly by substituting $\alpha = (f_x - (n_2 - n_1)\frac{d}{\lambda\Lambda})$, the expression becomes:

$$\begin{aligned} B(f_x) &= exp(-\frac{j2\pi dn_2}{\lambda})\int_0^{\Lambda} exp(-j2\pi\alpha x)dx\\ &= exp(-\frac{j2\pi dn_2}{\lambda})[\frac{-1}{j2\pi\alpha}exp(-j2\pi\alpha x)]_0^{\Lambda}\\ &= exp(-\frac{j2\pi dn_2}{\lambda})\frac{-1}{j2\pi\alpha}exp(-j\pi\alpha\Lambda)(exp(-j\pi\alpha\Lambda) - exp(j\pi\alpha\Lambda))\\ &= exp(-\frac{j2\pi dn_2}{\lambda})\frac{-1}{j2\pi\alpha}(-2jsin(\pi\alpha\Lambda))exp(-j\pi\alpha\Lambda) \end{aligned} \tag{5.19}$$

In the above equations, the integral was calculated, and an expression of complex integrals simplified to a sine expression. The full expression for α will now be reintroduced into the equation, with $(n_2 - n_1)\frac{d}{\lambda\Lambda}) = f_0$, a constant representing a spatial frequency.

$$B(f_x) = exp(-\frac{j2\pi dn_2}{\lambda})\frac{sin(\pi(f_x - f_0)\Lambda)}{\pi(f_x - f_0)}exp(-j\pi(f_x - f_0)\Lambda) \tag{5.20}$$

As we are interested in the intensity profile of B(f_x), the relevant quantity is $|B(f_x)|^2$, all imaginary components in the above expression cancel out, leaving the final expression for the Fourier transform of a single triangular grating period to be:

$$|B(f_x)|^2 = \frac{sin^2(\pi(f_x - f_0)\Lambda}{(\pi(f_x - f_0))^2} \tag{5.21}$$

This $sinc^2$ function has a maximum for $f_x - f_0 = 0$, and minima for $\pi(f_x - f_0)\Lambda = l\pi$, with $l \neq 0$, suggesting blazed gratings direct the majority of intensity to a single diffraction order f_0.

A blazed grating consists of more than just a single grating period in reality, and adding this periodic repetition to the Fourier transform adds an extra factor to the functions for b(x) and B(f_x) above, this factor standard for all periodically repeating structures. For a grating with N periods, this becomes:

$$b(x)_N = \sum_{k=0}^{N-1} b(x - k\Lambda) \tag{5.22}$$

In the Fourier analysis this results in an extra factor added to the expression

$$\begin{aligned} \sum_{k=0}^{N-1} exp(-j2\pi k f_x \Lambda) &= \frac{1 - exp(-j2\pi N f_x \Lambda)}{1 - exp(-j2\pi f_x \Lambda)} \\ &= exp(-j\pi(N-1)f_x\Lambda)\frac{sin(\pi N f_x \Lambda)}{sin(\pi f_x \Lambda)} \end{aligned} \tag{5.23}$$

As the intensity is the value of interest, the imaginary exponential term is neutralised in this expression. Combining the effect of the blazed grating with the periodic repetition, the Fourier transform of expression 5.22 becomes:

$$B(f_x) = \frac{sin^2(\pi N f_x \Lambda)}{sin^2(\pi f_x \Lambda)} \frac{sin^2(\pi(f_x - f_0)\Lambda}{(\pi(f_x - f_0))^2} \tag{5.24}$$

The lefthand fraction is caused by the periodic structure of N repeats of the blazed grating triangle, while the righthand fracture is caused by the triangular shape of each individual period. The left fracture reaches a maximum when the denominator equals zero, so for $f_x = \frac{k}{\Lambda}$, for all integer values of k ($k \in \mathbb{Z}$). In this case, the numerator equals zero as well, as N is an integer and $sin(Nk\pi) = 0$ with N, $k \in \mathbb{Z}$.

For these cases the righthand side of expression 5.24 reaches a maximum when the denominator equals zero, which is only the case for $f_x = f_0$, which occurs for a value of $k = k_0$:

$$
\begin{aligned}
f_x &= f_0 \\
\frac{k_0}{\Lambda} &= (n_2 - n_1)\frac{d}{\lambda\Lambda}) \\
k_0 &= (n_2 - n_1)\frac{d}{\lambda}, k \in \mathbb{Z}
\end{aligned}
\tag{5.25}
$$

If the above expression has a solution for an integer value value of k, called k_0, then the numerator will be zero for all values of k, and reach a minimum for all values of $k \neq k_0$. These minima overlap with the maxima of the lefthand fracture of the entire expression, meaning that there is only one value of f_x for which both fractures reach a maximum:

$$
f_x = k_0\Lambda \tag{5.26}
$$

The above mathematical analysis illustrates why a blazed grating is able to direct the majority of the light into a single diffraction order. The order which light is diffraction into is determined by the design parameters and material properties of the blazed grating: n_1, n_2, d, and Λ.

Blazed gratings designed to reflect light to a high order, by having parameter values resulting in a large k_0 value, are also called echelle, or echellette gratings. The diffraction angle of light, especially broadband light, is spread out more at these higher orders, due to the higher order number increasing the dispersion effects: the variation in values for θ for a wavelength range increases as m (proportional to k_0) increases, as can be told from the grating equation: $sin(\theta_m) = \frac{m\lambda}{d}$.

5.1.3 Simulation Design Results

As described in the fabrication chapter (3.2) many parameters play a role in the performance and efficiency of a chirped diffraction grating. As the fabrication cycle for a single sample could easily take a week, testing all parameter settings experimentally would be a time, energy, and resource-consuming activity. The chirped gratings are designed with a particular goal in mind: to achieve high-efficiency diffraction to high orders at perpendicular incidence to achieve overlapping diffraction orders, and in order to tell whether this has been achieved, the far-field diffraction pattern can be analysed. Using a combination of COMSOL Multiphysics (version 4.4) [152] simulations and Matlab [153] code, the this could be achieved.

COMSOL Multiphysics [152] was used to simulate the chirped grating diffraction patterns, and the far-field analysis was performed using functions written in Matlab [153]. A single chirped grating superperiod was designed in Comsol, and periodically repeated using the periodicity tool available in the software package. Initially, it was attempted to perform the far-field analysis using the Comsol far-field tool, but when test results using basic dielectric periodic gratings did not return a sensible far-field diffraction pattern, further investigation found that the periodicity and far-field tools could not be combined.

In order to move the far-field outside the Comsol package, the 2D light distribution pattern (e.g. see

figure 5.3) was exported from Comsol in a 2D array, each cell representing the intensity value on a pixel in the image in real space. To obtain a far-field pattern, this 2D image was Fourier-transformed in Matlab [153], example code for this process, using a generated 2D matrix for analysis is shown in figure 5.4.

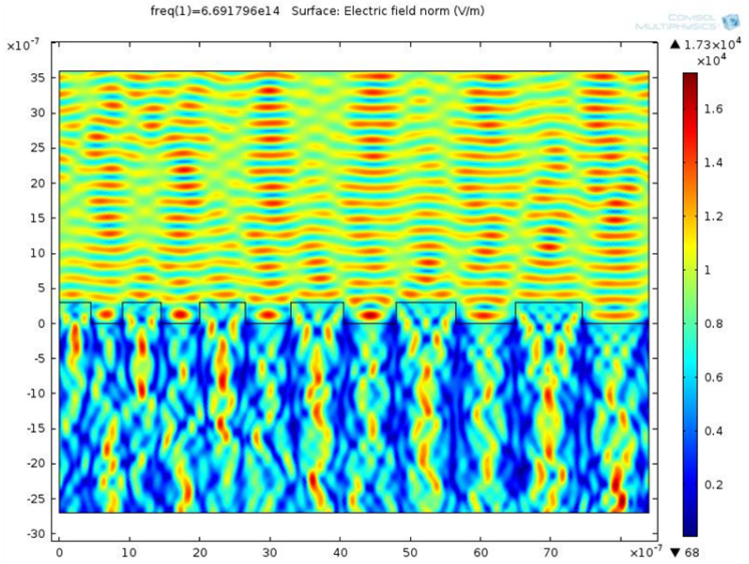

Figure 5.3 – A light distribution pattern of a chirped diffraction grating of a plane wave at normal incidence, obtained using COMSOL Multiphysics [152].

```
x = linspace(0,20e-6,1000);
y = linspace(0,40e-6,2000);

[X,Y] = meshgrid(x,y);

A = exp(-i*2*pi/600e-9*(cos(pi/6)*X+sin(pi/6)*Y));
B = exp(-i*2*pi/600e-9*(cos(pi/4)*X+sin(pi/4)*Y));

fA = abs(fft2(real(A+10*B))).^2;

dx = x(2)-x(1);
dy = y(2)-y(1);

kx = 1/dx*600e-9*(0:length(x)/2-1)/length(x);
ky = 1/dy*600e-9*(0:length(y)/2-1)/length(y);

%plot graph of the spatial frequencies expressed
pcolor(kx,ky,log(fA(1:1000,1:500)))
shading interp
```

Figure 5.4 – An illustration of Matlab 2D Fourier transform script code. A Matlab generated 2D matrix of a superposition of two waves at different angles of incidence ($\frac{\pi}{6} and \frac{\pi}{4}$ degrees) is Fourier transformed, scaled, and plotted to represent the propagation angles represented by their values on the k_x and k_y axes.

The code was adapted to analyse comsol-generated real-space light distributions instead of Matlab-generated ones, and enhanced to increase legibility and interpretation of the resulting Fourier graph. The code was first tested using a simple air-dielectric interface and planar wave incidence. The behaviour of this setup is described by Snell's Law ($n_{air} sin(\theta_{air}) = n_d sin(\theta_d)$). As can be seen from figure 5.5, the Comsol simulation of the light distribution pattern of a plane wave hitting the

periodically repeated simple air-dielectric boundary behaves according to Snell′s Law with a simple refraction of the light at the boundary. The righthand panel of figure 5.5 shows the Fourier transform of the code of figure 5.4. This initial Fourier transform and visualisation required amendments to increase legibility.

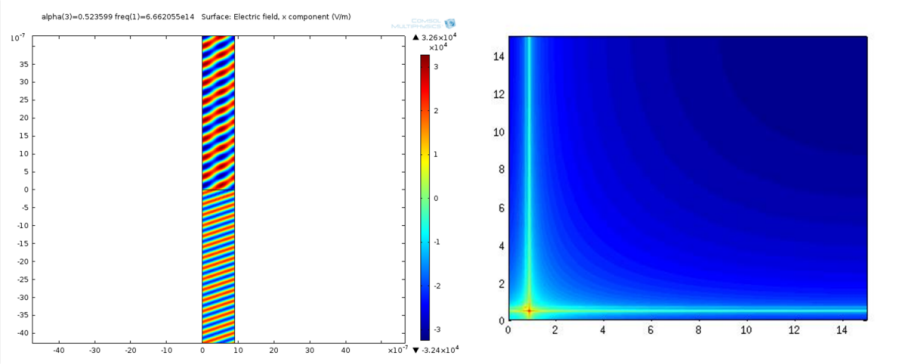

Figure 5.5 – The left image is a Comsol illustration of the light electric field distribution of a plane wave being refracted by an air-dielectric interface according to Snell's Law. The righthand image contains a Fourier plot of the the code shown in figure 5.4, showing the $\frac{\pi}{4}$ and $\frac{\pi}{6}$ waves.

To facilitate the interpretation of the results on the Fourier plot, the axes were scaled to return the sine and cosine values of the direction light travels in, multiplied by the refractive index of the medium in which the light travels. Circles were can be added to indicate the refractive indices present in the simulated setup, and to illustrate that all diffracted light is represented by peaks along these circles, representing the refractive index of the medium. Figure 5.6 shows a graph containing such circles, and the data represents the Fourier transform of a diffraction pattern resulting from a chirped dielectric grating in air. Further code was written to enable users to select the N highest peaks in the Fourier transform graph, and return their relative intensity and diffraction angles. The peaks can be used to easily determine if the goal of high-efficiency diffraction ot a set of overlapping orders has been achieved.

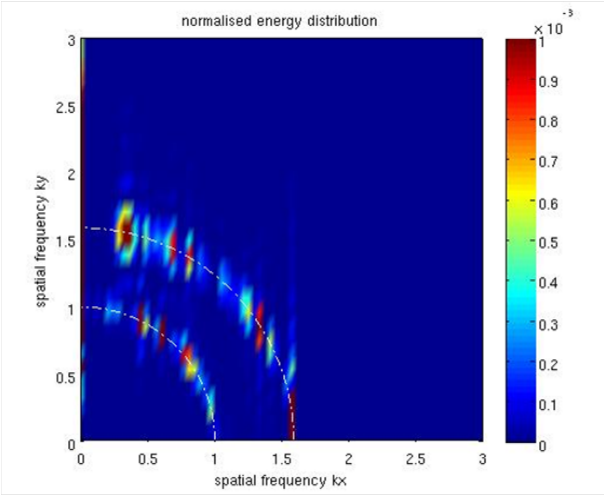

Figure 5.6 – Fourier plot of a plasmonic chirped grating of a periodic repeat of a supercell containing 12 Au grating strips with a height of 35 nm, and with 100nm chirp. The wavelength used for the simulation was 400 nm. The outer circle represents diffracted light in transmission, and the smaller circle shows diffracted light in reflection.

5.1.4 Experimental Results and Characterisation

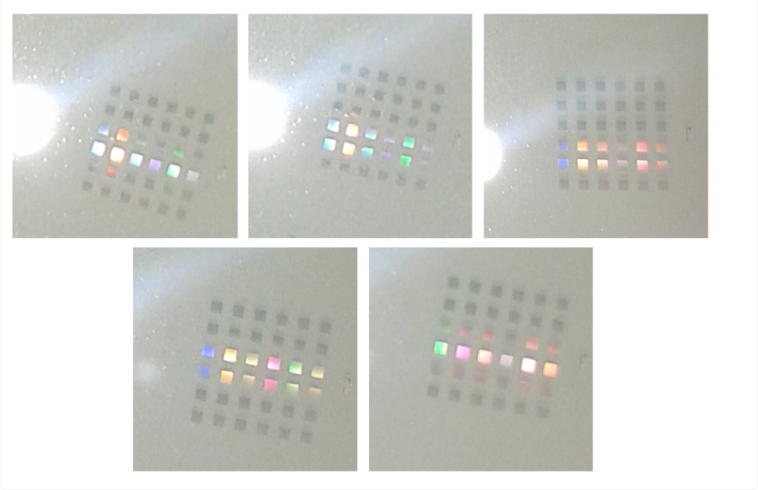

Figure 5.7 – An array of chirped gratings with variable chirp parameters reflecting broadband light, showing their characteristic colourful diffraction patterns.

This section discusses the experimental results obtained with chirped gratings and covers the visualisation of the fabricated samples, both with the naked eye and using an SEM, and characterising their interaction with light. The chirped grating samples produced during this project were meant for fabrication dose tests, measurement tests, and initial characterisation attempts. The gratings were produced to be similar in size to the diameters of the used lasers beams, having dimensions around 500 μm to 1 mm. A sample usually contains an array of 16 to 40 individual gratings, to test several parameter settings. Figure 5.7 contains an image of a standard sample, showing an array of gratings with different dose, chirp, and superperiodicity parameter values. A well-known characteristic of gratings is the colourful diffraction patterns they produce when illuminated, which can be observed in the figure 5.7, where the sample is illuminated with a white light source (a phone flashlight). Fabrication of the chirped gratings is discussed in detail in chapter 3.2.4. Figure 5.8 contains an example of an SEM image of a successfully fabricated chirped grating. The cleancut straight, narrow lines suggest accurate dosing, focussing, and alignment for the chosen pattern design settings.

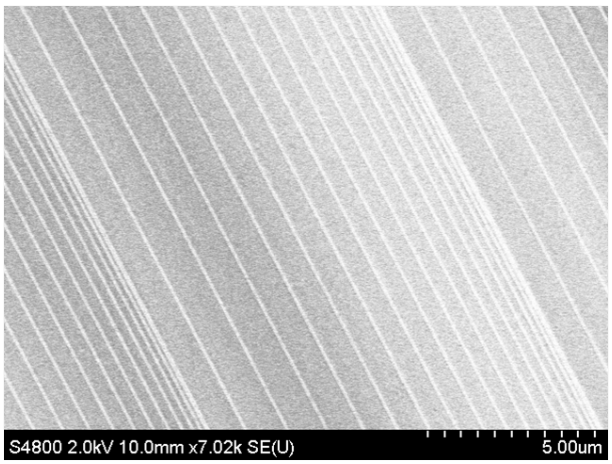

Figure 5.8 – After testing various design and patterning parameters, the settings could be chosen to achieve high quality gold on SU8 chirped gratings. In the above image a 10 μm superperiod with a single pixel line grating and 100 nm chirp was chosen.

To probe the chirped grating functionality, a broadband source measurement was performed on set of gratings with different dose, chirp, and superperiodicity values, using a NKT SuperK supercontinuum laser providing broadband coherent light with a bandwidth of 450nm - 2400 nm, for visualising the diffraction of the chirped grating. The comparisons between broadband diffraction for different chirp and superperiodicity values in figure 5.9 suggest that the main factor playing a role in establishing the diffraction pattern is the periodic grating caused by the supercells with superperiodicity. The chirp does influence the pattern (as shown in the different colour arrangements in figure 5.9 (a) and (b)), but only to a limited extent. It is also not certain that these observed differences are caused by the chirped functionality itself, as they could also be due to the effects of chirp on fill-factor influencing the overall efficiency of the periodic grating resulting from the supercells. For detailed and accurate analysis of the diffraction pattern quantitative spectral and intensity measurements will be required. A first improvement in the measurement of the sample was to analyse the diffraction angles more accurately and make it possible to view higher diffraction orders, using the Fourier setup described in chapter 4.1.

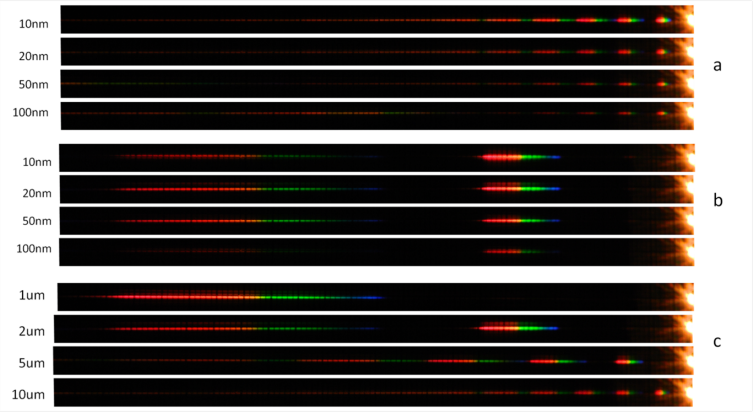

Figure 5.9 – Broadband diffraction patterns of chirped gratings taken at normal incidence. (a) Shows a comparison for different chirp values for a superperiod of 10 μm, where (b) shows the same range of chirp values for a superperiod of 2 μ. In figure (c) a comparison of different superperiodicities is shown, all with 20 nm chirp.

When placing chirped gratings in the Fourier setup for analysis, a beam block was required to obscure the zeroth order intensity, due to the low efficiency of the fabricated gratings. The measurements confirmed the earlier observations that the diffraction patterns follow the behaviour of a periodic grating having the supercell as its basic period, and do not direct light into a single higher order. The setup does provide the tool to determine the propagation direction for each diffracted order, as shown in figure 5.10(b), returning significantly more legible and interpretable results than real space images (e.g. figure 5.10(a)). If 532 nm Nd:YAG laser source would be replaced with a broadband collimated source, this analysis could be performed for a wide range of wavelengths to obtain a detailed wavelength-specific diffraction map, a useful tool for assembling the one-to-one wavelength-to-location 2D array.

5.1.5 Future Work

The limitations and possibilities of the chirped grating fabrication process are well understood, and the experiments performed during this project have confirmed basic ranges for fabrication pattern-

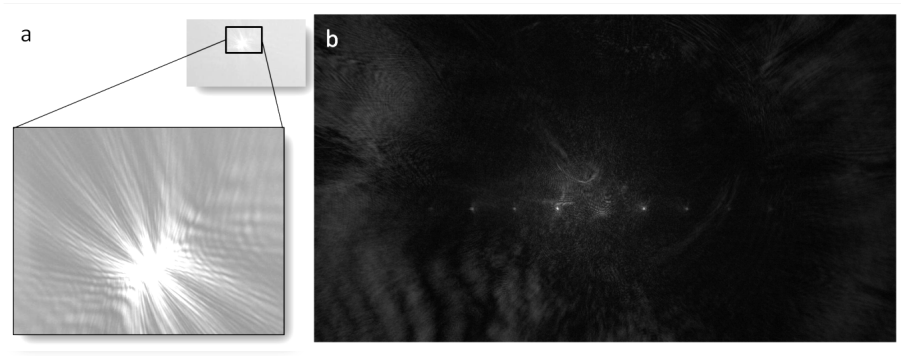

Figure 5.10 – Figure (a) shows a real-space image of a camera focussed on a sample with a periodic tungsten EBID grating, figure (b) in comparison is a Fourier image of a chirped grating diffraction pattern, using a zeroth order beam block.

ing settings which result in successful sample preparation. Future work in the area should focus on optimising the design parameter values, and once a particular design is decided upon, a dose test fabrication run can be performed to select the optimal set of settings.

A first area where more research should be performed is the determination and further clarification of the link between the different design parameters (e.g. fill-factor, superperiodicity, base period, chirp etc.) and the efficiency of the chirped gratings. For samples made throughout the course of the project, at normal incidence, the majority of the light got diffracted into the zeroth order. This could be due to a multitude of reasons, including the fact that the tested chirped grating patterns are very small and therefore do not fully cover the diameter of the incident beam. Producing samples with a constant single pixel line width leads to a mostly empty space as the periodicity increases (for large chirp and superperiodicity values), and in these cases it is possible that the narrow gold strips are not enough to interact with all the incident light, which is why it is essential for the optimal fill-factor to be researched.

A second task is to confirm if, when using an appropriate set of design parameters, high efficiency diffraction to a single higher order can be achieved using chirped gratings. The experimental confirmation of the equivalence between blazed and chirped diffraction gratings for a certain set of parameters would be interesting, although not essential for the functionality of the project, as blazed gratings are not the only tool which can assist in achieving the desired one-to-one frequency-location map.

A third activity which should be pursued is to search for Wood′s anomalies [156] [157] to confirm the presence of plasmonic effects. One way this could be achieved is to include quantitative intensity analysis to the Fourier microscopy setup discussed below in section 4.1.

The chirped grating application is aimed at creating a two-dimensional light array mapping frequency to location. Several attempts were performed to create he second perpendicular grating on top of the first chirped grating. However, none of the sample runs were successfully completed, as the alignment of the second grating on top of the first is complicated by the thick spacer SU8 polymer layer (1:1 SU8 2000.5 : SU8 2050 [115] [117] spincoated at 2000 rpm, 2 min UV exposure, and 5 min bake at 100°) and the gold layer masking the underlying chirped grating structures and potential alignment markers. The function of the second perpendicular grating was illustrated on a larger scale by man-

ually placing a dielectric grating in behind the chirped grating and observing the diffracted light. While the development of the first (chirped) grating was still in progress, adding the second grating was put on hold. Once the chirped grating performance and functionality is better understood, the second perpendicular grating can be added on top of the chirped grating and the second diffraction direction can be explored. As this step involves a well-understood simple periodic grating design, and functionality was already illustrated with a separate grating, the research into grating parameters should have a narrower focus.

5.2 Electron Beam Induced Deposition

Fabrication procedures used to make nanoscale structures are often complex and require a large amount of understanding and experience. With the arrival of the Raith E-Line Plus nanoengineering system [143], containing the Gas Injection System, this experience had to built up within the Synthetic Optics group. The results of this part of the project therefore include the development of fabrication and characterisation methods as discussed in section 3.3.2, and based on these findings, the design and development of specific experiments and potential applications. The results discussed below focus on different types of structures achieved through fabrication, especially those types of designs which are hard to fabricate using traditional lithography techniques. Part of the project was also aimed at developing ways of characterising the optical response of the fabricated structures using alternative plasmonic materials, aiming to determine if a plasmonic response could be detected and quantified from the EBID-based tungsten material. However, challenges arose as a result of the small scale of the written patterns, making the structures hard to locate on the sample using the setup initially developed for the much wider-area spanning chirped diffraction grating samples. This difficulty to detect the structures complicated the detection of a response.

5.2.1 Fabrication procedure

Based on tutorials by Raith technicians and on the Software reference manual [144], a detailed step-by-step fabrication procedure with basic troubleshooting suggestions was compiled, as discussed in detail in section 3.3.2. A shorter step-by-step practical user guide can be found in appendix 7.1. Table 5.1 contains an overview of determined functional writing parameter ranges for electron-beam induced deposition of tungsten.

5.2.2 Greyscale and 3D Metallic Nanoscale Patterning

A first advantage offered by the GIS system is that it makes greyscale and 3D deposition possible. When writing 3D structures the stage should ideally be moved down slightly for each consecutive layer to keep the focus of the system at the location where the material is being deposited. This can be achieved manually or through a script, if the patterns are being written using a positionlist. However, during the project it was found that this working distance adjustment is not an essential requirement to achieve small 3D structures. Tests were performed which showed that the height of the narrow columns can be varied simply by changing the dose factor. Image 5.13 shows an SEM

Table 5.1 – The table gives an overview of writing parameters used during the project to deposit Tungsten on a silicon substrate. These values and ranges are not the only possible options to obtain a tungsten deposit, they are merely example values which were found to have positive deposition results during testing.

Parameter	symbol	value
Current	I	0.18 - 0.21 nA
Dwell time	t_d	150 - 450 ms
Basic step size	s_b	10 - 20 nm
Line spacing	s_l	10 - 20 nm
Dot dose	d_d	15 - 30 pC
SPL dose	d_{SPL}	30 - 40 e^6 pC/cm
Area dose	d_a	15-40 e^6 $\mu C/cm^2$
Settling time	t_s	1 ms
EHT	V_{EHT}	3kV
Aperture	A	30μm

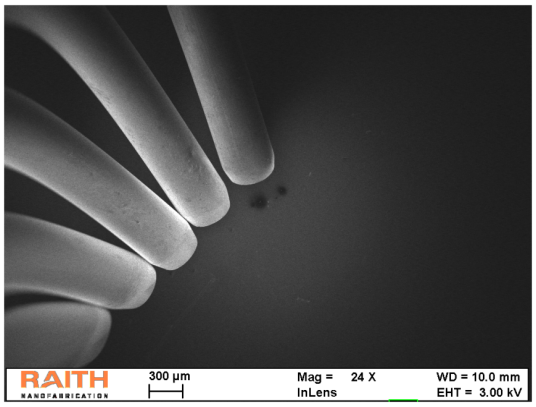

Figure 5.11 – Image of the GIS nozzles driven down to the surface to perform the electron-beam induced deposition. When zoomed out to a small magnification value, the nozzles are visible in the detector viewing window when operating the machine.

image of a test sample with narrow spiraling columns achieved by writing dots in a concentric writing configuration, at dose factors of 1, 2, 5, 10, and 20. Next to it, a concentric write of a circle resulted in a 3D helical structure by halving the basic step size, effectively quadrupling the dose per area.

Although it might seem obvious that depositing more material in a certain location by increasing the dose in that area leads to a higher deposited structure, to achieve this feature would be anything but straightforward using traditional lithography techniques. As the increased height of the structures might make them more easily detectable and change their interaction with incident light, this fabrication strategy was employed when trying to make samples intended to detect a diffraction pattern with the Fourier setup (see section 5.2.5). The SEM images shown in figure 5.14 shown a 2D array of 3D columns written attempt to cause and detect a Fourier response.

5.2.3 Point-and-Shoot Writing and Precise Alignment

When using the Gas Injection System in ad hoc writing mode, the advantages of precise alignment as a result of the point-and-shoot writing method become apparent. Next to performing dose and parameter tests for each write, using the same alignment settings and sample, it is possible to pre-

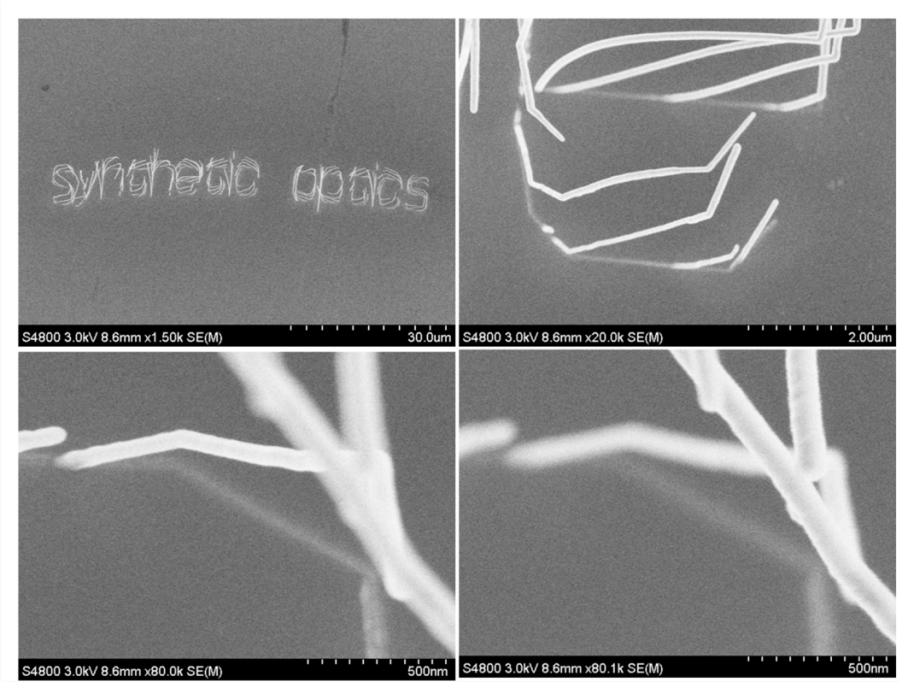

Figure 5.12 – SEM images showing an overview and close-up views of the unsuccessful write of the words *synthetic optics*. The balance between the settings was not achieved, and the deposited material detached from the substrate surface, potentially caused by a base dose for a single loop which was set too high. The images show how the material has clearly lifted off from the surface, as shown by the different points at which the branches are in focus in the bottom two images of this figure.

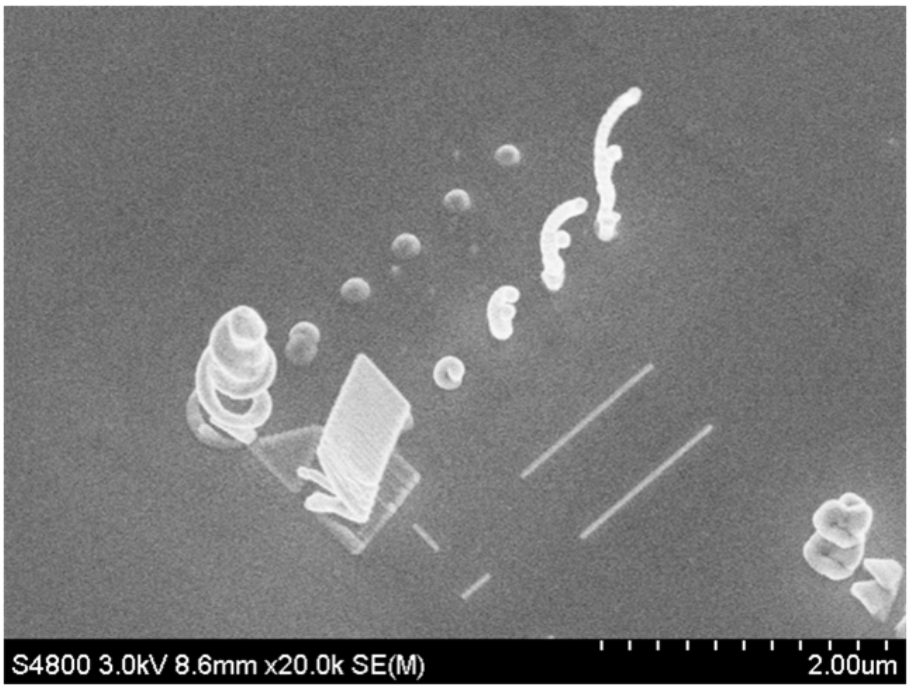

Figure 5.13 – An SEM image of the first successful 3D writing test, containing spiraling columns achieved through increasing the dose factor, and a 3D spiral caused by decreasing the step size when writing a concentrically filled-in circular structure. The image also shows the dose tests on dots, alignment issues for writing shapes, and an accidental diagonally stacked rectangular 3D structure.

cisely align and customise written features for specific sample configurations and topography.

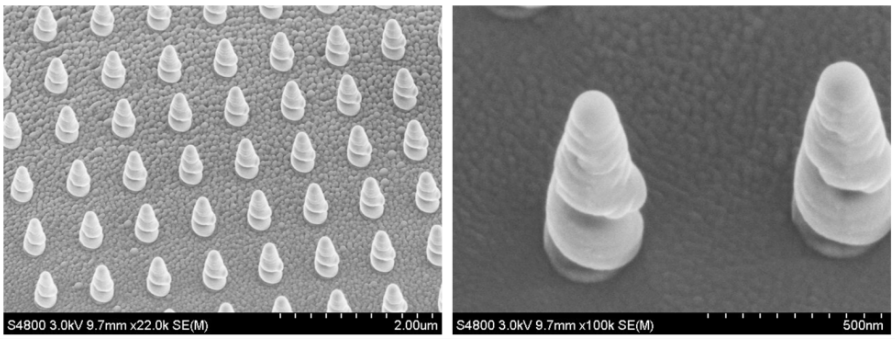

Figure 5.14 – A 2D array of 3D columns written to increase the surface area covered in EBID structures, and to stimulate an optical response, detectable by the Fourier microscopy setup.

A first example comes in the form of adding metal contacts to quantum-dot containing GaAs/AlGaAs nanowires (NW) on silica-on-silicon wafers to control their emission properties [155]. The NW samples were provided as part of a collaboration, by Dr Zhang-Kai Zhou from the School of Physics and Engineering, Sun Yat-sen University, in Ghuangzhou, China. The nanowire structures are spread randomly across the sample surface, and where the precise alignment of metal contacts on these nanowires would be an enormous challenge using traditional lithography techniques, here it can be achieved in a single step. Figure 5.15 shows two examples of metallic contacts on nanowires, in 5.15(a) the entire NW is enclosed within several deposited layers of tungsten, following a detailed path along the unique silhouette of the NW. In 5.15 (b), a metallic solid pattern has been added to one end of the NW. Grating structures like this could help couple light into a NW, and other potential designs (e.g. mirrors) could be used to increase and enhance the interaction of light with these structures (e.g. induce resonances). The images were taken with the SEM of the e-beam lithograph, as it can be challenging to relocate a single NW on a large sample covered in them.

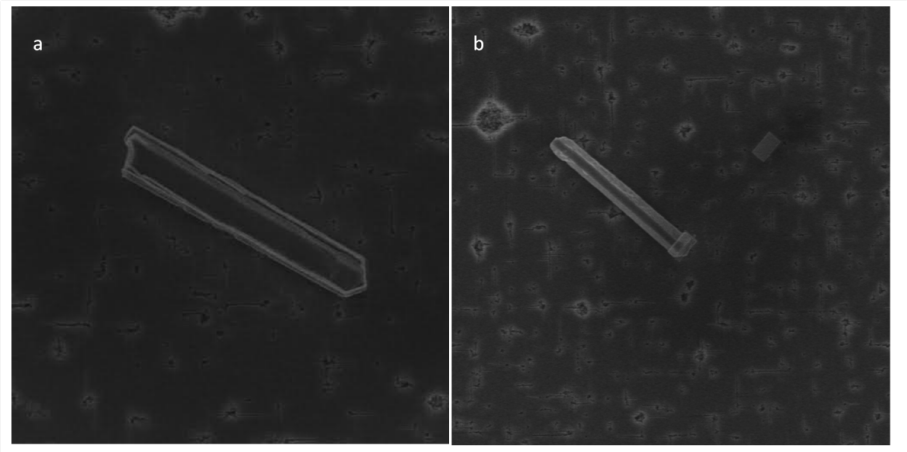

Figure 5.15 – The figure shows e-beam SEM images of metallic tungsten structures being added to individual nanowires, spread randomly across the sample surface. (a) shows a nanowire being encased by a metal coating around its edge; (b) shows a metal contact being added at the edge of a nanowire at the bottom right of the image. A test pattern has been written above and to the right of the actual contact.

A second example illustrating the benefits of point-and-shoot writing with precise alignment is the ability to write on a fibre tip. Figure 5.16 shows e-beam SEM images of a photonic crystal hollow core fibre with GIS structures added to the tip of the fibre. The fibre was loaded into the E-Line

Plus system, and the alignment procedure (see 3.3.2) was performed on the tip of the fibre, instead of at the surface of the sample holder. The already complex procedure was further complicated by the non-conductive nature of the fibre, which caused the electron beam to charge up the surface and deflect the beam, deforming both the formed image and the written patterns. The quality of the write and the SEM images is not great, and adjustments would have to be found to try and overcome the charging of the sample.

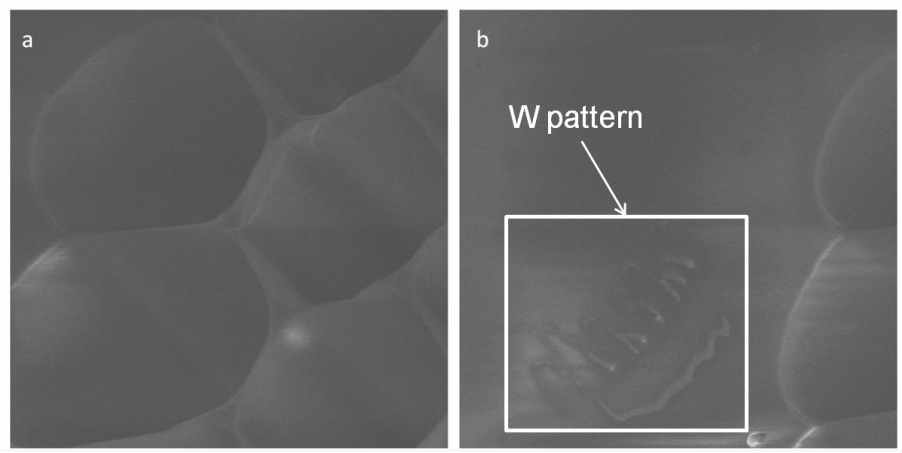

Figure 5.16 – Electron-beam induced deposition of tungsten on a hollow-core photonic crystal fibre-tip was attempted. Although some material was deposited, the lack of conductivity made the imaging and deposition unstable. Recipe settings would also require optimisation for deposition on glass and to build a bridge over the hollow cores. Image (a) shows several hollow cores, with the lighter areas indicating where material has been deposited. Image (b) illustrates how the charging up of the fibre tip interfered with the deposition patterns of straight lines.

5.2.4 3D writing on nanowires

In one of the examples above, customised features are designed and aligned to randomly placed and oriented nanowires lying flat on a silicon surface. In the following example, a sample with nanowires standing up on a GaAs surface is used, and EBID structures are added on top of the tips of the NWs, the metallic structures intended to cause plasmonic interaction with incident light. Figure 5.17 shows an e-beam SEM image of a NW standing up, before and after deposition of a circular feature on its tip. Figure 5.17 contains an overview of SEM images of several types of patterns deposited on NW tips placed at different angles. Figure 5.17(a) has two small spirals added on its NW tip, resulting in the remarkable appearance of the patterned NW tip having a pair of eyes, earning it the nickname *Nanosnake*. Figure 5.17(b) shows a circular shape added to the NW tip, which could be used to induce chiral effects. In figure 5.17(c) a simple line grating is deposited for diffracting light interacting with the nanowire, and in figure 5.17(d) a bowtie antenna shape is added to the NW tip which could be used to focus light and achieve high localised intensities.

In order to be able to take the SEM images of the patterned NWs, a system had to be found to locate the NWs on the sample surface. Figure 5.19 illustrates the method employed to achieve this. E-beam SEM images were taken at a range of magnifications, to identify the location of the patterns in a stepwise manner, from small recognisable markers on the sample substrate.

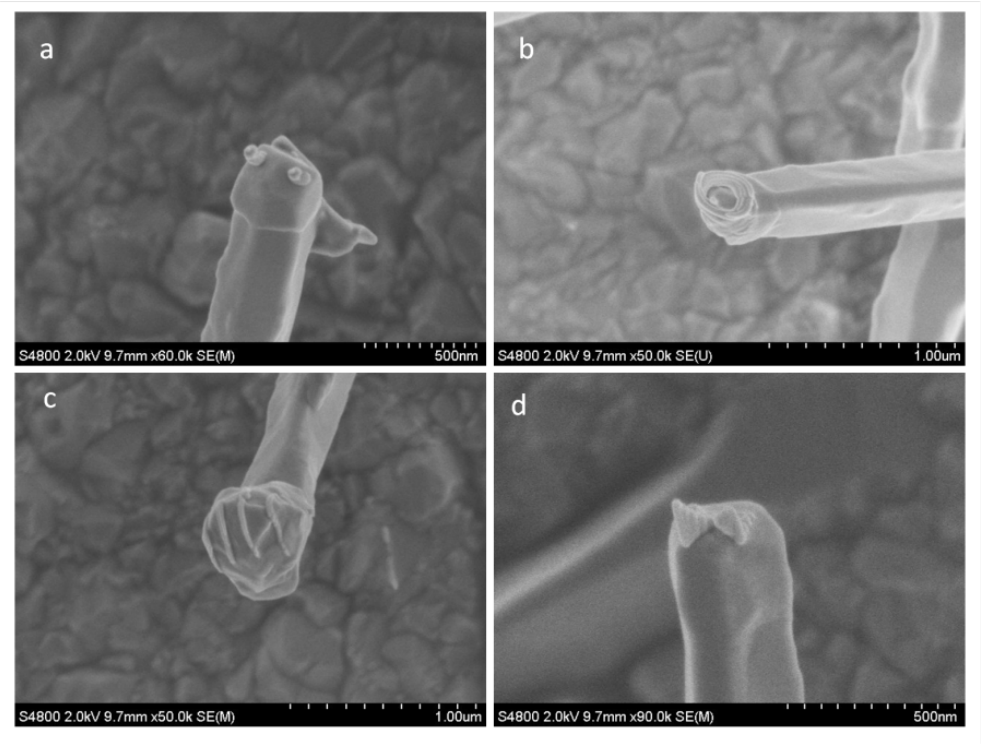

Figure 5.17 – Electron-beam induced deposition of tungsten on nanowires standing up on the sample surface. (a) shows the addition of small column on the tip of a NW, (b) has a circular feature added to the NW tip, in (c) grating lines have been added, and in (d) a triangular nanoantenna pattern has been written.

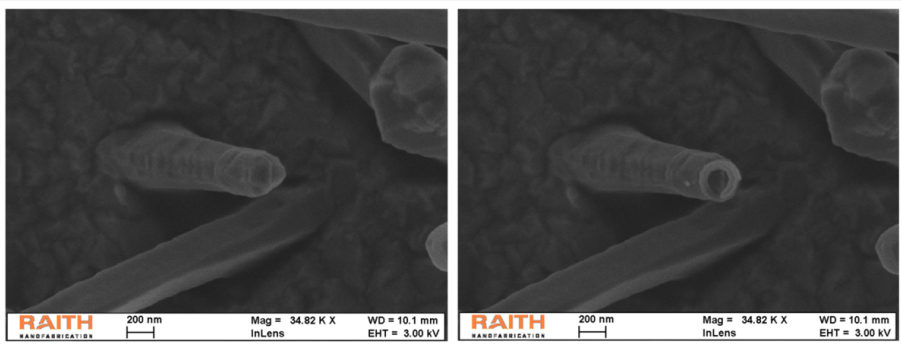

Figure 5.18 – A NW on GaAs substrate, before and after GIS electron-beam induced deposition of a circular tungsten pattern on the tip of the NW.

5.2.5 Measurement and Characterisation of EBID nanostructures

The Fourier setup as it was built relied on visual alignment of the laser beam onto the structures on the sample. This was no issue for the chirped grating samples as they tended to be visible with the naked eye, being several square millimeters in size. However, the EBID patterns written onto samples covered areas in the range of square micrometres, making them harder to detect.

Their small size is not the only property of the tungsten on silicon structures complicating their detection. The silicon substrate and tungsten deposited material are visually very similar, with a metallic shiny look and silvery colour. The very thin thickness of the deposited tungsten is in the range of tens of nanometers, and the low contrast in both depth and visual response makes these tungsten

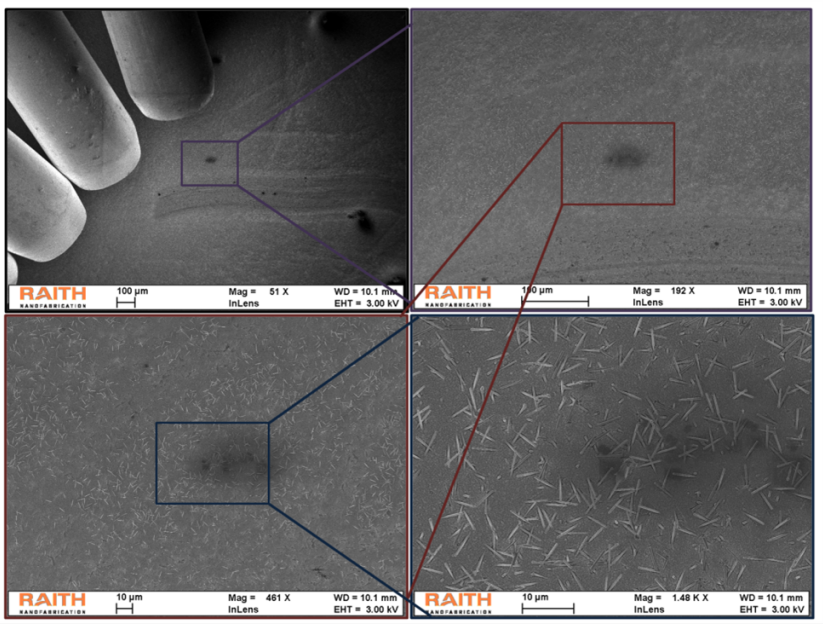

Figure 5.19 – A method for locating patterned features using a series of images at different magnifications to track down the patterned nanowires by zooming in to the correct location based on the map.

structures hard to detect on the silicon substrate even with an optical microscope. Figure 5.20 shows the optical microscope and SEM images of a periodic grating structure from EBID tungsten material.

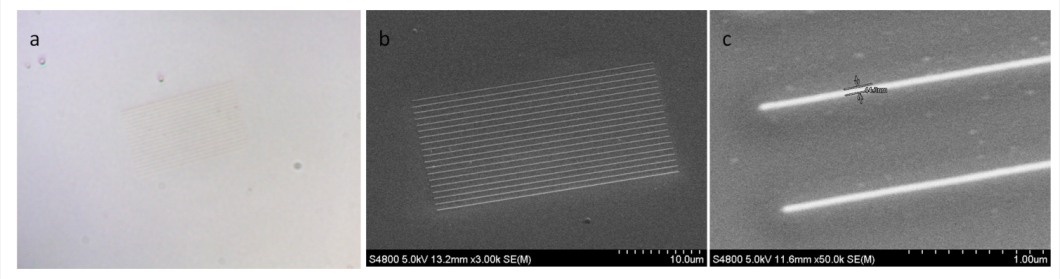

Figure 5.20 – Figure (a) is an optical microscope image taken at 100x magnification of a 20 by 30 μm periodic grating with 1 μm peridoicity, made from EBID tungsten material. (b) Shows an SEM image of the same grating and (c) contains a detail of the grating, with measured width of the deposited tungsten grating line around 40 nm.

In order to locate the small structures and aid their alignment with the laser in the Fourier setup, a scratch pattern was applied to the silicon surface to provide identifying marks on the sample substrate. The EBID-written patterns were placed in close proximity to one of the scratches to facilitate determining their location visually. However, the structures needed to be placed sufficiently far away from the scratches in order to avoid diffraction and scattering effects from these scratches, as those effects would overpower any patterns occuring as a result of the significantly smaller EBID structures. The placement of the structures relative to the scratches proved problematic as a misalignment caused by misinterpretation of the system parameters, as set out below, resulted in the actual patterns being written in a different location than originally intended.

In a GDSII file [145] for a 100 μm write field, the structures are usually placed in the bottom left

corner at coordinate (0,0), but when positioning the GDSII file in a positionlist based on coordinates, this system does not align the (0,0) coordinate of the GDSII file with the instructed set of coordinates, but instead places the centre of the write field at the instructed location. For a 100 μm write field this confusion between the bottom left corner and centre of the write field causes a (50 μm, 50 μm) misalignment downward and to the left. Because the size of the written structures was considerably smaller than half of the writefield size, this caused several samples to fail as the structures could at first not be located in their expected position, and several of the samples ended up with patterns being written to close to or on top of one of the scratches applied to the substrate for alignment purposes, as illustrates in figure 5.21.

In the end, to facilitate the detection of a Fourier response from structures written using EBID, their height was increased in an attempt to increase the efficiency in which they interact with light. The design was simplified so that the total area covered by the written structures could be increased to improve the chances to align the laser beam with the pattern.

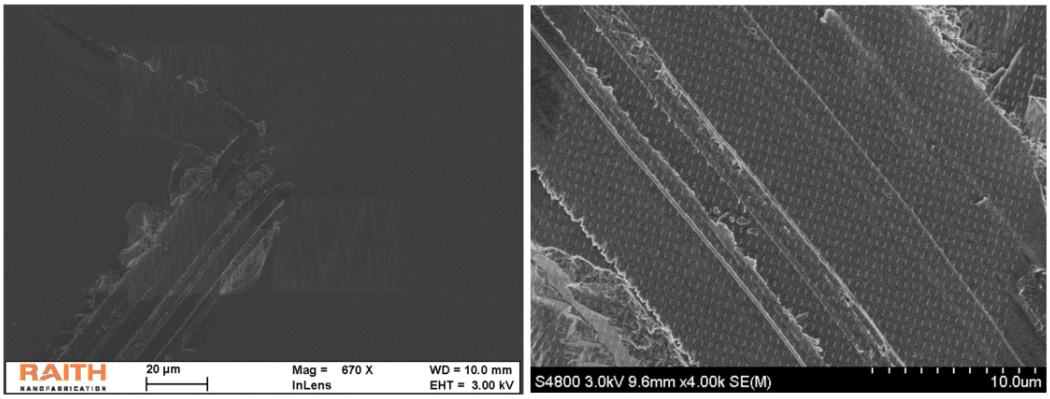

Figure 5.21 – Misalignment of the nanoantenna patterns onto a sample due to 50 μm positionlist alignment shift. The lefthand subfigure shows an e-beam SEM image of three nanoantenna arrays positioned on a scratch, and the righthand image shows a close-up SEM image of the nanoantennas on the scratch.

When scanning the sample surface of the 2D array of 3D columns (see figure 5.14) with the Fourier setup, the image shown in figure 5.22 was recorded. When comparing this image to the results presented in the 2006 paper by Van Dorp et al. in the Journal of Microscopy of electron diffraction patterns by nanoscale EBID $W(CO_6)$ material dot arrays, the patterns are similar. This suggests that the EBID tungsten pattern might have been detected using the Fourier microscopy setup.

5.2.6 Additional notes on EBID

During the project, a step-by-step manual was developed to operate the GIS equipment to perform electron-beam induced deposition, but the processes and menu settings are still in need of further development. Two specific examples of unexplained occurences during the writing process are discussed below.

A first example of unexplained GIS writing phenomena is illustrated in figure 5.23: during the fab-

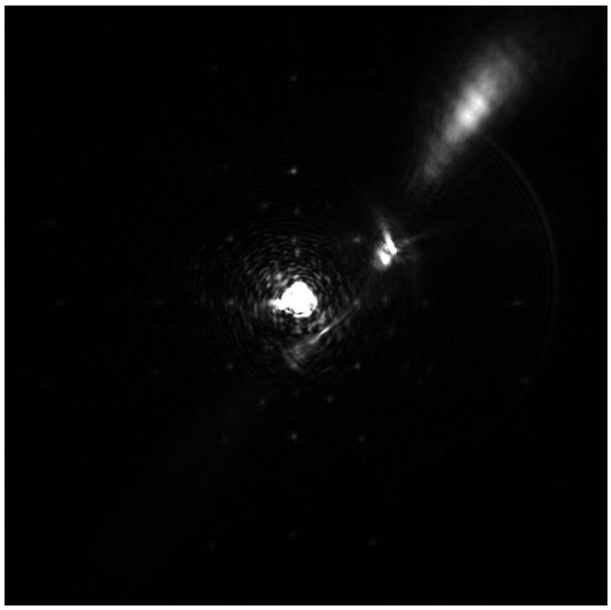

Figure 5.22 – A Fourier image taken during the scan of a silicon sample carrying a 2D dot array of tungsten 3D columns.

rication of the tungsten EBID samples, an undesirable drift was often noticed when writing larger patterns. The drift was not consistent in its direction or the extent of the effect. It is not understood what is causing these drifts, and if it is caused by the user-selected parameter and/or alignment settings, or if it is caused by an issue in the system itself.

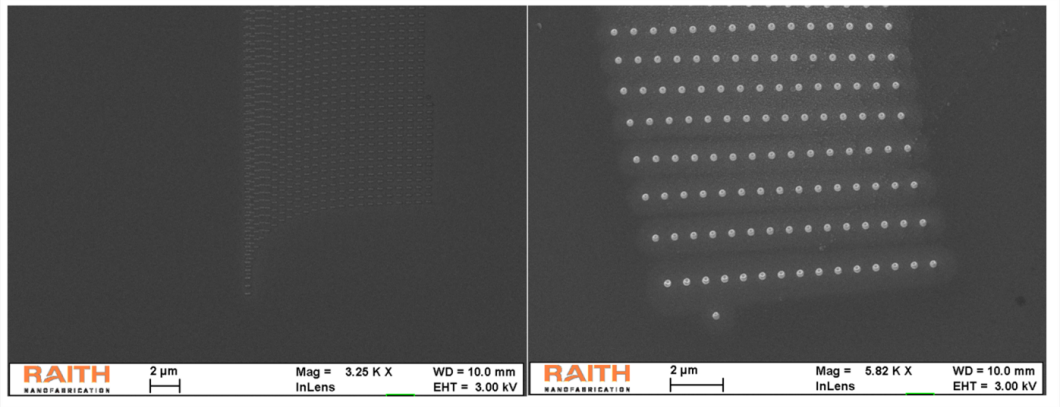

Figure 5.23 – Illustrations of drift issues experienced during longer writing times. The left picture shows the steep and sudden upward drift of what was intended to be a rectangular nanoantenna array. The right picture shows a slight drift to the right at the end of a write of a rectangualr array 2D columns.

Another undesirable effect observed during the fabrication of EBID samples was the deposition of a layer of material around areas with large amounts of deposited material (see figure 5.24), which suggests it is a side effect present during all depositions, but made more prominent due to the larger amount of deposited patterned material. It would be interesting to find out which settings are causing this excess deposition, if changes in parameter settings can decrease the deposition, and if this is the case, what these settings are.

Next to further developing the methods and understanding of the fabrication procedure, a better

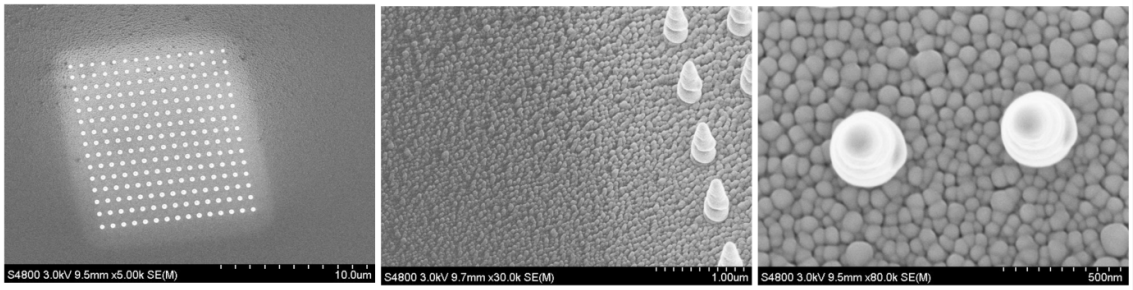

Figure 5.24 – The figures show evidence of unwanted deposition around areas where patterns were written. The light area around the column array has been covered in a layer of unwanted deposited material. The other two images show close-up SEM images of the accidentally deposited layer.

and more tailored measurement setup needs to be developed to characterise the samples. In a first part of future work, an optical response of GIS-written structures should be confirmed, potentially by changing the Fourier setup to be more accommodating to the smaller structures. Once this has been achieved, designs should be fabricated to confirm if plasmonic effects are present (e.g. by detecting Wood's anomalies [156]), and the efficiency of the deposited tungsten material as a plasmonic material should be quantified.

Chapter 6

Conclusion

In the field of nanophotonics research, the scaling down of optical devices has been a key objective. With their ability to arbitrarily control light beyond the diffraction limit using nanoscale structures, plasmonics are a valid and logical candidate to attain this size reduction. The promise of exceptional results and widespread applications has attracted growing research efforts, resulting in a steady increase in publications in the fields of nanoplasmonics and metamaterials since the 1990s. As research has advanced, a more realistic view on the potential applicability of nanoplasmonics has emerged, with a better understanding on feasible applications and unavoidable limitations of plasmonic performance. New fabrication techniques and plasmonic materials are being explored with the intention to tailor them to specific applications and manage their intrinsic limitations.

The aim of this thesis was to investigate the design, fabrication, and characterisation of nanoplasmonic samples made using Electron Beam Lithography (EBL) and Electron Beam Induced Deposition (EBID), and to compare the two processes and resulting features. The use of the EBL system came with all the benefits of a mature technology, with a solid understanding of the meaning of different parameter settings and a lot of prior practical experience of using the system available in the research group. The experience with using the system meant that recipes for plasmonic designs could be started from a basic set of parameters delivering a good starting point, and the understanding of the effect of different parameters meant that the optimisation of recipe settings could be performed in a targeted and efficient way. In contrast to EBL, the use of the gas injection system for electron-beam induced deposition of metal patterns came with the drawback of not having access to experience or understanding of the process, or a conclusive body of literature detailing the significance of paramater settings. However, EBID offers elegant and simple solutions to problems which for top-down etch-back EBL techniques would have been almost insurmountible. Point-and-shoot direct writing on sample surfaces, and the resulting possibility of precise alignment and custom design tailored to arbitrary patterns on a substrate are actions EBL could not perform. The possibility to write three-dimensional and greyscale patterns is also a strong advantage of EBID over EBL. Three-dimensional structures and alignment of patterns on arbitrarily placed collapsed and standing nanowires were presented.

It is important to note that EBL and EBID are not intended to be competing fabrication techniques, as EBID delivers a single-step nanoscale pattern in a chosen material, whereas EBL only delivers the nanolithographic patterning step of a muli-step fabrication process. The comparison between EBL

and EBID is should therefore not be made of the finished products, but of their ability to deliver nanoscale structures. Each of the two technologies has its own strengths and weaknesses, with EBL and the other steps in that nanofabrication process delivering high-quality products, and EBID enabling to fabricate structures that would be challenging or impossible to make using EBL. EBID is therefore a desirable fabrication technique for structures EBL cannot deliver, including greyscale and 3D patterning, and on-sample nanoscale alignment.

As a design taken through the development, fabrication, and characterisation steps to compare the two methods, chirped gratings were shown to be a discrete and planar alternative to blazed diffraction gratings. The linear momentum change associated with the optical path length difference induced by triangular blazed gratings was shown to be achieved by linearly varying the inverse of the grating period $\frac{1}{d}$. Simulations were developed using Comsol [152] and Matlab [153] to interrogate the influence of several design parameters including fill-factor, chirp, base period, etc. on the performance of the chirped diffraction grating. A fabrication recipe for gold chirped gratings on SU8 flexible membranes was developed for electron beam lithography, and the performance of the resulting samples was investigated using a Fourier Microscopy setup imaging the far-field diffraction patterns. Chirped grating far-field diffraction patterns were successfully observed using the Fourier microscopy setup, although their diffraction efficiency was considerably lower than that of a dielectric periodic grating used for calibration of the setup. It was found that EBID structures were not straightforward to detect using the same Fourier setup, and a series of EBID patterns were written covering a larger area in an attempt to observe an optical response. A diffraction pattern resulting from a two-dimensional tungsten dot array was potentially detected using the Fourier microscope in reflection, but the result was not conclusive.

Although the theoretical advantages and benefits of EBID over traditional EBL are clear, in experimental results, EBID structures did not elicit a significant optical response, and further research will be needed to optimise their material quality and performance. When patterns can be produced using EBL fabrication techniques, the EBID samples of this thesis could not compete with their EBL counterparts, but for cases beyond predictable alignment and planar features, alternatives to EBL are necessary. Further development of EBID technology and patterning settings will be required to let the fabrication possibilities live up to their potential for optical applications.

Chapter 7

Appendices

7.1 Appendix 1: E-Line GIS Practical User Guide

A. Setup

- Start the Elphy program as a GIS/Nanomanipulator User
- Load the sample into the machine on the Ultra-Flat Stage
- Check whether the GIS nozzles and nanomanipulators are parked (their circles should be blue, if they are red or grey they are not correctly initialised)
  You will not be able to drive the nozzles down if the Nanomanipulators or GIS nozzles are not initialised, so make sure to check this
  - If they are NOT initialised, drive the stage down to z = 1 mm manually and start the initialisation procedure (you might need to do this as admin). The initialisation can be found by clicking the button icon with a ruler icon at the top left of the GIS and Nanomanipulator menus
  - If this also fails, log in as admin and check whetehr the Nanomanipulators or GIS nozzles are LOCKED. If they are, unlock them.
- Once everything is correctly initialised, turn on the nozzle heaters
- Select the write settings: Aperture 30 μm, EHT 3 kV, WD 10 mm
- Drive the stage to z = 25.5 mm
- Measure the Faraday Cup current (USB TV needs to beturned off for this to succeed)
- Adjust origin, angle correction, focus, aperture, and stigmation alignment settings
- Set WD to exactly 10 mm (to 1 μm precision at least)
  This is an iterative procedure as follows:
  Start at z = 25.5 mm
  Repeat:
  - Focus on sample
  - Read WD (in the 'read W' menu box) and adjust W (disable the 'read from CCD' option)

  - Drive to W = 10.000 mm
- Once this is done, SAVE your settings into your preselected mode
- Start the OUTGAS procedure (EHT needs to be turned off to read the pressure inside the chamber.) This can bedone before the nozzles are driven down
  - The system vacuum should be below $1e^{-5}$ mbar, ideally around 3 e^{-6} mbar
  - Turn off EHT
  - Monitor the pressure using the Gun Monitor Program
  - Use outgas ON times of 0.3 s, 0.5 s, and 0.7 s
- Drive Nozzle in
- Load the Nozzle in second preselected Mode

Writing Structures in GIS

1. Writing Ad Hoc

- Open a single image (e-Line will go into patterning mode), there is an icon on the task bar of a new window with a + sign next to it
- Use ALT + DRAG to drag the GDSII file into the window. This will also open the drawing tools section in the toolbox
- Drag the recipe (e.g. Tungsten Line No Loops) onto the desired structure or use A to change the patterning attributes (= recipe settings) of the selected structure
- Make sure to adjust the recipe's system settings (e.g beam current)

2. Writing Using Positionlists

- Use macros to open/close valves at the start/end if positionlist
- For 3D writing, use macros to read the initial working distance (WD) and to change it (1 mum decrease in WD per layer suggested by Raith in test write)
- To set the recipes for the different structures:
  - Go to the desired GDSII file, click EDIT
  - Select the relevant structure(s)
  - Press A to make the patterning attributes menu appear and select DEPOSITION
  - Click SAVE

3. Setting Recipe Values

- Load the correct current by selecting that option and clicking OK
  do not click the pipette icon, it will drive to the Faraday Cup without moving the nozzles to PARK position, and could cause damage
- Select the type of exposure in the dropdown menu
- Set general recipe parameters (step size, line spacing, loops, ...) Smaller step/line spacing sizes increase the amount of deposition in that location, as do more loops

- For each style of deposition (Area, Single Pixel Line, Dot) set dwell time, dose, and select deposition specific requirements (e.g. direction and shape of pattern drawing)

References

[1] *The British Museum*, Collection Online: the Lycurgus Cup, [Online] Available: $http://www.britishmuseum.org/research/collection\_online/collection\_object\_details.aspx?objectId = 61219\&partId = 1\&searchText = lycurgus + cup$ [Accessed February 2017]

[2] *The British Museum*, Sutton Hoo and Europe AD 300 - 1100, Room 41, the Sir Paul and Lady Ruddock Gallery [Online] Available: $http://www.britishmuseum.org/visiting/galleries/europe/room\_41\_europe\_ad\_300-1100.aspx$ [Accessed February 2017]

[3] I. Freestone, N. Meeks, M. Sax, C. Higgitt. The Lycurgus Cup - A Roman Nanotechnology, *Gold Bulletin*, 40(4), pp. 270 - 277, 2007.

[4] D. Pile. Perspective on PLasmonics, Interview with Joachim Krenn, *Nature Photonics*, 6, 2012

[5] A. I. Fernández-Domínguez, F. J. García-Vidal, L. Martín-Moreno. Unrelenting Plasmons, *Nature Photonics*, 11, pp. 8 - 10, January 2017.

[6] W. L. Barnes, A. Dereux, T. W. Ebbesen. Surface Plasmon Subwavelength Optics, *Nature*, 424, 2003.

[7] J. A. Schuller, E. S. Barnard, W. Cai, Y. Chul Jun, J. S. White, M. L. Brongersma. Plasmonics for Extreme Light Concentration and Manipulation, *Nature Materials*, 9, 2010.

[8] N. Meinzer, W. L. Barnes, I. R. Hooper. Plasmonic Meta-Atoms and Metasurfaces, *Nature Photonics*, 8, 2014.

[9] Y. Li, S. Kita, P. Muñoz, O. reshef, D. I. Vulis, M. Yin, M. Loncar, E. Mazur. On-chip Zero-Index Metamaterials, *Nature Photonics*, 9, 2015.

[10] K. M. Mayer, J. H. Hafner. Localised Surface Plasmon Resonance Sensors, *Chemical Reviews*, 1(11), pp. 3828 - 3857, 2011.

[11] A. G. Brolo. Plasmonics for Future Biosensors, *Nature Photonics*, 6, 2012.

[12] C. S. Moreira, A.M.N. Lima, H. Heff, C. Thirstrup. Temperature-Dependent Sensitivity of Surface Plasmon Resonance Sensors at the Gold-Water Interface, *Sensors and Actuators B*, 134, pp. 854 - 862, 2008.

[13] A. El Eter, N. M. Hameed, F. I. Baida, R. Salut, C. Filiatre, D. Nedeljkovic, E. Atie, S. Bole, T. Grosjean. Fiber-Integrated Optical Nano-Tweezer Based on a Bowtie-Aperture Nano-antenna at the Apex of a SNOM Tip, *Optics Express*, 22(8), 2014.

[14] C. L. Nehl, H. Liao, J. H. Hafner. Optical Properties of Star-Shaped Gold Nanoparticles, *Nano Letters*, 6(4), pp. 683 - 688, 2006.

[15] V. G. Veselago. The Electrodynamics of Substances with Simultaneously Negative Values of ϵ and μ, *Sov. Phys. Usp.*, 10 509, 1968.

[16] D. R. Smith, J. B. Pendry, M. C. K. Wiltshire. Metamaterials and Negative Refractive Index, *Science*, 305, 2004.

[17] Nhs.uk. Endoscopy, 11 October 2016 [Online] Available: $http://www.nhs.uk/Conditions/Endoscopy/Pages/Introduction.aspx$. [Accessed January 2017]

[18] B. E. A. Saleh, M. V. Teich. Fundamentals of Photonics, *John Wiley and Sons*, New York, 1991.

[19] D. Van Thourhout, R. Baets, H. Ottevaere. Microphotonics syllabus, *Ghent University, VUB*, academic year 2012 - 2013.

[20] S. A. Maier. Plasmonics: Fundamentals and Applications. *Springer*, 2007.

[21] P. Tassin, T. Koschny, M. Kafesaki, C. M. Soukoulis. A Comparison of Graphene, Superconductors and Metals as Conductors for Metamaterials and Plasmonics, *Nature Photonics*, 6, 2012.

[22] M. Abb, P. Albella, J. Aizpurua, O. L. Muskens. All-Optical Control of a Single Plasmonic Nanoantenna-ITO Hybrid, *Nano Letters*, 11(6), pp. 2457 - 63, 2011.

[23] M. Abb, B. Sepúlveda, H. M. H. Chong, O. L. Muskens. Transparent Conductive Oxides for Active Hybrid Metamaterial Devices, emphJournal of Optics, 14(11), 2012.

[24] V. G. Kravets, F. Schedin, A. N. Grigorenko. Extremely Narrow Plasmon Resonances Based on Diffraction Coupling of Localized Plasmons in Arrays of Metallic Nanoparticles, *Physical Review Letters*, 101, 2008.

[25] J. B. Khurgin. How to deal with the Loss on Plasmonics and Metamaterials, *Nature Nanotechnology*, 10, 2015.

[26] J. B. Khurgin, A. Boltasseva, Reflecting upon the losses in Plasmonics and Metamaterials, *MRS Bulletin* 37, pp. 768 - 779, 2012.

[27] B. J. Roxworthy, K. D. Ko, A. Kumar, K. Hung Fung, E. K. C. Chow, G. L. Liu, N. X. Fang, K. C. Toussaint Jr. Application of Plasmonic Bowtie Nanoantenna Arrays for Optical Trapping, Stacking, and Sorting, *Nano Letters*, 12, pp. 796 - 801, 2012.

[28] A. Krasavin, A. V. Zayats. Guiding Light at the Nanoscale: Numerical Optimization of Ultrasubwavelength Metallic Wire Plasmonic Waveguides, *Optics Letters*, 36(16), pp. 3127 - 3129, 2011.

[29] M. Kauranen, A. V. Zayats. Nonlinear Plasmonics, *Nature Photonics*, 6, pp. 737 - 748, 2012.

[30] G. A. Wurtz, R. Pollard, W. Hendren, G. P. Wiederrecht, D. J. Gosztola, V. A. Podolskiy, A.V. Zayats. Designed Ultrafast Optical Nonlinearity in a Plasmonic Nanorod Metamaterial Enhanced by Nonlocality, *Nature Nanotechnology*, 6, pp. 107 - 111, 2011.

[31] G. Baffou, R. Quidant, C. Girard. Heat Generation in Plasmonic Nanostructures: Influence of Morphology, *Applied Physics Letters*, 94, 2009.

[32] Commercialising Plasmonics, *Nature Plasmonics*, 9(477), 2015.

[33] K. Kneipp. Surface Enhanced Raman Scattering, *Physics Today*, pp. 40 - 46, 2007.

[34] A. C. De Luca, P. Reader-Harris, M. Mazilu, S. Marriggìo, D. Corda, A. Di Falco. Reproducible Surface-Enhanced Raman Quantification of Biomarkers in Multicomponent Mixtures, *ACS Nano*, 8(3), pp. 2575 - 2583, 2014.

[35] A. Aubry, D. Y. Lei, A. I. Fernández-Dominguez, Y. Sonnefraud, S. A. Maier, and J. B. Pendry. Plasmonic Light-Harvesting Devices over the Whole Visible Spectrum, *Nano Letters*, 10, pp. 2574 - 2579, 2010.

[36] M. Lee, J. U. Kim, K. J. Lee, S. Ahn, Y.-B. Shin, J. Shin, C. B. Park. Aluminum Nanoarrays for Plasmon-Enhanced Light Harvesting, *ACS Nano*, 9(6), pp. 6206 - 6213, 2015.

[37] A. K. K. Kyaw, D. H. Wang, D. Wynands, J. Zhang, T.-Q. Nguyen, G. C. Bazan, A. J. Heeger. Improved Light Harvesting and Improved Efficiency by Insertion of an Optical Spacer (ZnO) in Solution-Processed Small-Molecule Solar Cells, *Nano Letters*, 13, pp. 3796 - 3801, 2013.

[38] J. B. Pendry, A. J. Holden, D. J. Robbins, W. J. Stewart. Magnetism from Conductors and Enhanced Nonlinear Phenomena, *IEEE Transactions on Microwave Theory and Techniques*, 47(11), pp. 2075 - 2084, 1999.

[39] C. Soukoulis, M. Wegener. Past Achievements and Future Challenges in the Development of Three-Dimensional Photonic Metamaterials. *Nature Photonics*, 5, pp523 - 530, 2011.

[40] N. Zheludev. The Road agead for Metamaterials, *Science*, 328, 5978, pp. 582 - 583, 2010.

[41] P. R. West, S. Ishii, G. Naik, N. Emani, V. M. Shalaev, A. Boltasseva. Searching for Better Plasmonic Materials, *Laser and Photonics Reviews*, 4(6), pp. 795 - 808, 2010.

[42] A. M. Shaltout, A. V. Kildishev, V. S. Shalaev. Evolution of Photonic Metasurfaces: From Static to Dynamic, *Journal of the Optical Society of America B*, 33(3), pp. 501 - 510, 2016.

[43] C. L. Holloway, A. Dienstfrey, E. F. Kuester, J. F. O'Hara, A. K. Azad and A. J. Taylor. A Discussion on the Interpretation and Characterization of Metafilms/Metasurfaces: the Twodimensional Equivalent of Metamaterials, *Metamaterials*, 3(2), pp. 100 - 112, 2009

[44] T. Ergin, N. Stenger, P. Brenner, J. B. Pendry, M. Wegener. Three-dimensional Invisibility Cloak at Optical Wavelengths, *Science*, 328, pp. 337 - 339, 2007.

[45] N. Yu, F. Capasso. Flat Optics with Designer Metasurfaces, *Nature*, 13, 2014.

[46] H. Fischer, O. J. F. Martin. Engineering the Optical Response of Plasmonic Nanoantennas, *Optics Express*, 16, 12, 2008.

[47] P. Reader-Harris, A. Di Falco. Nanoplasmonic Filters for Hollow-Core Photonic Crystal Fibres, *ACS Photonics*, 1(10), pp. 985 - 989, 2014.

[48] N. Yu, P. Genevet, M. A. Kats, F. Aieta, J.-P. Tetienne, F. Capasso, Z. Gaburro. Light Propagation with Phase Discontinuitues: Generalised Laws of Reflection and Refraction, *Science*, 334, pp. 333 - 337, 2011.

[49] F. Qin, L. Ding, L. Zhang, F. Monticone, C. C. Chum, J. Deng, S. Mei, Y. Li, J. Teng, M. Hong, S. Zhang, A. Alù, C.-W. Q. Hybrid Bilayer Plasmonic Metasurface Efficiently Manipulates Visible Light, *Science Advances*, 2, 2016.

[50] M. Khorasaninejad, F. Capasso. Broadband Multifunctional Efficient Meta-Gratings Based on Dielectric Waveguide Phase Shifters, *Nano Letters*, 15(10), 2015.

[51] Y. Zhang, L. Zhou, J. Li, Q. Wang, C. Huang. Ultra-Broadband and Strongly Enhanced Diffraction with Metasurfaces, *Scientific Reports*, 5, 2015.

[52] L. Chen, G. P. Wang, Q. Gan,F. J. Bartoli. Rainbow trapping and releasing by chirped plasmonic waveguides at visible frequencies, *Applied Physics Letters*, 97(15), 2010.

[53] Q. Gan, F. J. Bartoli. Surface dispersion engineering of planar plasmonic chirped grating for complete visible rainbow trapping, *Applied Physics Letters*, 98, 2011.

[54] J.-S. Bouillard, S. Vilain, W. Dickson, G.A. Wurtz, A. V. Zayats. Broadband and Broadangle SPP antennas based on Plasmonic Crystals with Linear Chirp, *Scientific Reports*, 2, 2012.

[55] N. I. Zheludev, E. Plum. Reconfigurable Nanomechanical Photonic Metamaterials, *Nature Nanotechnology*, 11, 2016.

[56] P. Ruchhoeft, M. Colburn, B. Choi, H. Nounu, S. Johnson, T. Bailey, S. Damle, M. Stewart, J. Ekerdt, S. V. Sreenivasan, J. C. Wolfe and C. G. Willson. Patterning Curved Surfaces: Template Generation by Ion Beam Proximity Lithography and Relief Transfer by Step and Flash Imprint Lithography, *Journal of Vacuum Science Technology B: Microelectronic and Nanometer Structures Processing*, 17(6), pp. 2965 - 2969, 1999.

[57] A. Nathan, A. Ahnood, M. T. Cole, S. Lee, Y. Suzuki, P. Hiralal, F. Bonaccorso, T. Hasan, L. Garcia-Gancedo, A. Dyadyusha, S. Haque, P. Andrew, S. Hofmann, J. Moultrie, D. Chu, A. J. Flewitt, A. C. Ferrari, M. J. Kelly, J. Robertson, G. A. J. Amaratunga and W. I. Milne. Flexible electronics: the next ubiquitous platform, *Proc. IEEE*, 100, pp. 1486 - 1517, 2012.

[58] P. Reader-Harris, A. Ricciardi, T. Krauss, A. Di Falco. Optical Guided Mode Resonance Filter on a Flexible Substrate, *Optics Express*, 21(1), 2013.

[59] S. Aksu, M. Huang, A. Artar, A. A. Yanik, S. Selvarasah, M. R. Dokmeci and H. Altug. Flexible Plasmonics on Unconventional and Nonplanar Substrates, *Advanced Materials*, 23(38), pp. 4422 - 4430, 2011.

[60] R. M. Cole, S. Mahajan and J. J. Baumberg. Stretchable Metal-Elastomer Nanovoids for Tunable Plasmons, Applied Physics Letters, 95(15), 2010.

[61] I. M. Pryce, K. Aydin, Y. A. Kelaita, R. M. Briggs and H. A. Atwater. Highly Strained Compliant Optical Metamaterials with Large Frequency Tunability, *Nano Letters*, 10(10), pp. 4222 - 4227, 2010.

[62] Where Now For Plasmonics, *Nature Nanotechnology*, 11, 2016.

[63] S. Janahi, Z. Jacob. All-dielectric Metamaterials, *Nature Nanotechnology*, 11, 2016.

[64] U. Guler, A. V. Kildichev, AA. Boltasseva, V. M. Shalaev. Plasmonics on the Slope of Enlightenment: the Role of Transition Metal Nitrides, *Faraday Discussions*, 178(71), 2015.

[65] U. Guler, V. M. Shalaev, A. Boltasseva. Nanoparticle Plasmonics: Going Practical with Transistion Metal Nitrides, *Materials Today*, 18(4), 2015.

[66] N. Kinsey, M. Ferrera, V. M. Shalaev, A. Boltasseva. Examining Nanophotonics for integrated hybrid systems: a review of plasmonic interconnects and modulators using traditional and alternative materials, *Journal of the Optical Society of America B*, 32(1), pp. 121 - 142, 2015.

[67] G. V. Naik, V. M. Shalaev, A. Boltasseva. Alternative Plasmonic Materials: Beyond Gold and Silver, *Advanced Materials*, 25, pp. 3264 - 3294, 2013.

[68] A. Boltasseva, H. A. Atwater. Low-Loss Plasmonic Metamaterials, *Science*, 331, pp. 290 - 291, 2011.

[69] M. Riordan, L. Hoddeson, C. Herring. The Invention of the Transistor, *Reviews of Modern Physics*, 71(2), Centenary 1999.

[70] T. Love. Object Lessons: Lessons Learned in Object-Oriented Development Projects, *Cambridge University Press*, Cambridge, 1997.

[71] L. F. Thompson. Introduction to Lithogtaphy, ACS Publications,pp. 1 - 13, 1983.

[72] J. S. Kilby. Invention of the Inegrated Circuit, *IEEE Transactions on Electronic Devices*, 23(7), 1976.

[73] R. N. Noyce. Semiconductor Device-and-Lead Structure, US2981877A *Fairchild Semiconductor*, 1961.

[74] G. E. Moore. Cramming More Components Onto Integrated Circuits, *Electronics*, 38(8), 1965.

[75] R. Courtland. Moore's law's Next Step: 10 Nanometers, *IEEE Spectrum*, 54(1), pp. 52-53, 2017.

[76] K. M. Poole, Electrode Contamination in Electron Optical Systems, *Proceedings of the Physcical Society B*, 66(7), 1953.

[77] A. Ashkin. Electron Beam Analyzer, *Journal of Applied Physics B* 28, 1957.

[78] M. A. McCord, M. J. Rooks. SPIE Handbook of Microlithography, Micromachining, and Microfabrication, Volume 1, Chapter 2, *SPIE*, 1997.

[79] M. Hatzakis. Electron Resists for Microcircuit and Mask Production, *J. Electrochem. Soc.* 116, pp. 1033-1037, 1969.

[80] World Semiconductor Trade Statistics [Online] Available: *https://www.wsts.org/* . [Accessed June 2017]

[81] R. W. Christy. Formation of Thin Polymer Films by Electron Bombardment, *Journal of Applied Physics*, 31, pp. 1680, 1960.

[82] M. Toth, C. lobo, V. Friedli, A. Szkudlarek, I. Utke. Continuum Models of Focused Electron Beam Induced Processing, *Beilstein Journal of Nanotechnology*, 6, pp. 1518 - 1540, 2015.

[83] P. Wilhite, A. A. Vyas, Jason Tan, Jasper Tan, T. Yamada, P. Wang, J. Park, C. Yang. Metal-Nanocarbon Contacts, *Semiconductor Science and Technology*, 29, 2014.

[84] G. Rius. Technology Basis and Perspectives on Focused Electron Beam Induced Deposition and Focused Ion Beam Induced Deposition, *Nuclear Instruments and Methods in Physics Research B*, 314, pp. 337 - 43, 2014.

[85] P. Wilhite, H. S. Uh, N. Kanzaki, P. Wang, A. Vyas, S. Maeda, T. Yamada, C. Yang. Electron-Beam and Ion-Beam induced Deposition Yungsten Contacts for Carbon Nanofibre Interconnects, *Nanotechnology*, 25, 2014.

[86] G. L. Kerr, V. Stoljan, S. r. P. Silva. Characterisation of Electron-Beam Deposited Tungsten Interconnects, *Journal of Physics: Conference Series: Electron Microscopy and Analysis Group Conference*, 126, 2007.

[87] K. Wnorowski, M. Stano, C.Matias, S. Denifl, W. Barszczewska, S. Matejcík. Low-Energy Electron Interactions with Tungsten Hexacarbonyl - ($W(CO)_6$), *Rapid Communic. Mass Spectrom.*, 26, pp. 2093 - 2098, 2012.

[88] W. F. van Dorp, B. van Someren, C. W. Hagen, P. Kruit. Approaching the Resolution Limit of Nanometre-scale Electron Beam Induced Deposition, *Nano Letter*, 2(7), pp. 1303 - 1307, 2005.

[89] A. Botman, J. J. L. Mulders, C. W. Hagen. Creating Pure Nanostructures from Electron-Beam-Induced Deposition Using Purification Techniques: a Technology Perspective, *Nanotechnology*, 20, 2009.

[90] I. Utke, P. Hoffman, J. Melngaillis. Gas-assisted Focused Electron Beam and Ion Beam Processing and Fabrication, *Journal of Vacuum Science Technology B*, 26(4), 2009.

[91] H. H. Rose. Optics of High-Performance Electron Microscopes, *Science and Technology of Advanced Materials*, 9(1), 2008.

[92] Y. Chen. Nanofabrication by Electron Beam Lithography and its Applications: A Review, *Microelectronic Engineering*, 135, pp. 57 - 72, 2015.

[93] A. N. Broers, A. C. F. Hoole, J. M. Ryan. Electron Beam Lithography - Resolution Limits, *Microelectronic Engineering*, 32, pp. 131 -142, 1996.

[94] C. Vieu, F. Carcenac, A. Pépin, Y. Chen, M. Mejias, L. Manin-Ferlazzo, L. Couraud, H. Launois. Electron Beam Lithography: Resolution Limits and Applications, *Applied Surface Science*, 164, pp. 111 - 117, 2000.

[95] A. E. Grigorescu, C. W. Hagen. Resists for Sub-20-nm Electron Beam Lithography with a Focus on HSQ: State of the Art, *Nanotechnology*, 20, 2009.

[96] M. Rommel, B. Nilsson, P. Jedrasik, V. Bonanni, A. Dmitriev, J. Weis. Sub-10 nm Resolution After Lift-off Using HSQ/PMMA Double Layer resist, *Microelectronics Engineering*, 110, pp. 123 - 125, 2013.

[97] A. Del Campo, C. Greiner. SU-8: A Photoresist for High-Aspect-Ratio and 3D Submicron Lithography, *Journal of Micromechanics and Microengineering*, 17(6), pp. 81 - 95, 2007.

[98] H. W. P. Koops, J. Kretz, M. Rudolph, M. Weber, G. Dahm, K. L. Lee. Characterisation oand Application of Materials Grown by Electron-Beam-Induced Deposition, *Japanese Journal of Applied Physics*, 33(1), 1994.

[99] A. Fernández-Pacheco, L. Serrano-Ramón, J. M. Michalik, M. R. Ibarra, J. M. De Teresa, L. O'Brien, D. Petit, J. Lee, R. P. Cowburn. Three Dimensional Magnetic Nanowires Grown by Focused Electron-Beam Induced Deposition, *Scientific Reports*, 3, 2013.

[100] W. F. van Dorp, C. W. Hagen. A Critical Review Of Focused Electron Beam Induced Deposition, *Journal of Applied Physics*, 104, 2008.

[101] J. D. Fowlkes, S. J. Randolph, P.D. Rack. Growth and Simulation of High-Aspect Ratio Nanopillars by Pirmary and Secondary Electron-Induced Deposition, *Journal of Vacuum Science Technology B*, 23(6), pp. 2825 - 2831, 2005.

[102] P. C. Hoyle, M. Ogasawara, J. R. A. Cleaver, H. Ahmed. Electrical Resistance of Electron Beam Induced Deposits from Tungsten Hexacarbonyl, *Applied Physics Letters*, 62, 1993.

[103] M. Takeguchi, M. Shimojo, K. Fuyura. Nanostructure Fabrication by Electron-Beam-Induced Deposition with Metal Carbonyl Precursor and Water Vapor, *Japanese Journal of Applied Physics*, 46(1), 2007.

[104] J. D. Fowlkes, R. Winkler, B. B. Lewis, M. G. Stanford, H. Plank, P. D. Rack. Simulation-Guided 3D Manufacturing via Electron Beamm Induced Deposition, *ACS Nano*, 10, pp. 6163 - 6172, 2015.

[105] R. Córdoba, N. Sharma, S. Kölling, P. M. Koenraad, B. Koopmans. High-Purity 3D Nano-objects Grown by Focused-ElectronÂ°Beam Induced Deposition, *Nanotechnology*, 27, 2016.

[106] W. S. Chang, S. Bauerdick, M. S. Jeong. Resolution Enhancing Using Cantilevered Tip-On-Aperture Silicon Probe Near-field Optical Microscopy, *Ultramicroscopy*, 108(10), pp. 1070 - 1075, 2008.

[107] H. Morimoto, T. Kishimoto, M. Takai, S. Yura, A. Hosono, S. Okuda, S. Lipp, L. Frey. Electron-Beam-Induced Deposition of Pt for Field Emitter Arrays, *Japan Journal of Applied Physics*, 35, pp. 6623 - 6625, 1996.

[108] H. W. P. Koops, C. Schössler, A. Kaya, M. Weber. Conductive Dots, Wires, and Supertipes for Field Electron Emitters Produced by Electron-eam Induced Deposition on Samples having Increased Temperature, *Journal of Vacuum Science and Technology B*, 14(6), 1996.

[109] S. Graells, R. Alcubilla, G. Badenes, R. Quidant. Growth of Plasmonic Gold Nanostructures by Electron Beam Induced Deposition, *Applied Physics Letters*, 91, 2007.

[110] S. Sengupta, C. Li, C. Baumier, A. Kasumov, et al. Superconducting Nanowires by Electron-Beam-Induced Deposition, *Applied Physics Letters*, 106, 2015.

[111] C. W. Hagen. The Future of Focused Electron Beam-Induced Processing, *Applied Physics A*, 117, pp. 1599 - 1605, 2014.

[112] S. Hari, C. W. Hagen, t. Verduin, P. Kruit. Size and Shape Control of Sub-20 nm Patterns Fabricated Using Focused Electron Beam Induced Processing., *Proceedings of SPIE*, 9049, 2014.

[113] *Agar Scientific*, Square Coverglasses 20 x 20 m, Agar Scientific Ltd., 2017.
Available: $http://www.agarscientific.com/lm/coverglasses-coverslips/square-coverglasses-10473.html$

[114] *MicroChem*, *Omnicoat*^{TM}, MicroChem, Newton MA, accessed 2017.
Available: $http://microchem.com/pdf/OMNICOAT.pdf$

[115] *MicroChem*, SU-8 2000 Permanent Epoxy Negative Photoresist, MicroChem, Newton MA, accessed 2017.
Available: $http://www.microchem.com/pdf/SU-82000DataSheet2000_5thru2015Ver4.pdf$

[116] R. Martinez-Duarte, M. J. Madou. Microfluidics and Nanofluidics Handbook, Chapter 8: SU-8 Photolithography and its Impact on Microfluidics, *CRC Press*, pp. 321 - 268, 2010.

[117] *MicroChem*, SU-8 2000 Permanent Epoxy Negative Photoresist, MicroChem, Newton MA, accessed 2017.
Available: $http://www.microchem.com/pdf/SU-82000DataSheet2025thru2075Ver4.pdf$

[118] *Sigma Aldrich*, N-Methylpyrrolidone, Sigma Aldrich Co. LLC, 2017.
Available: $http://www.sigmaaldrich.com/catalog/product/aldrich/m79204?lang=en\&region=GB$

[119] *Shipley* MF-319 Developer, Shipley Europe Ltd., Coventry, 2017.
Available: $http://microchem.com/products/images/uploads/MF_319_DataSheet.pdf$

[120] K. M. McPeak, S. V. Jayanti, J. P. Kress, S. Meyer, S. Iotti, A. Rossinelli, D. J. Norris. Plasmonics Films Can Easily Be Better: Rules and Recipes, *ACS Photonics*, 2(3), pp. 326 - 333, 2015.

[121] G. R. Brewer. Electron-Beam Technology in Microelectronics Fabrication, *Academic Press*, New York, 1980.

[122] M. Altissimo. E-beam Lithography for Micro-Nanofabrication, *AIP Biomicrofluidics*, 4(2), 2010.

[123] A. Biswas, I. S. Bayer, A. S. Biris, T. Wang, E. Dervishi, F. Faupel. Advances in Top-Down and Bottom-Up Surface Nanofabrication: Techniques, Applications and Future Prospects, *Advances in Colloid and Interface Science*, 170, pp. 2 - 27, 2012.

[124] B. D. Gates, Q. Xu, M. Stewart, D. Ryan, C. G. Willson, G. M. Whitesides. New Approaches to Nanofabrication: Molding, Printing, and Other Techniques, *Chemical Reviews*, 105, pp. 1171 - 1196, 2005.

[125] S. Y. Chou, P. R. Krauss, P. J. Renstrom. Imprint Lithography with 25-Nanometer Resolution, *Science*, 272(5258), pp. 85 - 87, 1996.

[126] S. H. Ahn, L. J. Guo. Large-Area Roll-to-Roll and Roll-to-Plate Nanoimprint Lithography: A Step toward High-Throughput Application of Continuous Nanoimprinting, *ACS Nano*, 3(8), 2009.

[127] T. Betancourt, L. Brannon-Peppas. Micro- and Nanofabrication methods in Naotechnological Medical and Pharmaceutical Devices, *International Journal of Nanomedicine*, 1(4), pp. 483 - 495, 2006.

[128] Y. Xia, G. M. Whitesides. Soft Lithography, *Annual Review of Material Science*, 28, pp. 153 - 184, 1998.

[129] B. D. Gates, Q. Xu, J. C. Love, D. B. Wolfe, G. M. Whitesides. Unconventional Nanofabrication, *Annual Review of Materials Research*, 34, pp. 339 - 372, 2004.

[130] J. K. W. Yang, Y. S. Jung, J.-B. Chang, R. A. Mickiewicz, A. Alexander-Katz, C. A. Ross, K. K. Berggren. Complex Self-Assembled Patterns Using Sparse Commensurate Templates with Locally Varying Motifs, *Nature Nanotechnology*, 5, pp. 256 - 260, 2010.

[131] D. M. Eigler, E. K. Schweizer. Positioning Single Atoms with a Scanning Tunneling Microscope, *Nature*, 334, pp. 524 - 526, 1990.

[132] D. S. Ginger, H. Zhang, C. A. Mirkin. The Evolution of Dip-Pen Nanolithography, *Angewandte Chemie*, 43(1), pp. 30 - 45, 2003.

[133] T. A. Jung, A. Moser, H. J. Hug, D. Brodbeck, R. Hofer, H. R. Hidber, U. D. Schwarz. The Atomic Force Microscope User as a Powerful Tool for Machining Surfaces, *Ultramicroscopy*, 42-44(2), pp. 1446 - 1451, 1992.

[134] S. Gwo, C.-L. Yeh, P.-F. Chen, Y.-C. Chou, T. T. Chen. Local Electric-Field-Induced Oxidation of Titanium Nitride Films, *Applied Physics Letters*, 74(8), 1999.

[135] B. D. Gates, Q. Xu, V. R. Thalladi, T. Cao, T. Knickerbocker, G. M. Whitesides. Shear Patterning of Microdominos: A New Class of Procedures for Making Micro- and Nanostructures, *Angewandte Chemie*, 43(21), pp. 2780 - 2783, 2004.

[136] W. Geyer, V. Stadler, W. Eck, M. Zharkinov, A. Gölzhäuser, M. Grunze. Electron-Induced Crosslinking of Aromatic Self-Assembled Monolayers: Negative resists for Nanolithography, *Applied Physics Letters*, 75, 1999.

[137] Z. She, A. Di Falco, G. Hähner, M. Buck. Electron-Beam Patterned Self-Assembled Monolayers as Templates for Cu Electrodeposition and Liftoff, *Beilstein Journal of Nanotechnology*, 3, pp. 101 - 103, 2012.

[138] P. W. K. Rothemund. Folding DNA to Create Nanoscale Shapes and Patterns, *Nature*, 440, pp. 297 - 302, 2006.

[139] A. Kuzuya, M. Komiyama. DNA Origami: Fold, Stick, and Beyond, *Nanoscale*, 2, pp. 310 - 322, 2010.

[140] X. Shen, C. Song, J. Wang, D. Shi, Z. Wang, N. Liu, B. Ding. Rolling Up Gold Nanoparticle-Dressed DNA Origami into Three-Dimensional Plasmonic Chiral Nanostructures, *Journal of the American Chemical Society*, 134, pp. 146 - 149, 2012.

[141] F. N. Gür, F. W. Schwarz, J. Ye, S. Diez, T. L. Schmidt. Towards Self-Assembled Plasmonic Devices: High-Yield Arrangement of Gold Nanoparticles on DNA Origami Templates, *ACS Nano*, 10(5), pp. 5374 - 5382, 2016.

[142] M. Born, E. Wolf. Principles of Optics, Electromagnetic Theory of Propagation, Interference and Diffraction of Light, *Cambridge University Press*, Cambridge, New York, 1999.

[143] *eLINE PLUS*, Product Overview, Raith GmbH, 2017.
Available: *https://www.raith.com/products/eline-plus.html*.

[144] *NanoSuite Software Reference Manual*, Raith GmbH, 2014.

[145] M. A. McCord, M. J. Rooks. SPIE Handbook of Microlithography, Micromachining, and Microfabrication, Appendix: GDSII Stream Format, Volume 1, Chapter 2.9, *SPIE*, 1997.

[146] M. C. Hutley. Diffraction Gratings, *Academic Press*, London, 1982.

[147] I. Sersic, C. Tuambilangana, A. Femius Koenderink. Fourier Microscopy of Single Plasmonic Scatterers, *New Journal of Physics*, 13, 2011.

[148] J. W. Goodman. Introduction to Fourier Optics, 3rd edition, *Roberts and Company Publishers*, 2005.

[149] C. Hammond. A Symmetrical Representation of the Geometrical Optics of the Light Microscope. *Journal of Microscopy*, 192(1), pp. 63-68, 1998.

[150] C. Hammond, J. Heath. Symmetrical Ray Diagrams of the Optical Pathways in Light Microscopes. *Microscopy and Analysis*, 20(5), 2006.

[151] J. A. Kurvits, M. Jiang, R. Zia. Comparative Analysis of Imaging Configurations and Objectives for Fourier Microscopy. *Journal of the Optical Society of America A*, 32(11), pp. 2082-2092, 2015.

[152] *COMSOL Multiphysics*, overview, COMSOL Inc., 2017.
Available: https://www.comsol.com/comsol-multiphysics

[153] *Matlab*, The Language of Technical Computing, The Mathworks, Inc., 2017.
Available: *https://uk.mathworks.com/products/matlab.html*

[154] W. F. Van Dorp, B. van Someren. Diffraction patterns of Artificial Two-Dimensional Crystals Synthesized in Situ in an Environmental Scanning Transmission Microscope, *Journal of Microscopy*, 221, pp. 159 - 163, 2006.

[155] Y. Yu, X-M. Dou, B. Wei, G-W. Zha, X-J. Shang *et al.* Self-Assembled Quantum Dot Structures in a Hexagonal Nanowire for Quantum Photonics, *Advanced Materials*, 26, pp. 2710 - 2717, 2014.

[156] R. W. Wood. On a Remarkable Case of Uneven Distribution of Light in a Diffraction Grating Spectrum, *Proc. Phys. Soc. London*, 18, 269, 1902.

[157] A. Hessel, A. A. Olner. A New Theory of Wood's Anomalies on Optical Gratings, *Applied Optics*, 4, 10, pp. 1275 - 1297, 1965.